Mott insulators in disguise

Francesco Grandi

Supervisor: Michele Fabrizio
Adriano Amaricci

Theory and numerical simulation of condensed matter physics
SISSA

This dissertation is submitted for the degree of
Doctor of Philosophy

SISSA October 2018

Table of contents

1 Introduction 1

1.1 Mott insulators 1

1.2 Low temperatures Mott insulators 6

1.3 The orbital quantum number 8

2 Main results 11

2.1 Two bands with different bandwidth 12

2.2 Two bands with different shape: a model for vanadium dioxide 15

3 Dynamical mean-field theory 21

3.1 The Hubbard model 21

3.2 Dynamical mean field theory 23

3.3 Mapping on the Anderson impurity model 28

3.4 Self-consistent solution scheme 29

3.5 Exact diagonalization 30

4 Correlation-driven Lifshitz transition and orbital order in a two-band Hubbard model 33

4.1 The model 35

4.1.1 Weak and strong coupling analyses 36

4.2 Paramagnetic DMFT solution 39

4.3 Anti-ferromagnetic DMFT results 44

4.4 Conclusions 47

5 Vanadium dioxide: a Mott insulator in disguise 49

5.1 Electronic and structural properties of VO_2 50

5.1.1 Evidences of a monoclinic metal 54

5.1.2 Earlier theoretical works 56

5.2 The model 59

5.3 DMFT results 62
5.4 Conclusions 66

6 NCA and OCA impurity solvers 69
6.1 The model 70
6.2 Aim of the calculation 72
6.3 Derivation of the NCA equations at equilibrium 74
    6.3.1 Useful quantities in NCA 75
6.4 Derivation of the OCA equations 76
6.5 Derivation of the NCA equations for the non equilibrium case 78
    6.5.1 Useful quantities in non-equilibrium NCA 81
6.6 Conclusions 82

7 Conclusions and perspectives 83

Appendix A Strong coupling expansion 89

Appendix B Useful out of equilibrium relations 99

Bibliography 109

Chapter 1

Introduction

1.1 Mott insulators

Collective phenomena play a large role in our everyday life, and are ubiquitous in every field of science, going from physics to sociology, passing through ethology [1, 2]. A traffic jam, the motion of bird flocks or the appearance of a magnetic order in a material are few of many examples of the emergent self-organisation of a large number of individuals that occurs due to their mutual interaction. Condensed Matter Physics, dealing with systems made of a large number $\sim 10^{23}$ of elementary constituents, seems to be the perfect playground to study collective emergent phenomena. Due to a large number of degrees of freedom active in a system, it is generally not sufficient nor possible to tackle its description with a reductionistic approach. It is necessary first to identify new physical laws that can describe it as a whole [3, 4]. There are many examples of emergent collective behaviours that arise because of a large number of interacting constituents and that can not be predicted by considering just one or a few of them. One famous example is spontaneous symmetry breaking: even if the system is invariant under a specific symmetry group, it might be that its ground state is not. This is what happens in many cases, e.g., when phenomena such as superconductivity or magnetism are observed.

Since the only many-body models that can be solved exactly are those of non-interacting particles, the common attitude is to search for a minimal description in terms of weakly interacting quasiparticles, not to be confused with the original constituents. Paradigmatic examples are provided by the quasiparticles in the Bardeen-Cooper-Schrieffer model for superconductivity or by the phonons to describe elementary excitations of a lattice with broken translational invariance, or spin-waves in magnetic systems [5–7].

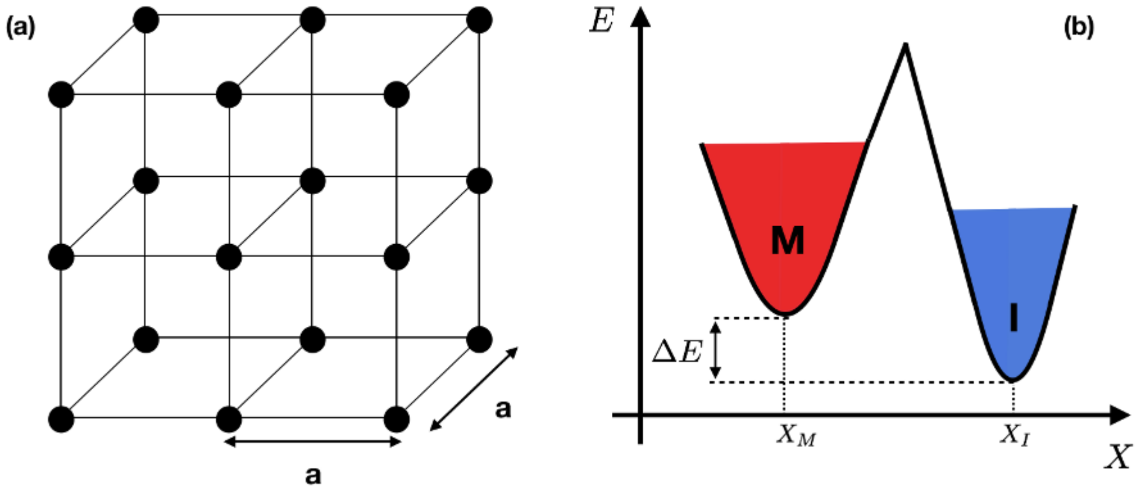

Figure 1.1: Panel (a): cubic crystal made of hydrogen like atoms with lattice spacing a. Panel (b): sketch of the zero-temperature internal energy of the system as function of the unitary cell volume or of the composition (both denoted by X). The red minimum denotes a metallic (M) phase, instead the blue one denotes an insulating solution (I).

There are however relevant cases when emergent collective phenomena elude simple descriptions in terms of independent quasiparticles. One of the most intriguing examples is provided by the Mott transition, i.e., a metal-insulator transition (MIT) driven by the Coulomb repulsion among the electrons. Let us consider, as a simple example, a three-dimensional crystal made of hydrogen-like atoms with a lattice constant a that can be varied for instance by an external pressure (see Fig. 1.1 (a)). We shall ignore atomic motion, which is instead important, e.g., for real hydrogen in the solid phase, and brings in additional complications as the formation of H_2 molecules. By changing a we can identify two regimes: when the atoms are close together, i.e., when a is small, the tunnelling of one electron from one atom to its neighbours is sufficiently strong to guarantee a conducting behavior; the system is a metal, actually a half-filled one. Instead, if the atoms of the lattice are infinitely far apart, i.e. $a \to \infty$, the tunnelling amplitude vanishes, and the system is evidently an insulator. This result is physically quite intuitive. Much less trivial is to foresee, as originally done by Mott, that the metal to insulator transition occurs at a finite value of a. Naïvely, one would expect quantum mechanically that, for any not infinite a, the finite tunnelling amplitude generates a dispersive band that, being half-filled, describes a metal.

In a seminal work [8], Mott not only provided convincing arguments for the transition, since then named Mott transition, to take place at finite a, but he was also able to get an estimate of the critical a at which it should occur. In a simple-minded view, we can regard the above solid hydrogen model as composed by the same number, one per atom, of negatively charged

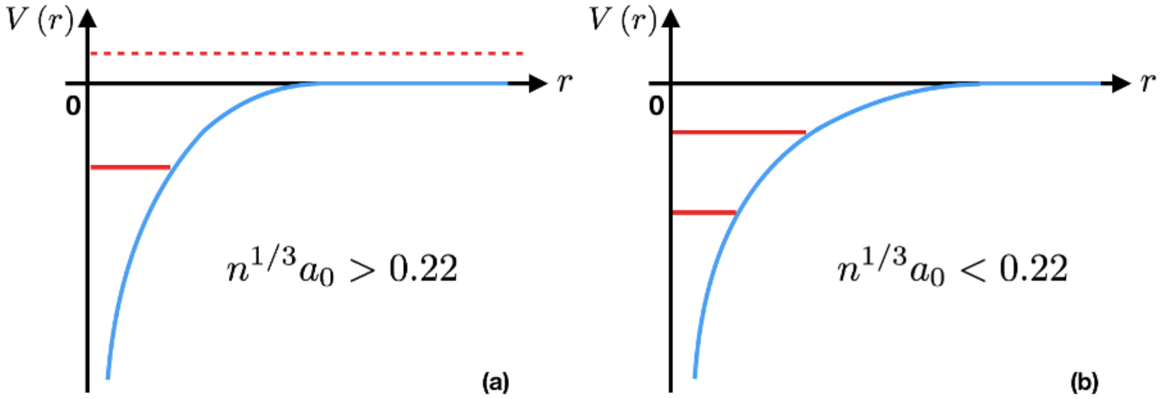

Figure 1.2: Sketch of the Thomas-Fermi potential in the two limits of small and large λ_{TF}. In panel (a) is depicted the case of $n_c^{1/3}a_0 > 0.22$: in that case the potential is really much short range, and it supports a bound state (continuous red line) and a low energy free state (dashed red line). In panel (b) is instead represented the case of $n_c^{1/3}a_0 < 0.22$: the state that in panel (a) was free now has become bound.

particles, the electrons, and of positively charged holes, in this specific case stuck on the immobile atoms. A particle and a hole attract each other via the Coulomb potential, and can thus form a bound state with bond length λ. According to Mott, the transition happens when λ becomes smaller than the Thomas-Fermi screening length λ_{TF}. Since λ_{TF} depends on the electron density n, we can rephrase the problem of finding the critical a as that of searching for the critical density n_c at which the transition occurs. Indeed, we know that $\lambda_{TF} \propto \left(\frac{n}{a_0^3}\right)^{-1/6}$ depends on n, where a_0 is the Bohr radius. This means that, when we lower down the density, i.e., increase a, λ_{TF} increases, too, so the screened Coulomb potential extends sufficiently far to allow for several bound states that deepen more and more as n decreases. It follows that the electrons may prefer to localise and essentially become an integral part of the *core*, as schematically depicted in Fig. 1.2. The critical density obtained by Mott [8–12] is:

$$n_c^{1/3}a_0 \approx 0.22\,. \tag{1.1}$$

Below this critical value, the system is predicted to be insulating. Such very simple estimate works particularly well to locate the MIT in doped or photo-excited semiconductors.

Moreover, Mott predicted that the transition from the metal to the insulator had to be discontinuous. The idea is essentially based on the analogy with the liquid-gas transition, where the liquid is the plasma of electrons and holes, while the gas is composed of bound electron-hole pairs. Close to the transition, the internal energy of the system as function of the relevant thermodynamic variable, that we shall denote as X and might correspond, e.g.,

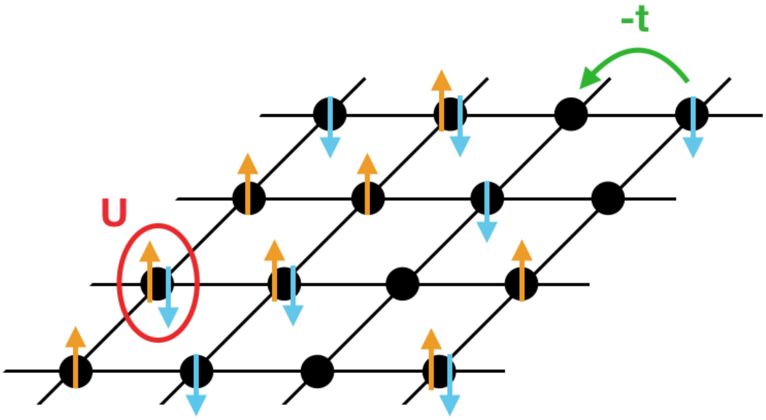

Figure 1.3: Sketch of the Hubbard model. In order to simplify the representation, we present it on a square lattice instead on a cubic one. We see depicted the energy gain $-t$ that we get from moving one electron from a site to a nearest neighbour one, and the energy cost U of having a doubly occupied or an empty site.

to the unit cell volume or the composition, should have a shape like that in Fig. 1.1 (b). By decreasing X, the system goes across a first order phase transition from an insulator to a metal with a concurrent drop in X from X_I to X_M. If X represents the alloy composition, so that changing X means changing the number of carriers, the region between the two minima is unstable and therefore, at equilibrium, the alloy separates in two phases.
We remark that the Mott insulator has a completely different nature with respect to a band insulator of the Bloch-Wilson kind [13–15], which corresponds to a state with a fully occupied valence band and empty conduction one. In the Mott case there is not need to completely fill a band; indeed, a metal-insulator transition can occur even with a partially filled band by changing some external parameters such as the pressure.

The prototypical model that can describe the Mott transition is the Hubbard model, which is essentially a simplified version of the previously discussed solid hydrogen. It is a simple tight-binding model, with nearest neighbour hopping amplitude $-t < 0$, which includes just a local charging energy that penalises valence fluctuations with respect to a reference value and is parametrised by the so-called Hubbard U, see Fig. 1.3. Of course, since we neglect the long-range character of the Coulomb interaction, we would miss part of the physics previously described. Still, such a simple model is able to show a Mott transition. Let us consider the even simpler case in which there is just one valence orbital and one valence electron per site. In the limit of small interaction, $t \gg U$, which would correspond to the small a case, the model describes a half-filled metal. In the opposite limit $U \gg t$, i.e., large a, we can first diagonalise the potential energy and then treat the hopping perturbatively.

The former is minimised by the state where each site is occupied just by a single electron, which is evidently insulating. This state is separated by a gap $2U$ from the lowest energy excitations with one site empty and one doubly occupied site. Because of the finite gap, perturbation theory is well behaved, and thus the system remains insulating even at finite but small $t \ll U$. It follows that there must exist a critical $(U/t)_c < \infty$, above which the ground state is insulating and below which it is metallic.

However, despite the simplicity of the model, this transition is still inaccessible within an independent particle scheme. Indeed, even though the electron charge is localised in the insulating phase at large U/t, its spin can still delocalise throughout the lattice. In fact, although lowest order perturbation theory in t/U does not lead to a charge gap closure, it generates an antiferromagnetic exchange J, equal to $4t^2/U$ at second-order, which makes mobile the spin excitations. In other words, in the Mott insulator, there is a clear separation of spin and charge degrees of freedom, which are instead entangled into one single object, the electron, in any independent particle scheme. This brief discussion allows us introducing an ingredient that was not taken into account in the previous description of the Mott insulator-to-metal transition as the unbinding of electron-hole pairs, but which will be the main focus of this work. Both in the idealised solid hydrogen model and in its simpler version, the Hubbard model, the electron has charge and spin, while the hole only charge. Therefore the electron-hole bound state that constitutes the Mott insulator, although being a neutral object, still possesses a quantum number, the spin, which must be taken into account to get a proper description of the physical behaviour, even across the transition.

Mott insulators can be also artificially realised in cold atom systems [16–19], which actually provide the cleanest realisations of simple Hubbard-like lattice models that can be in this way studied in different equilibrium or out-of-equilibrium situations. However, although those artificial systems may be of invaluable help to shed light in the physics of the Hubbard as well as other lattice models without all complications of real materials, they also lack the richness of the latter ones. Within real materials, the compounds where the conduction bandwidth becomes so small as compared to the Coulomb repulsion to stabilise a Mott insulating phase typically involve elements with partially filled d or f valence shells [20–22], in particular, 3d, 4f and 5f shells [23]. These cases are generally far from the simple picture emerging from the Hubbard model. This is due to many reasons, first of all to the fact that usually more than a single band cross the Fermi level. Moreover, in most cases, the Mott transition is accompanied by a structural distortion, which is often not just a side effect but plays a relevant role.

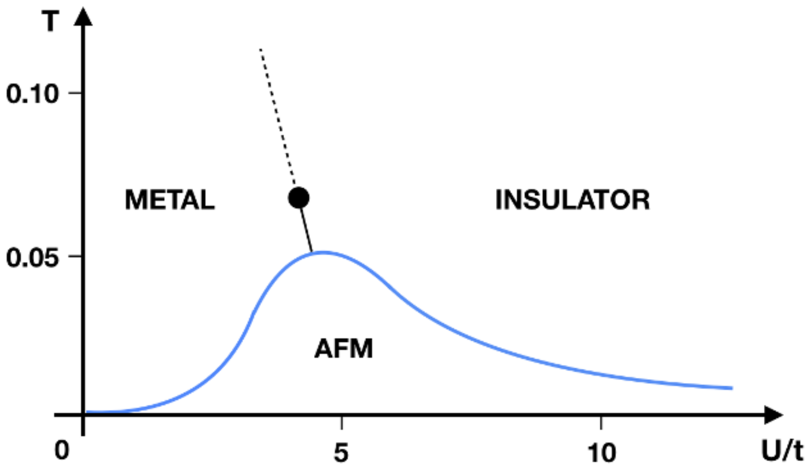

Figure 1.4: Sketch of the magnetic phase diagram of the Hubbard model as function of temperature T and of the intensity of the Hubbard interaction U/t inspired by DMFT calculations [27–29]. Three phases are observable: at each finite U and at temperatures close to zero the system is always antiferromagnetic with a dome-like structure (AFM); at higher temperatures and for small interactions the system is in a paramagnetic metal separated by a first order phase transition (black continuous line) from a paramagnetic insulator. The fist order phase transition ends in a critical point indicated by a dot. For larger temperatures the two phases are separated by a crossover regime (dashed line).

1.2 Low temperatures Mott insulators

As we already mentioned, electron quantum numbers different from the charge are not involved in the Mott's localisation phenomenon. For instance, in the case of the solid hydrogen model, as well as of the half-filled single-band Hubbard model, discussed in Sec. 1.1, in the state that minimises the potential energy though each electron is localised, its spin is totally free. Evidently, a system cannot sustain a finite entropy at zero temperature, all the more since it has means to get rid of it. Therefore, any realistic Mott insulator will also freeze all other degrees of freedom different from the charge, though at energy scales substantially lower than the Mott's localisation one. In general, this freezing corresponds to some symmetry breaking that takes place below a critical temperature, even though one cannot exclude exotic scenarios like spin liquids [24, 25].

In the simple case of the half-filled single-band Hubbard model, it is straightforward to predict which symmetry broken phase is going to be established. As we mentioned, perturbation theory in the hopping t generates an antiferromagnetic exchange among the localised spins.

In dimensions greater than two, and if the lattice is bipartite and the hopping not frustrated, it is quite natural to expect that the low temperature phase must describe an antiferromagnetic insulator [26, 10], which is indeed the case.

More refined calculations permit to get the actual phase diagram that we qualitatively sketch in Fig. 1.4. At low temperatures, the system is, for each value of U, an antiferromagnetic insulator. At small U this is due to the Stoner instability of the nested non-interacting Fermi surface. At large U the physics is instead that described above, i.e., of a Mott insulator that orders magnetically to freeze the spin entropy. The two, physically distinct, regimes are separated just by a crossover, signalled by the maximum in the Néel temperature T_N that occurs around $U/t \sim 5$. For that reason, an independent particle scheme like Hartree-Fock, eventually combined with RPA to access collective spin-wave excitations, provides a reasonable description of the low temperature phase, from the low U Stoner regime, where Hartree-Fock is justified, up to the large U local moment one. In other words, the Mott insulator seems to become describable by independent particle schemes as soon as a symmetry breaking intervenes to freeze out the spin degrees of freedom. This is actually the rule in all realistic Mott insulators that are known to date. One can always find a more or less sophisticated method based on independent particles that is able to reproduce the properties of a Mott insulating material close to zero temperature. For instance, the monoclinic non-magnetic insulating phase of VO_2, which we shall discuss later in this thesis, has been for long time believed to be inaccessible to any *ab-initio* technique based on DFT, and thus taken as an example of the failure of DFT in describing Mott insulators. However, with the development of more efficient hybrid functionals, also the monoclinic phase of VO_2 has been satisfactorily reproduced by DFT [30].

In reality, the success of independent particle approaches to describe Mott insulating materials at low temperature must not mislead about the fundamentally collective character of the Mott transition. Indeed, while those approaches may even be working at low temperature when all degrees of freedom are frozen, they fail at high temperature, when the clear separation of energy scales between the charge and all other degrees of freedom overwhelmingly emerges. A simple example of that is again offered by the phase diagram in Fig. 1.4. Within the Hartree-Fock approximation, the Hubbard interaction U turns into an exchange splitting, Um, between the majority and minority spins, where m is the difference between their local densities and corresponds to the local order parameter in the symmetry broken phase. This exchange splitting also plays the role of a charge gap, i.e., the energy cost to locally add one electron, which, by Pauli principle, must belong to the minority spin band, or remove one, which, in the ground state, belongs instead to the majority spin band. It follows that, as U increases, also the exchange splitting increases, as so T_N. This is incorrect, see Fig. 1.4, since at large U, deep in the Mott insulator, the antiferromagnetic exchange $J \simeq 4t^2/U$ decreases and thus T_N decreases, too. In addition, according to Hartree-Fock as magnetic order melts, i.e., the order parameter $m \to 0$, the exchange splitting must disappear and thus also the charge gap; the model must turn back into a metal phase. This is indeed true at low U, where the magnetic insulating behaviour arises by an instability of the Fermi sea, but it is certainly wrong at large U, where charge fluctuations remain frozen up to a temperature $T_U \sim U \gg t \gg T_N$, above which they are indeed thermally excited but highly incoherent, since $T \gg t$. The system therefore never behaves like a genuine metal at finite temperature.

The above discussion points out that a realistic Mott insulator may be sharply distinguished from a *band* insulator, in the Bloch-Wilson meaning, only at relatively high temperatures, whereas the distinction is quite elusive at low temperature. This allows us introducing the concept of a Mott insulator *in disguise*, i.e., an insulator that becomes as such only because of interaction and Mott's localisation, yet it is disguised as a conventional band insulator by the onset of some symmetry breaking. We shall elaborate further on this idea throughout this Thesis.

1.3 The orbital quantum number

In the previous sections, we mainly analyzed the effect of the spin degree of freedom (DOF) at the Mott transition. However, conduction electrons in real materials may, in addition, possess another quantum number, that is the orbital one. Many materials believed to be Mott insulators, as vanadium sesquioxide V_2O_3, have more than a single band crossing the Fermi level, so a faithful low-energy description has to take this additional DOF into account [31]. In a crystalline environment, the $SO(3)$ orbital symmetry of an isolated atom is drastically lowered down. In most cases, the orbital degeneracy is completely removed, while in others only a discrete symmetry survives. On the contrary, unless spin-orbit interaction is strong, $SU(2)$ spin symmetry is to a large extent preserved. The total or partial absence of symmetry properties among the orbitals that participate to the Mott's localisation actually endows the system with a wealth of different routes to reach a Mott insulating phase, which would not be the case if just a single orbital were involved, because of the constraints put by spin $SU(2)$. The potential richness of the Mott transition in multi-orbital systems still has to be fully explored. Recent years have witnessed a great interest in the orbital selectivity at the Mott transition and in the role of Hund's exchange [32–47], yet there are still interesting open issues.

In this Thesis, we shall focus on a two-band model at quarter filling, i.e., still one electron per site as in the half-filled single-band Hubbard model, which is the simplest extension of the latter model where now the electron that localises at the Mott transition possesses an additional two-valued quantum number beside the spin. The degeneracy between the two bands can in principle be removed in different ways: either splitting their centres of gravity as in the presence of a crystal field or changing the bandwidth or the shape of a band relatively to the other. In physical systems, all those effects might be simultaneously present, though it is preferable to investigate them separately in order to assess their relative importance. Since the role of the crystal field splitting has been already investigated [31], we shall concentrate on the latter two cases and consider either two bands with the same centre of gravity, same shape but different bandwidths, or two bands with the same centre of gravity, same bandwidth but different shapes.

Chapter 2

Main results

In recent years the orbital degrees of freedom have attracted a revived interest, partly stimulated by the physics of ruthenates [48, 49], of iron pnictides [50–52], and of iridates as well as transition metal compounds with strong spin-orbit coupling [53, 54]. Generally, the realistic lattice Hamiltonians used to describe such type of systems are characterized by tight binding parameters that are not invariant under orbital $SO(3)$ rotations. On the other hand, the sensitivity of such systems to the orbital symmetry breaking is significantly enhanced by the effects of electronic interaction. For instance, the distinction between different orbitals brought about by the hopping integrals or the crystal field splitting could be either reduced or amplified by strong correlations. Indeed, the interaction can lead to a striking orbital differentiation [55, 56, 52, 57], eventually causing an orbital-selective Mott transition (OSMT), i.e. the localization of the most narrow band at expense of the remaining itinerant ones [32–47]. Moreover, the orbital degrees of freedom are expected to play an important role in determining which symmetry broken phase is more likely to accompany the Mott transition when correlations grow at integer electron density.

In order to investigate the role of orbital degrees of freedom in strongly correlated systems, here we shall focus on interacting two-bands models with an occupation of one electron per site [58]. In this situation, higher order multipoles do not affect qualitatively the physics, unless they are of comparable strength as the screened monopole Slater integral. This might well be possible in real materials, but is quite an exception rather than the rule. For that reason, we have not included any Coulomb exchange in our study. The two bands can be made inequivalent by a crystal field that shifts the centre of gravity of one relative to the other, a case that has already been studied [31]. We have therefore considered separately two other options, namely,

- two bands with different bandwidth but same shape and centre of gravity;

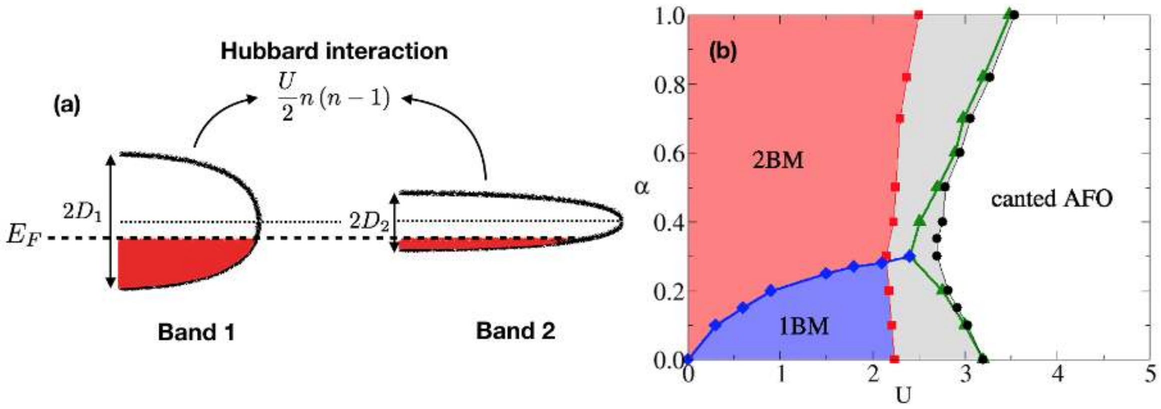

Figure 2.1: Panel (a): sketch of the studied model. It consists in two bands at quarter filling, where E_F is the Fermi level. The two bands have different bandwidth $2D_1 > 2D_2$ and, in the non-interacting case, they have the same centre of gravity. The two states interact with each other through the Hubbard interaction and there are not inter-band hopping terms. Panel (b): paramagnetic phase diagram of the model sketched in panel (a). Three phases are shown: a two-band metal (2BM) where the electron per site is distributed among the two bands, a one-band metal (1BM) where the electron belongs just to the broad band and a canted antiferro-orbital (canted AFO) insulating phase. The metals are connected through a continuous phase transition (diamonds), instead they are both connected to the insulator through a first order transition (triangles). The coexistence region corresponds to the grey area between the circles and the squares.

- two bands with different shape but same bandwidth and centre of gravity.

The remaining part of this chapter is devoted to briefly summarising the main results that we obtained studying those models by dynamical mean-field theory, whose detailed presentation is postponed to Chap. 4 and Chap. 5. These results show that already the simple addition of one more two-valued quantum number besides the spin enriches a lot the physics of the Mott transition at one electron per site, especially if such quantum number is not constrained by any symmetry.

2.1 Two bands with different bandwidth

To begin with we consider the quarter-filled two-band model shown in Fig. 2.1 (a). The two bands are not hybridized among each other and, as we mentioned, the interaction only includes a monopole Slater integral parametrised by the Hubbard U. Similar models were already studied deep in the Mott insulator, where the Hamiltonian can be mapped onto a Kugel-Khomskii type of spin-orbital Heisenberg model [59–62, 53]. However, the physics of such systems is to a large extent yet unexplored right at the Mott transition. Here we focus on this problem and we analyze how the orbital degree of freedom affects the zero temperature

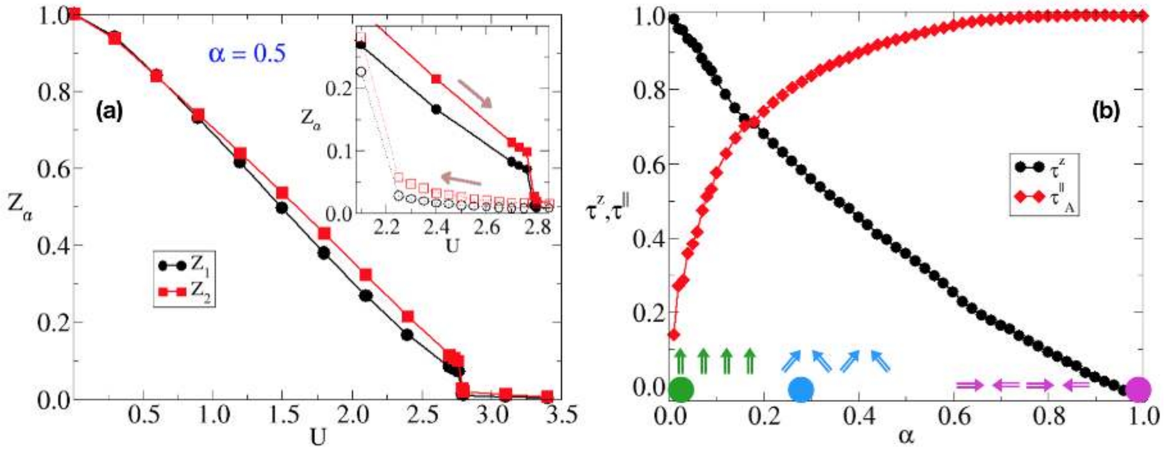

Figure 2.2: Panel (a): quasiparticle residue of band 1 (circles) and band 2 (squares) as function of the Hubbard interaction U for a value of the bandwidth ratio $\alpha = D_2/D_1 = 0.5$. Inset of panel (a): zoom of the region where a first order transition from a conducting to an insulating state is observed, with the corresponding hysteretic behavior. Arrows indicate the direction of the hysteresis cycle. Panel (b): z and in-plane components of the pseudospin orbital vector τ^z and $\tau^{||}$ as function of α at $U = 5$. Arrows form a cartoon for the pseudospin order for specific α points.

Mott transition.
We introduce a parameter $\alpha = D_2/D_1 \in [0, 1]$ that quantifies the difference among the bandwidths and fix $\mathrm{D}_1 = 1$ the energy unit. In the non-interacting case, the broader band 1 is more occupied than the narrower one 2. At weak repulsion U, the Hartree-Fock approximation is valid and predicts that the interaction induces a level repulsion between occupied and unoccupied states, which effectively acts as a crystal field that lowers band 1, which thus becomes more populated, and raises band 2, which empties. The issue is what happens at larger U when Hartree-Fock is not applicable and the system is expected to approach a Mott transition.

We start by presenting the results within the paramagnetic sector, i.e., not allowing for magnetism. If the Hartree-Fock picture could be trusted even at sizeable values of U, we would expect a transition from a quarter-filled two-band metal (2BM) to a one-band metal (1BM), with half-filled band 1 and empty band 2. In the calculations, we indeed found a continuous Lifshitz transition from the 2BM to the 1BM for sufficiently small values of α, see the phase diagram α vs. U in Fig. 2.1 (b). Upon increasing U the metal eventually gives up, and the system turns into a Mott insulator through a first order transition. In the insulator, band 2 is repopulated in such a way that the system shows a canted antiferro-orbital (canted AFO) order.

The properties of the different phases are highlighted in Fig. 2.2. Despite the naïve expectation that the narrower the bandwidth the larger the correlation, here the situation is, to some extent, the opposite. In Fig. 2.2 (a) the quasiparticle residue Z_a, with $a = 1,2$ the orbital index, is shown as function of the Hubbard interaction U. In the region $U < 0.6$, the two quasiparticle residues have almost the same size $Z_1 \approx Z_2$, but for larger values of U we find $Z_1 < Z_2$, meaning that the broader band is more correlated than the narrower. By further increasing the interaction, the system turns discontinuously into a Mott localized state with $Z_1 = Z_2 = 0$. The hysteresis region is shown in the inset of Fig. 2.2 (a).
As we already mentioned, the insulating phase shows orbital order, which can be characterised by the z and the in plane components of the pseudo-spin orbital vector τ^z and $\tau^{||}$. While $\tau^z = \sum_\sigma \langle n_{1,\sigma} - n_{2,\sigma} \rangle$, which measures the orbital imbalance, is uniform across the lattice, the in plane component $\tau^{||} = \text{sgn}\,(\tau^x)\,\sqrt{(\tau^x)^2 + (\tau^y)^2}$ is staggered. At $\alpha = 0$, i.e., when band 2 has zero bandwidth, $\tau^{||} = 0$ and $\tau^z = 1$, meaning that the system is in a ferro-orbital state along z. When $\alpha = 1$ the two bands have the same bandwidth and $\tau^{||} = 1$ while $\tau^z = 0$, namely the system is in an antiferro-orbital state (in this case the direction of the staggered orbital moment is arbitrary because of orbital $SU(2)$ symmetry). The change from one state to the other is just a continuous crossover, as shown in Fig. 2.2 (b). This kind of orbital order can be well rationalised by the corresponding Kugel-Khomskii Hamiltonian, which looks like a standard antiferromagnetic Heisenberg model for spin-1/2, with the role of spin played by the orbital, in a uniform magnetic field directed along z, which is zero at $\alpha = 1$ and increases monotonically. As a result, for any $\alpha < 1$, the lowest energy configuration is a canted antiferro-orbital state with a finite uniform polarisation along z. The model is such that there is no spin-flip transition [63]; the ferro-orbital state occurs only at $\alpha = 0$. Remarkably, though the Kugel-Khomskii Hamiltonian is strictly justified only for very large U, its predictions agree well with the actual dynamical mean-field theory results, even at moderate values of U within the insulating phase.

The phase diagram changes if we allow also for magnetic ordering, see Fig. 2.3 (a). In comparison with Fig. 2.1 (b), we first note the disappearance of the 1BM phase. This is expected because of the nesting property of the half-filled one-band Fermi surface. As mentioned in Sec. 1.2, nesting implies a Stoner instability towards an antiferromagnetic order. In more realistic circumstances where nesting is absent, the Lifshitz transition could well survive. In the present case with nesting, instead of the 1BM, we find a ferro-orbital antiferro-magnetic (FO-AFM) insulator in a quite extended region of the α-U phase diagram. Only for $\alpha > 0.7$ the large-U insulator has again the canted AFO order, still accompanied by antiferromagnetism (AFO-AFM). In this case and unlike before, we do find a continuous *orbital*-flip transition, i.e., the analogous of the spin-flip transition in the orbital space, at

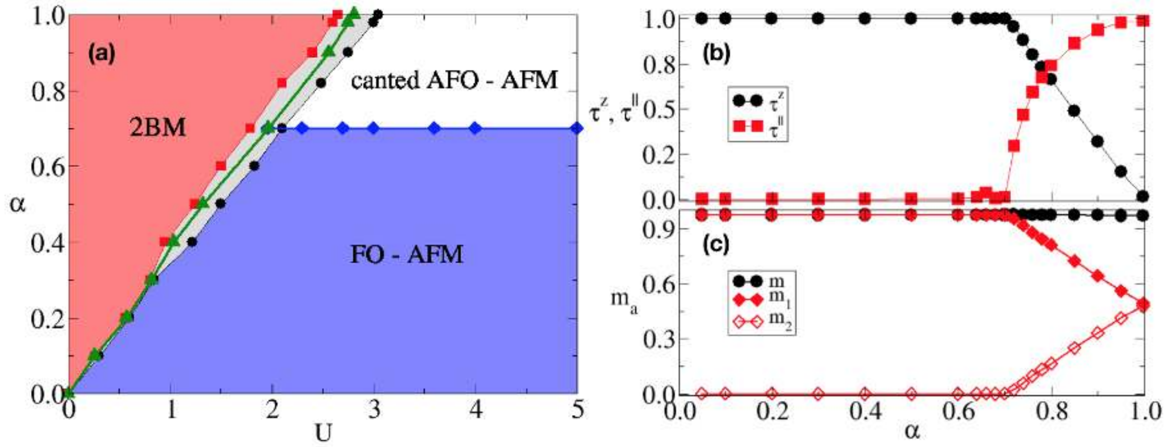

Figure 2.3: Panel (a): magnetic phase diagram in the α-U plane of the model in Fig. 2.1 (a). Three phases are shown: the 2BM, an antiferro-magnetic insulator with just the broad band 1 filled (FO-AFM) and an antiferro-magnetic insulator with canted antiferro-orbital order (canted AFO). The insulators are connected through a continuous phase transition (diamonds), instead the 2BM is connected to both the insulators through a first order transition (triangles). The coexistence region corresponds to the grey area between the circles and the squares. Panel (b): evolution of τ^z and $\tau^{||}$ as function of α at fixed $U = 4.5$. Panel (c): evolution of the total magnetization m and of the magnetizations per band m_a, with $a = 1,2$, as function of α at fixed $U = 4.5$.

a finite value of α within the insulating phase [64]. Both FO-AFM and canted AFO-AFM insulators turn discontinuously into a 2BM upon decreasing U, though the transition occurs at smaller values of interaction than in the absence of magnetism.

The evolution in α within the insulating phase at $U = 4.5$ of the pseudospin components τ^z and $\tau^{||}$ is shown in Fig. 2.3 (b), while that of the spin magnetization per band, $m_a = \langle n_{a,\uparrow} - n_{a,\downarrow}\rangle$, with $a = 1,2$ and of the total spin magnetization, $m = m_1 + m_2$, is shown in Fig. 2.3 (c). Although m is smooth increasing α across the *orbital*-flip transition, m_1 starts to decrease and, concomitantly, m_2 increases from zero. It is a well known fact that a FO phase leads to AFM correlations, the so-called Goodenough-Kanamori-Anderson rules [65, 66, 26]. It is instead less known and obvious that even a canted AFO could lead to antiferromagnetism, as we find.

2.2 Two bands with different shape: a model for vanadium dioxide

We shall now summarise the results that we obtained for a model of two bands with the same bandwidth, same centre of gravity, but different shape. The study of this model was originally inspired by the physics of vanadium dioxide, which we briefly present here. A more detailed discussion is postponed to Chap. 5.

Vanadium dioxide (VO_2) is a transition metal oxide with a great potential for technological applications, thanks to its nearly room temperature metal-to-insulator transition. For this reason, VO_2 has been the subject of an intense investigation which dates back to the 1950s [67], but it is still rather active [68] and, to some extent, debated [69, 30, 70–73].
At $T_c \sim 340$ K, VO_2 crosses a first-order transition from a metal at $T > T_c$ to an insulator at $T < T_c$ [74, 75], both phases being paramagnetic [76–78]. At the same time, a structural distortion occurs from a high temperature rutile (R) structure to a low temperature monoclinic (M1) one.
In the oxidation state V^{4+}, the single valence electron of vanadium can occupy any of the three t_{2g} orbitals that derive from the $3d$-shell split by the crystal field, and which are in turn distinguished into a singlet a_{1g} (or $d_{||}$) and a doublet e_g^π (or d_{π^*}), where the subscripts $||$ and π^* indicate, respectively, the bonding and non-bonding character of the orbitals along the rutile c-axis, c_R. In the R phase, vanadium atoms form equally spaced chains along c_R. In the M1 phase, there is an antiferroelectric distortion where each vanadium moves away from the centre of the oxygen octahedron and the chains, from being straight, become zigzag and, in addition, they dimerise [79, 80].
A simple picture of the transition was proposed back in 1971 by Goodenough [81]. According to it, the antiferroelectric distortion first of all increases the crystal field splitting between the lower a_{1g} and the upper e_g^π. Concurrently, the chain dimerisation opens a hybridisation gap between bonding and anti-bonding combinations of the a_{1g}. For large enough crystal field splitting and hybridisation gap, the bonding combination of the a_{1g} fills completely, while the anti-bonding as well as the e_g^π empty, hence the insulating behaviour.
Goodenough's mechanism for the metal-insulator transition in VO_2 is in essence a single-particle one: the Peierls instability of the quasi one-dimensional a_{1g} band that becomes half-filled after the grown crystal field has emptied the e_g^π. However, the properties of the so-called M2 monoclinic insulating phase that is reached upon as low as ~ 0.2 % [77] partial substitution of V with Cr, or under pressure, indicate that correlations effects are not negligible in VO_2 [82]. However, the existence of a metallic phase at temperatures above the monoclinic to rutile transition suggests that correlation is necessary but not sufficient to explain the metal-insulator transition. In turns, the M2 phase and the *bad metal* character of the R phase [83, 84] suggest that also the coupling to the lattice is necessary but not sufficient. We actually believe that Goodenough's scenario is after all correct, though it requires an active contribution from correlations, thus realising the aforementioned Mott insulator in disguise that can be properly accounted for by many-body techniques, as dynamical mean-field

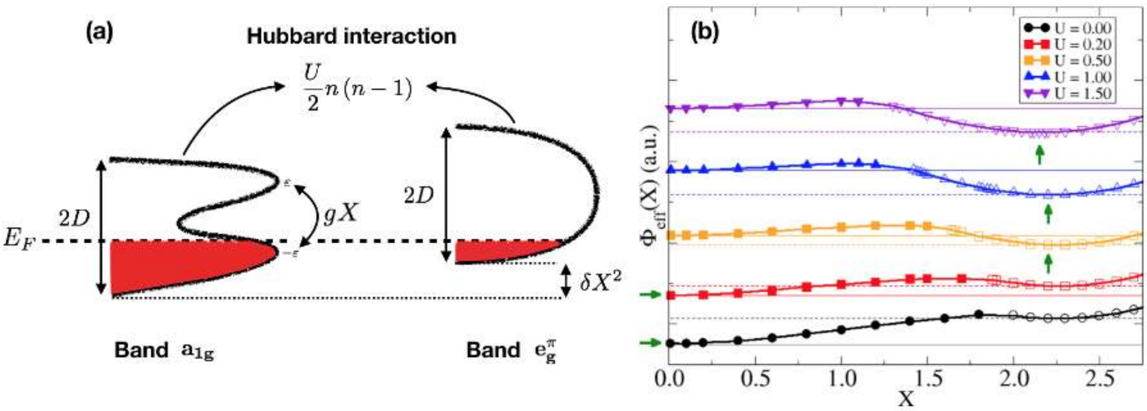

Figure 2.4: Panel (a): sketch of the studied model. It consist in a two band model at quarter filling, where E_F is the Fermi level. The two bands have a different shape but same bandwidth, and, in the non-interacting case without any lattice deformation, they have the same centre of gravity. The two states interact through a local Hubbard term and there is not inter-band hopping. Panel (b): zero-temperature internal energy of the system (in arbitrary units) as function of the lattice distortion X for several values of the Hubbard interaction U. Arrows indicate the position of the absolute minimum for each U. Filled (open) symbols are for the metallic (insulating) solution, instead straight and dashed lines are drawn in order to compare the relative position of the metallic and insulating solutions, respectively.

theory [69], but equally well by independent particle schemes based on DFT [30, 72].

In order to capture the essential aspects of the VO_2 physics, we constructed a minimal model that comprises two bands, one that represents the a_{1g}, band 1, and another the e_g^π, band 2, thus neglecting its doublet character that we believe is unessential. To mimic the quasi-one-dimensional character of the a_{1g}, we assumed a double horn shape of its density of states, with two peaks close to the bottom and the top of the band. On the contrary, the more three-dimensional character of the e_g^π band is reflected in a structureless semi-circular density of states. Both bands have the same bandwidth and are centred at the same energy. Because of the double-horn shape, at quarter-filling band 1 is more occupied than band 2 at $U = 0$, so that, as discussed above, a finite but weak U is expected to generate an effective crystal field splitting that lowers band 1 and raises band 2. In addition, in order to represent the lattice distortion that occurs in VO_2, we include a classical dispersionless phonon X that couples to the bands in two ways: it splits them, hence adding a further contribution to the crystal field produced by U, and concurrently dimerises band 1, i.e., it opens a gap in the middle of its double-horn shaped density of states. We remark that in the real VO_2 the antiferroelectric distortion, i.e. the displacement of V in the basal plane away from the centre of the oxygen octahedron, actually increases and decreases the hybridisation of the e_g^π orbitals with the

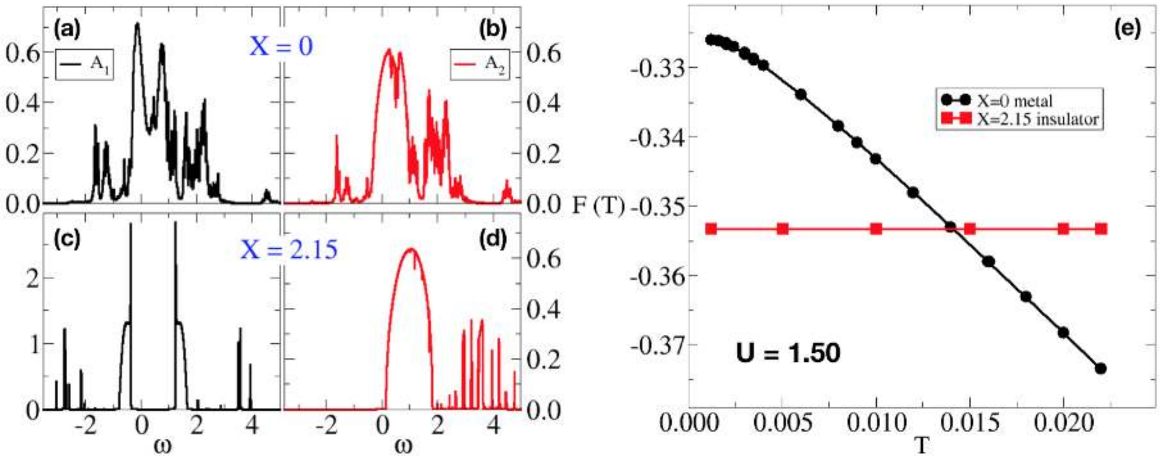

Figure 2.5: Panel (a)-(d): zero temperature spectral functions for $U = 1.50$ at the two minima observed in Fig. 2.4 (b). Particularly, panels (a) and (b) ((c) and (d)) show the spectral functions of band 1 and 2, respectively, when the system is in the undistorted metallic (distorted insulating) phase. Panel (e): free energy $F(T)$ of the system as function of temperature T for the two (stable and metastable) solutions encountered in Fig. 2.4 (b) at $U = 1.50$.

oxygen ligands that are, respectively, closer and further with respect to the off-center position of the vanadium atom. Such variation of the metal-ligand hybridisation has indeed the indirect effect of increasing the e$_g^\pi$ energy, but the raise is quadratic for small displacement. In order to mimic this effect, we assumed that the phonon coordinate X is coupled linearly to dimerisation but quadratically to the population imbalance operator $n_1 - n_2$.

The evolution of the internal energy of the system as function of the lattice distortion X for several values of U is shown in Fig. 2.4 (b). For each U we find two minima, one stable and one metastable. For small U, the stable phase is a metal without any distortion ($X = 0$). On the contrary, the stable phase becomes a distorted, $X \neq 0$, insulator above a critical U, explicitly demonstrating the crucial role of correlations in the metal-insulator transition, in qualitative agreement with the experiments [77, 85, 74, 75].
In order to gain a better understanding of the different phases, we plot in Fig. 2.5 (a)-(d) the spectral functions relative to the two minima at $U = 1.50$, which is a realistic estimate of its actual value. Panels (a)-(b) show the spectral functions of the metallic undistorted solution, while panels (c)-(d) those of the distorted insulator. In the metastable metal phase, both bands are partially filled, with a larger occupancy of band 1 with respect to band 2. The stable insulating phase is instead characterised by a a$_{1g}$ band split into a bonding and anti-bonding components, and the energy gap of between the bonding a$_{1g}$ and the e$_g^\pi$, still in accordance with experiments [86].

By separately evolving with temperature the two solutions at $U = 1.50$, we find the free energy crossing of Fig. 2.5 (e), which signals a first order phase transition between a low temperature distorted insulator and a high-temperature undistorted metal.
All the above results are in qualitative agreement with the actual behaviour of VO_2, suggesting that our simple modelling is representative of the physics of the compound.

Chapter 3

Dynamical mean-field theory

In Chap. 1 we commented about the Mott physics. In this chapter, we will derive a simple model Hamiltonian which can capture the essential ingredients of the strongly correlated electrons and the basic equations for a trustable technique to solve it. In doing so we will introduce some concepts that will be important in the following parts of this thesis.

3.1 The Hubbard model

The description of real materials is, in general, a problem of outmost difficulty. It involves the description of many (approximately $\sim 10^{23}$) degrees of freedom. The complete Hamiltonian of the problem involves the kinetic contributions of the electrons and of the nuclei (ions), the electron-electron, the nucleus-nucleus and the electron-nucleus interactions. In the following we will completely neglect the kinetic term that comes from the nuclei: since their mass is much larger than the electrons one, we make use of the Born-Oppenheimer approximation and consider them as static. Correspondingly, the nucleus-nucleus interaction reduces to a constant shift in the energy and can be safely neglected. We consider the system of a regular (i.e. Bravais) lattice, thus the nuclei are arranged in a periodic structure. The electrons move on a background periodic potential created by the regular layout of the ions. In presence of such lattice potential, the many degenerate electronic levels arrange in a band structure which expresses the energy of the electrons in a particular lattice structure. Should a structural transition occur in a system, it will be reflected in a dramatic change of the band structure.
In the tight binding description, the motion of the electrons is described in terms of a hopping process from site i to site j, occurring with a quantum mechanical probability amplitude t_{ij} [87, 88]. In most cases, the hopping amplitude decays rapidly with the distance so that it is meaningful to assume that just the hoppings among nearest neighbor sites are different from

zero. Moreover, if we assume that all the atoms in the lattice are equal, we can write $t_{ij} = t$, where i and j are nearest neighbors.
In this approach the kinetic term reads:

$$H_K = -t \sum_{\langle i,j \rangle} \sum_{\sigma} c^{\dagger}_{i,\sigma} c_{j,\sigma} \,, \tag{3.1}$$

where $c^{\dagger}_{i,\sigma}$ ($c_{i,\sigma}$) is the creation (annihilation) operator of one electron with spin σ on site i and the sum $\sum_{\langle i,j \rangle}$ is restricted just to nearest neighbour lattice sites.
Finally, one should take into account the Coulomb interaction among the electrons. For a generic system of s or p-orbital electrons this term is small with respect to the bandwidth, fixed by the large overlap between neighbouring electronic wave functions. However, for materials with d or f-electrons the situation can change dramatically. The more localized nature of the d/f-orbital wave functions makes their overlap in space smaller, ultimately leading to narrow bands. In this situation, the interaction term becomes of roughly the same order of the kinetic term and can not be neglected. It is well known that the Coulomb interaction among two charges in the vacuum is long-ranged, instead inside a material the long-range character is suppressed by the screening of the local charge due to the conduction electrons. This effect is the Thomas-Fermi screening that we mentioned in Chap. 1, that changes the spatial dependence of the potential from $\propto \frac{1}{|\boldsymbol{x}_i - \boldsymbol{x}_j|}$ when we are in vacuum to $\propto \frac{e^{-\lambda_{TF}^{-1}|\boldsymbol{x}_i - \boldsymbol{x}_j|}}{|\mathbf{x_i} - \mathbf{x_j}|}$ in a compound. The Thomas-Fermi screening length λ_{TF} for a real material such as copper is estimated to be ~ 0.55 Å.
We can take into account this screening effect when we write the tight binding formulation of the Coulomb interaction. This leads to retain just the local term, since it will be for sure the dominant contribution of the expansion, and we can write it as:

$$H_U = \frac{U}{2} \sum_{i} n_i n_i \,, \tag{3.2}$$

where n_i is the number operator for site i and U is the strength of the Hubbard repulsion. We notice that this energy contribution, at fixed occupation, assumes its minimum value when the system does not have any doubly occupied site, i.e. when the electrons are not close one to the other.
We notice that each one of the two terms in Eq. (3.1) and Eq. (3.2) can be easily diagonalized, the former in reciprocal space, the latter in direct space. Instead, the sum of the two, known

as the Hubbard model [89–91], does not have a simple solution:

$$H = -t \sum_{\langle i,j \rangle} \sum_{\sigma} c^{\dagger}_{i,\sigma} c_{j,\sigma} + \frac{U}{2} \sum_{i} n_i n_i \,. \tag{3.3}$$

This model contains the basic elements of the true Hamiltonian of the problem: the kinetic energy of the electrons, the interaction of them with the static ionic potential and the electron-electron interaction at the minimal level. Despite its apparent simplicity, no exact solution of this model are known in dimension $d > 1$ [92]. The physics of this model is the subject of an intense investigation by means of analytic or numerical methods. The Hubbard model is able to describe the Mott transition from a metallic state to a correlated insulator, as we already discussed in Chap. 1. The proximity to such transition is universally recognized to be an essential ingredient for the many unexpected properties which characterize the strongly correlated electrons systems.

The absence of exact solutions for the model Eq. (3.3) stimulated over the years the development of many approximate analytical and numerical methods. A suitable approach to tackle the description of correlated electrons has been introduced nearly twenty years ago. This method enabled to obtain a controlled solution of the Hubbard model providing an accurate description of the Mott transition. This approach, named Dynamical Mean Field Theory (DMFT), is based on the expansion in the reciprocal dimensionality $1/d$. At any finite dimensionality, it is reasonable to approximate the original lattice problem with infinite degrees of freedom with an effective single-site local problem, with a smaller number of degrees of freedom, as for example in any mean-field approach. The key idea of DMFT is that, for $d \to \infty$, an exact map of the local problem onto an effective quantum many-body problem, i.e. with infinite degrees of freedom, is possible. In facts, in the limit of infinite coordination number a relevant simplification arise: the locality of the self-energy function, which express the effects of interaction at the single particle level. As a mean-field mapping, the DMFT neglects the spatial fluctuations. However, contrary to static mean-field approaches, the DMFT capture exactly the local quantum fluctuations which partly characterize the physics of the correlated systems.

3.2 Dynamical mean field theory

DMFT and its extensions represent the state of the art techniques to treat strongly interacting fermions [29]. In this section, we will derive and discuss the basic DMFT equations. We will see that in analogy with static mean-field, the central quantity of interest in DMFT is the Weiss field. Contrary to static mean-field however, in the DMFT formalism, the Weiss field

takes the form of a function (as opposed to a number). Within DMFT an interacting system of electrons on a lattice is mapped onto that of a single quantum impurity coupled to an effective bath. The properties of the bath, described by a Weiss field, are fixed self-consistently by requiring that the single particle properties of the auxiliary problem are the same as the local ones of the original problem. The functional nature of the Weiss field makes the fulfilment of such self-consistent condition more complicated than in a conventional static mean-field.
The key idea in the derivation of the DMFT equations is taken from a well-known technique developed within classical statistical mechanics [93], i.e the cavity method. This consists in focusing on a specific site o of the lattice model and to integrate out all the degrees of freedom of other sites. In this way we get an effective model for site o. Note that this reduction is exact. However, some approximation will be required in order to solve such effective problem. In the DMFT approach such approximation is obtained by the limit of infinite dimensionality.
The first step consist in writing the action formulation of the Hubbard model Eq. (3.3), and this can easily be done by using Grassmann algebra [94]:

$$\begin{aligned} S = \int_0^\beta d\tau \, [\sum_{i,\sigma} c^*_{i,\sigma}(\tau)\ (\partial_\tau - \mu)\ c_{i,\sigma}(\tau) - \sum_{\langle i,j\rangle}\sum_{\sigma} (t)_{i,j}\, c^*_{i,\sigma}(\tau) c_{j,\sigma}(\tau) + \\ \frac{U}{2}\sum_i n_i(\tau) n_i(\tau)] \,. \end{aligned} \tag{3.4}$$

$c_{i,\sigma}(\tau)$ and $c^*_{i,\sigma}(\tau)$ are Grassmann variables at imaginary time τ, as well as $n_i(\tau) = \sum_\sigma c^*_{i,\sigma}(\tau) c_{i,\sigma}(\tau)$ and μ is the chemical potential that we tune in order to fix the desired occupation $\langle n_i \rangle$. We introduced the notation $(t)_{i,j}$ for the hopping amplitude just to remark which are the sites involved in the motion process. From this action that describes the whole lattice system we want to get an effective action for a single specific site o. In order to do so, we can look at Eq. (3.4) as a sum of three contributions: the action of the site o (S_o), the action of the system without site o ($S^{(o)}$) and the action that describes the interaction of site o with the rest of the lattice (ΔS), so at the end $S = S_o + S^{(o)} + \Delta S$. For later convenience we can introduce a more compact notation for the Grassmann variables on site o:

$$\eta_i = (t)_{i,o}\ c_{o,\sigma} \,, \tag{3.5}$$

and we do in the same way for the complex conjugate variable, so we arrive to write:

$$
\begin{aligned}
\Delta S &= -\int_0^\beta d\tau \sum_{i\neq o}{}^{'} \sum_\sigma \left(c^*_{i,\sigma}\eta_i + \eta^*_i c_{i,\sigma}\right) \,, \\
S_o &= \int_0^\beta d\tau \, [\sum_\sigma c^*_{o,\sigma}(\tau) \; (\partial_\tau - \mu) \; c_{o,\sigma}(\tau) + \frac{U}{2} n_o(\tau) n_o(\tau)] \,, \\
S^{(o)} &= \int_0^\beta d\tau \, [\sum_{i\neq o}\sum_\sigma c^*_{i,\sigma}(\tau) \; (\partial_\tau - \mu) \; c_{i,\sigma}(\tau) \\
&\qquad - \sum_{\langle i,j\rangle \neq o} \sum_\sigma (t)_{i,j} c^*_{i,\sigma}(\tau) c_{j,\sigma}(\tau) + \frac{U}{2}\sum_{i\neq o} n_i(\tau) n_i(\tau)] \,.
\end{aligned}
\tag{3.6}
$$

where the sum $\sum'$ means that we have to perform it just on the nearest neighbors of site o. In order to get the effective action S_{eff} we have to impose:

$$
\begin{aligned}
&\frac{1}{Z_{eff}} e^{-S_{eff}\left[c^*_{o,a,\sigma}, c_{o,a,\sigma}\right]} = \frac{1}{Z}\int \left(\prod_{i\neq o}\prod_\sigma \mathscr{D}c^*_{i,\sigma}\mathscr{D}c_{i,\sigma}\right) e^{-S} \\
&= \frac{1}{Z} e^{-S_o} \int \left(\prod_{i\neq o}\prod_\sigma \mathscr{D}c^*_{i,\sigma}\mathscr{D}c_{i,\sigma}\right) e^{-S^{(o)}-\Delta S} \,.
\end{aligned}
\tag{3.7}
$$

In this expression the partition function of the original lattice Z as well as the effective partition function Z_{eff} of the single site effective problem appear. We also define $Z^{(o)}$ as the partition function of the system described by the action $S^{(o)}$. Moreover, the notation $\int \left(\prod_{i\neq o}\prod_\sigma \mathscr{D}c^*_{i,\sigma}\mathscr{D}c_{i,\sigma}\right)$ means that we have to perform a functional integral over all the Grassmann variables $c^*_{i,\sigma}$ and $c_{i,\sigma}$ for each site i different from o. From the previously given relations it is easy to get:

$$
S_{eff} = S_o - \ln\left(\langle e^{-\Delta S}\rangle_{(o)}\right) - C \,,
\tag{3.8}
$$

where the average $\langle\cdots\rangle_{(o)}$ means that we are averaging over the system without site o. C is the constant $C = \ln\left(\frac{Z_{eff}Z^{(o)}}{Z}\right)$ that we will not write explicitly in the next steps. By taking into account that $\langle \Delta S\rangle_{(o)} = 0$, we arrive to write:

$$
\begin{aligned}
S_{eff} =& S_o + \sum_{n=1}^{\infty} \sum_{i_1,\cdots,i_n\neq o}{}^{'} \; \sum_{j_1,\cdots,j_n\neq o}{}^{'} \int_0^\beta d\tau_{i_1}\cdots d\tau_{i_n} d\tau_{j_1}\cdots d\tau_{j_n} \\
&\eta^*_{i_1}(\tau_{i_1})\cdots\eta^*_{i_n}(\tau_{i_n})\,\eta_{j_1}(\tau_{j_1})\cdots\eta_{j_n}(\tau_{j_n})\, G^{(o)}_{i_1,\cdots,i_n,j_1,\cdots,j_n}\left(\tau_{i_1},\cdots,\tau_{i_n},\tau_{j_1},\cdots,\tau_{j_n}\right) \,,
\end{aligned}
\tag{3.9}
$$

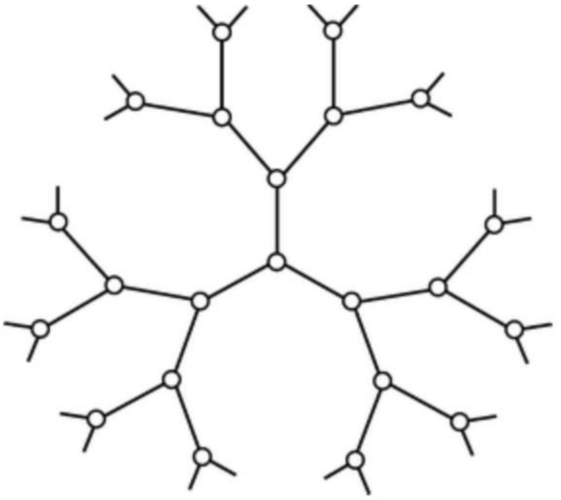

Figure 3.1: Cayley tree with coordination number $z=3$. Adapted from [95].

where $G^{(o)}_{i_1,\cdots,i_n,j_1,\cdots,j_n}\left(\tau_{i_1},\cdots,\tau_{i_n},\tau_{j_1},\cdots,\tau_{j_n}\right)$ is the n-particle connected Green's function of the fully interacting model with site o removed, and the indexes $i_1,\cdots,i_n,j_1,\cdots,j_n$ are multilabel for the spin and the lattice site.

We are now able to see the great semplification of the problem that occurs in the limit of infinite coordination for the model in Eq. (3.3). In order to preserve the extensivity of the energy in this limit, the hopping amplitude must scale as $\frac{1}{\sqrt{z}}$, so we have to perform the substitution $t \to \frac{t}{\sqrt{z}}$. From the definition that we gave in Eq. (3.5) of the Grassmann variables it follows that the n-th order term of the expansion in Eq. (3.9) scales as z^{1-n}. As soon as $z \to \infty$ just the $n=1$ term will remain different from zero, so we can rewrite the effective action as:

$$\begin{aligned} S_{eff} &= S_o + \sum_{i\neq o}{}' \sum_{j\neq o}{}' \sum_{\sigma} \int_0^\beta d\tau_i \int_0^\beta d\tau_j \eta^*_{i,\sigma}(\tau_i)\, \eta_{j,\sigma}(\tau_j)\, G^{(o)}_{i,j}(\tau_i,\tau_j) = \\ &= -\int_0^\beta d\tau_i \int_0^\beta d\tau_j \sum_\sigma c^*_{o,\sigma}(\tau_i)\, \mathscr{G}_0^{-1}(\tau_i,\tau_j)\, c_{o,\sigma}(\tau_j) + \frac{U}{2}\int_0^\beta d\tau\, n_o(\tau) n_o(\tau)\ . \end{aligned} \tag{3.10}$$

In equilibrium conditions the non-interacting single-particle Green's function of the single site effective problem is invariant for translations in time $\mathscr{G}_0^{-1}(\tau_i,\tau_j) = \mathscr{G}_0^{-1}(\tau_i-\tau_j)$ so in Matsubara frequencies we can write, by comparing the two expressions in Eq. (3.10):

$$\mathscr{G}_0^{-1}(i\omega_n) = i\omega_n + \mu - \frac{t^2}{z} \sum_{i,j}{}' G^{(o)}_{i,j}(i\omega_n)\ . \tag{3.11}$$

We can now consider a specific lattice system called Bethe lattice, that represent the limit of infinite coordination $z \to \infty$ of a Cayley tree, as shown in Fig. 3.1. When we remove site o in such a kind of lattice all the nearest neighbors of o are disconnected. For this reason the Green's function $G^{(o)}_{i,j}(i\omega_n)$ that appears in Eq. (3.11) has to be computed for $i = j$, i.e. $G^{(o)}_{i,j}(i\omega_n) = G^{(o)}_{i,i}(i\omega_n)\,\delta_{i,j}$. Since we are working in the limit of infinite connectivity, the removal of one site does not change the local Green's function, so $G^{(o)}_{i,i}(i\omega_n) = G_{i,i}(i\omega_n)$. Moreover, by assuming that the system is invariant for translations in space we get that: $G_{i,i}(i\omega_n) = G(i\omega_n)\,\delta_{i,i}$. At the end Eq. (3.11) can be rewritten as:

$$\mathscr{G}_0^{-1}(i\omega_n) = i\omega_n + \mu - t^2 G(i\omega_n) \ . \tag{3.12}$$

Let us now consider a simple non interacting problem. In this limit the Green's function of the effective model $\mathscr{G}_0(i\omega_n)$ is equal to the local Green's function of the original problem $G(i\omega_n)$, leading to $\mathscr{G}_0(i\omega_n) = G(i\omega_n)$. In this case Eq. (3.12) can be rewritten, by substituting the imaginary Matsubara frequency $i\omega_n$ with the complex variable ζ, as:

$$G^{-1}(\zeta) = \zeta + \mu - t^2 G(\zeta) \ , \tag{3.13}$$

that leads to the local Green's function on the Bethe lattice:

$$G(\zeta) = \frac{(\zeta+\mu) - \sqrt{(\zeta+\mu)^2 - 4t^2}}{2t^2} \ , \tag{3.14}$$

from which we can compute the DOS

$$D(\varepsilon) = -\frac{1}{\pi} Im\left[G\left(\zeta \to \varepsilon + i0^+\right)\right] = \frac{1}{2\pi t^2}\sqrt{4t^2 - (\varepsilon+\mu)^2}\;\theta\left(4t^2 - (\varepsilon+\mu)^2\right) \ . \tag{3.15}$$

The Bethe lattice DOS has finite bandwidth, as any tight binding model in generic lattices in finite dimensions. If we consider instead the limit of infinite dimensions of a hypercubic lattice, we get a gaussian DOS, that has a finite value in every energy range.

The greatest simplification brought about by the limit of infinite coordination number $z \to \infty$ is the local nature of the lattice self-energy, that in this limit coincide with the self-energy of effective problem. This can be deduced by looking at the skeleton perturbation expansion of the single particle self-energy, as was done in [96, 97]. The argument is based on some considerations similar to the ones performed when we excluded all the Green's function with more than one particle from the expression of the effective action Eq. (3.9), and we will not analyze it in detail. It is sufficient to know that $\Sigma_{i,j}(i\omega_n) = \Sigma(i\omega_n)\,\delta_{i,j}$, and this means that it is also independent by the momenta.

Exploiting the locality of the self-energy we can close the equations by writing a self-consistence condition for the Weiss field. This conditions relates the local interacting physics of the original problem, expressed in terms of the local interacting Green's function, with the properties of the effective bath, expressed by the Weiss field itself.
We can write the local interacting Green's function of the lattice in terms of the local self-energy function as [98]:

$$G(i\omega_n) = \int_{-\infty}^{\infty} d\varepsilon \, \frac{D(\varepsilon)}{i\omega_n + \mu - \varepsilon - \Sigma(i\omega_n)} \, . \tag{3.16}$$

The Dyson equation for the effective problem stated in Eq. (3.10) reads:

$$\mathscr{G}^{-1}(i\omega_n) = \mathscr{G}_0^{-1}(i\omega_n) - \Sigma(i\omega_n) \, . \tag{3.17}$$

Finally, due to the equivalence of site o to any other site, it follows that $\mathscr{G}(i\omega_n) = G(i\omega_n)$ and making use of Eq. (3.12) we obtain:

$$G^{-1}(i\omega_n) = i\omega_n + \mu - t^2 G(i\omega_n) - \Sigma(i\omega_n) \, , \tag{3.18}$$

which can be recasted in terms of a self-consistent equations of the form:

$$\mathscr{G}_0^{-1}(i\omega_n) = G^{-1}(i\omega_n) + \Sigma(i\omega_n) \, . \tag{3.19}$$

With this procedure we were able to reduce the original lattice problem to the solution of an effective single site model, supplemented by a self-consistence condition. This is typical of any mean-field approach but, contrary to the classical case, here the effective problem is yet a quantum many-body one. The DMFT mapping establishes a correspondence between the local quantities computed for the lattice and the quantities computed for the effective model.

3.3 Mapping on the Anderson impurity model

In order to solve the DMFT equations, it is very useful to obtain a Hamiltonian formulation of the problem. To this end, it is straightforward to realize that, considering the action of an Anderson impurity model (AIM), we can obtain an expression equivalent to that in Eq. (3.10) integrating out the conduction band, i.e. the bath, degrees of freedom. This enables one to identify the AIM as a Hamiltonian representation of the effective single-site problem discussed in Sec. 3.2. More explicitly, the AIM Hamiltonian reads:

$$\begin{aligned}
H_{AIM} &= H_B + H_I + H_{B-I} \ , \\
H_B &= \sum_{l,\sigma} \varepsilon_l \, c^\dagger_{l,\sigma} c_{l,\sigma} \ , \\
H_I &= -\mu n_d + \frac{U}{2} n_d n_d \ , \\
H_{B-I} &= \sum_{l,\sigma} V_l \left(c^\dagger_{l,\sigma} d_\sigma + d^\dagger_\sigma c_{l,\sigma} \right) \ ,
\end{aligned} \tag{3.20}$$

where H_B is the bath Hamiltonian, H_I the Hamiltonian of the impurity and H_{B-I} represent the hopping processes that can take place from the bath to the impurity and vice versa. $c^\dagger_{l,\sigma}$ $(c_{l,\sigma})$ is the bath creation (annihilation) operator of one electron in the state l with spin σ. $d^\dagger_\sigma$ (d_σ) is the creation (annihilation) operator for an electron on the impurity with spin σ, and $n_d = \sum_\sigma d^\dagger_\sigma d_\sigma$ is the impurity number operator. ε_l represents the energy value of the l-th bath level, instead V_l is the size of the hopping probability amplitude of one electron to move from the impurity to the bath energy level ε_l and vice versa. We assume that those terms are real. The number of bath sites is infinite, so $l = 1, \cdots, \infty$. The non-interacting impurity Green's function can be written as:

$$\mathscr{G}^{-1}_{0,AIM}(i\omega_n) = i\omega_n + \mu - \Delta(i\omega_n) \ , \tag{3.21}$$

where $\Delta(i\omega_n)$ is the hybridization function of the problem defined as:

$$\Delta(i\omega_n) = \sum_l \frac{V_l^2}{i\omega_n - \varepsilon_l} \ . \tag{3.22}$$

Even if the model Eq. (3.20) formally reproduces the same action in Eq. (3.10), this does not mean that they have the same solution. In order to get this result we have to fix the parameters (ε_l, V_l) of the AIM so that the non-interacting Green's function in Eq. (3.21) is equal to $\mathscr{G}_0(i\omega_n)$ in Eq. (3.17).

3.4 Self-consistent solution scheme

Now that we have shown the basic equations of the DMFT we can outline a general solution scheme for the problem. As any non-linear system of equations, the solution of the DMFT problem corresponds to an optimization problem. The simplest, and in many cases working, approach is to use an iterative method. The initial step is to guess the Weiss field $\mathcal{G}_0(i\omega_n) = \mathcal{G}_{0,AIM}(i\omega_n)$ which is the main unknown of the problem. In many cases this step ultimately means that we have to guess some values for the parameters of the AIM (ε_l, V_l). The iterative procedure is then the following:

1. Given the Weiss field a solution of the AIM is obtained, generally using numerical techniques such as Quantum Monte-Carlo or Exact Diagonalization. The direct output of this step is the calculation of the impurity self-energy $\Sigma(i\omega_n)$.
2. From the knowledge of the self-energy one can compute, by using Eq. (3.16), the local interacting Green's function $G_{new}(i\omega_n)$ of the lattice problem.
3. Next the Weiss field $\mathcal{G}_{0,new}(i\omega_n)$ is updated using the self-consistency relation Eq. (3.17): $\mathcal{G}_{0,new}(i\omega_n) = \left[G^{-1}_{new}(i\omega_n) + \Sigma(i\omega_n)\right]^{-1}$

The whole procedure is iterated until convergence is reached. The convergence is usually evaluated in terms of a suitable function, such as the Weiss field or the self-energy. The solution is usually achieved within 10-100 iterations, depending on the particular regime of the model.

The key step in the DMFT iterative solution is the solution of the quantum many-body problem placed by the auxiliary AIM. To this end, a variety of methods have been developed over many years. In this thesis, we used a technique named Exact Diagonalization (ED), which allow obtaining an accurate solution at zero or finite, but low, temperature. In the next section, we shall describe with some details the ED algorithm.

3.5 Exact diagonalization

The ED [99] method is based on the approximation of the Hamiltonian Eq. (3.20), that in principle has an infinite number of bath states, to a Hamiltonian that has, instead, a finite number $l = 1, \cdots, N_s$ of levels:

$$H_{AIM} \approx \sum_{l=1}^{N_s} \sum_{\sigma} \left[\varepsilon_l c^{\dagger}_{l,\sigma} c_{l,\sigma} + V_l \left(c^{\dagger}_{l,\sigma} d_{\sigma} + h.c.\right)\right] - \mu n_d + \frac{U}{2} n_d n_d \,. \tag{3.23}$$

As a consequence, the hybridization function that appears in the expression of the Weiss field in Eq. (3.21) is written as:

$$\Delta(i\omega_n) = \sum_{l=1}^{N_s} \frac{V_l^2}{i\omega_n - \varepsilon_l} \,. \tag{3.24}$$

This approximation can be seen as the projection of the true Weiss field $\mathcal{G}_0(i\omega_n)$ into the restricted functional subspace that contains the hybridization functions of the kind Eq. (3.24). The discretized finite system, for a given set of Hamiltonian parameters, can then be diagonalized exactly using Lanczos based techniques [100]. This allows to obtain the lowest part of the spectrum and to evaluate the (impurity) interacting Green's function $G(i\omega_n)$ in terms of its Lehmann (or spectral) representation:

$$\begin{aligned} G(i\omega_n) =& \sum_N \frac{1}{Z_N} \sum_{i,j} \frac{\langle \psi_i^N | d_\sigma | \psi_j^{N+1} \rangle \langle \psi_j^{N+1} | d_\sigma^\dagger | \psi_i^N \rangle}{i\omega_n - \left(E_j^{N+1} - E_i^N \right)} \left(e^{-\beta E_i^N} + e^{-\beta E_j^{N+1}} \right) \\ &+ \sum_N \frac{1}{Z_N} \sum_{i,j} \frac{\langle \psi_i^N | d_\sigma^\dagger | \psi_j^{N-1} \rangle \langle \psi_j^{N-1} | d_\sigma | \psi_i^N \rangle}{i\omega_n - \left(E_i^N - E_j^{N-1} \right)} \left(e^{-\beta E_i^N} + e^{-\beta E_j^{N-1}} \right) , \end{aligned} \tag{3.25}$$

where Z_N is the partition function of the problem for fixed number of particles N in the system (that can be computed from the knowledge of the eigenvalues), the states $|\psi_i^N\rangle$ are the eigenstates of the Hamiltonian and E_i^N are the corresponding eigenvalues. $\beta = 1/T$ is the inverse temperature. While the expression Eq. (3.25) is exact if the sum over i and j takes into account all the excited states of the problem, in practice the Lanczos approach allows to obtain directly the amplitudes with some states j which are connected to the target states, i.e. the ground state or low lying excited ones.

The number of levels generally considered for the discretization of the bath is of the order of $N_s = 5 - 12$. The computation of the Green's function in Eq. (3.25) needs only a finite number of excited states that increases with the temperature [101–103]. At zero temperature Eq. (3.25) simplifies since the summation over the index i disappears (we consider just the ground state), the sum of the Boltzmann factors is equal to one while the partition function equals the number of degenerate states.

By implementing the procedure discussed in Sec. 3.4 we get, at each step, a function $\mathcal{G}_{0,new}(i\omega_n)$ that may lay out from the space of the functions with hybridization functions of the kind Eq. (3.24). For this reason, we have to project back to that subspace the new Weiss field. This procedure, which is part of the self-consistency, is performed by means of a multi-dimensional conjugate gradient minimization in the functional space of the Weiss field.

As said the ED method enables to investigate the physics at zero-temperature, i.e. in the ground state, giving direct access to local functions on the whole complex plane. Moreover, the adaptive nature of the discretized effective bath minimizes the finite size effects, so that the scaling with the number of bath sites converges already for $N_s = 8 - 12$.

Chapter 4

Correlation-driven Lifshitz transition and orbital order in a two-band Hubbard model

In this chapter, we present the results that we get by considering a system of two bands with different bandwidth at quarter filling. Before doing so, we show some results about a formally similar model that represents the paradigm for the orbital-selective Mott transition (OSMT) [35–47]: a two-band Hubbard model with bands with different bandwidth but at half rather than at quarter filling [32–34]. The Hamiltonian of the problem is

$$H = -\frac{1}{\sqrt{z}} \sum_{\langle \mathbf{R}\mathbf{R}' \rangle, \sigma} \sum_{a=1}^{2} t_a \left(c^\dagger_{\mathbf{R}a\sigma} c_{\mathbf{R}'a\sigma} + H.c. \right) + \frac{U}{2} \sum_{\mathbf{R}} n_{\mathbf{R}} \left(n_{\mathbf{R}} - 1 \right) , \tag{4.1}$$

on a Bethe lattice of coordination number z that we send to infinity (see Sec. 3.2). In (4.1) the operator $c_{\mathbf{R}a\sigma}$ ($c^\dagger_{\mathbf{R}a\sigma}$) annihilates (creates) an electron at site $\mathbf{R}$ in orbital $a = 1,2$ with spin $\sigma = \uparrow, \downarrow$, $n_{\mathbf{R}} = \sum_{a\sigma} n_{\mathbf{R}a\sigma} = \sum_{a\sigma} c^\dagger_{\mathbf{R}a\sigma} c_{\mathbf{R}a\sigma}$ is the number operator at site $\mathbf{R}$, and t_a a nearest neighbour hopping integral, diagonal in the orbital index a. Hereafter we shall assume $t_1 = 1 \geq t_2$ and define the hopping anisotropy parameter $\alpha = t_2/t_1 \in [0,1]$. Being at half-filling means that the average occupation per site is of two electrons $\langle n_{\mathbf{R}} \rangle = 2$.

The model in Eq. (4.1) was studied in [33] by using Gutzwiller technique and we report the phase diagram in the α-U plane in Fig. 4.1 (a). Three phases are observed: a two band metal (2BM) where both bands are conducting, a phase with the narrow band localized and the broad one still itinerant (OSMT) and a Mott insulating state where both bands are localized (INS). All the transitions are continuous and both bands are at half-filling, separately, in all the regions of the phase diagram. Of course, when we enter the OSMT

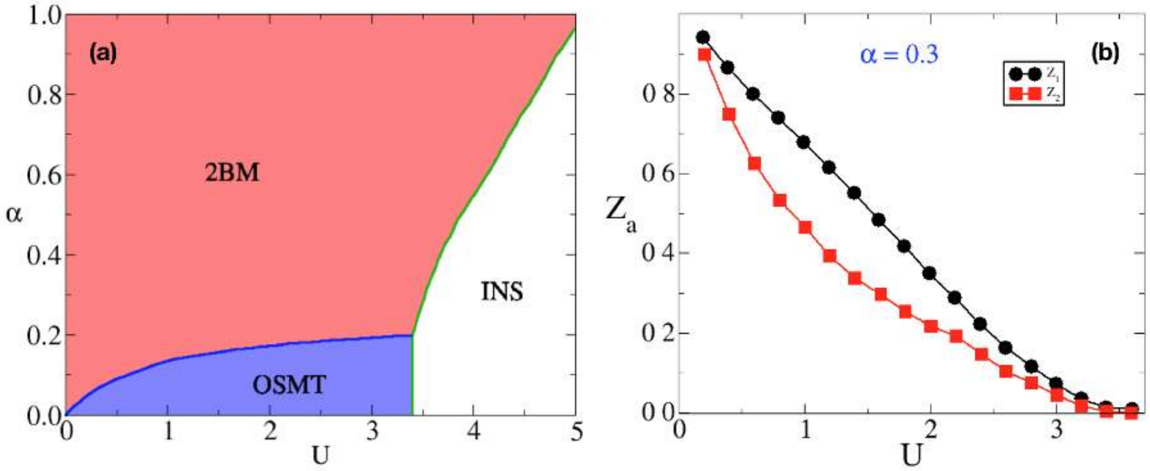

Figure 4.1: Panel (a): non-magnetic phase diagram of the model Eq. (4.1) in the U–α plane. We observe three different phases: a two-bands metal (2BM) at small U and large enough α, an orbital selective Mott phase (OSMT) for small α and small U and a Mott insulator with both bands localized (INS) for sufficiently large values of the interaction. The different phases are connected through a continuous transitions. A tricritical point is present at the merging of the transition lines. Panel (b): quasiparticle residues Z_a as function of U, for $\alpha = 0.3$. Both Z_1 and Z_2 vanish at $U \simeq 3.5$ signaling the transition to the Mott state. Adapted from [33].

phase the band with the smaller bandwidth is more correlated than the broad one, since the first is localized, the second is not. By looking at the evolution of the quasiparticle weight per band $Z_a \approx \frac{m_a}{m_a^*}$, where m_a (m_a^*) is the bare (dressed) mass of the carriers in band a, as function of the Hubbard interaction amplitude U for $\alpha = 0.3$, we get the same scenario even in the 2BM phase, with $Z_2 < Z_1$. The picture that we can sketch from this brief analysis is that the smaller is the bandwidth the larger are the effects of the correlation on it. The occupations of the two bands do not change by increasing the size of the Hubbard interaction. This phenomenon is paradigmatic of many physical situations, the best-known examples being heavy fermions [104] and ruthenates [48].

Starting from this scenario, we consider the same model as in Eq. (4.1) but with an occupation of one electron per site. This may appear as a small change in the model, but we will see how it affects the phase diagram in Fig. 4.1 (a).

We notice that in the model Eq. (4.1) the effect of the Hund's coupling was disregarded. This was done in order to simplify the comparison of the phase diagram in Fig. 4.1 (a) with the one that we are going to present in the next sections. Indeed, the model that we will consider does not include the effect of the Hund's interaction.

4.1 The model

We consider the Hubbard model of two orbitals with different hopping integrals

$$H = -\frac{1}{\sqrt{z}} \sum_{\langle \mathbf{R}\mathbf{R}' \rangle, \sigma} \sum_{a=1}^{2} t_a \Big(c^\dagger_{\mathbf{R}a\sigma} c_{\mathbf{R}'a\sigma} + H.c. \Big) + \frac{U}{2} \sum_{\mathbf{R}} n_{\mathbf{R}} \left(n_{\mathbf{R}} - 1 \right) - \mu \sum_{\mathbf{R}} n_{\mathbf{R}} \,, \tag{4.2}$$

where μ is the chemical potential and we use the same notation we used in Eq. (4.1) for the operators and the parameters. As we anticipated we shall focus on the quarter-filled density case, i.e. $\langle n_{\mathbf{R}} \rangle = 1$, and we consider an interaction term (see (4.2)) which includes the monopole Slater integral $U > 0$, but not the Coulomb exchange J responsible of Hund's rule. This term corresponds to the density-density part of the Kanamori interaction [105, 51] with no Hund's coupling. We study this model on the Bethe lattice.

We introduce the local spin and orbital pseudo-spin operators, $\boldsymbol{\sigma}_{\mathbf{R}}$ and $\boldsymbol{\tau}_{\mathbf{R}}$, respectively, through:

$$\begin{aligned} \boldsymbol{\sigma}_{\mathbf{R}} &= \sum_{a\sigma\sigma'} c^\dagger_{\mathbf{R}a\sigma}\, \boldsymbol{\sigma}_{\sigma\sigma'}\, c_{\mathbf{R}a\sigma'} \,, \\ \boldsymbol{\tau}_{\mathbf{R}} &= \sum_{\sigma ab} c^\dagger_{\mathbf{R}a\sigma}\, \boldsymbol{\sigma}_{ab}\, c_{\mathbf{R}b\sigma} \,, \end{aligned}$$

where $\boldsymbol{\sigma} = (\sigma^x, \sigma^y, \sigma^z)$, with $\sigma^{x,y,z}$ being the Pauli matrices. The Hamiltonian (4.2) is invariant under global spin-$SU(2)$ rotations. On the contrary, orbital $SU(2)$ symmetry holds only at $\alpha = 1$, while for any $\alpha < 1$ the symmetry is lowered down to $U(1)$, which corresponds to uniform rotations around the orbital pseudo-spin z-axis. It follows that a finite expectation value of the z-component of the uniform pseudo-spin operator, which defines the orbital polarisation

$$\tau^z = \frac{1}{V} \sum_{\mathbf{R}\sigma} \langle n_{\mathbf{R}1\sigma} - n_{\mathbf{R}2\sigma} \rangle \,, \tag{4.3}$$

V being the number of lattice sites, is allowed by symmetry, while a finite expectation value of $\boldsymbol{\sigma}_{\mathbf{R}}$ and of $\tau^{x,y}_{\mathbf{R}}$ would break a Hamiltonian symmetry, the spin $SU(2)$ and the orbital $U(1)$, respectively. We underline that when $\alpha = 1$ the symmetry of the model is enlarged to $SU(4)$. The ground state of the system, in this peculiar case, was studied in [106] for the square lattice. They observe that the unitary cell of the system becomes a square plaquette of four atoms, with couples of them dimerized. Each dimer involves just two of the four possible colors, but at the end on a plaquette all of them are involved. Dimers with the same colours are never nearest neighbor. Due to the specificity of this point $\alpha = 1$, we will not consider it in our study.

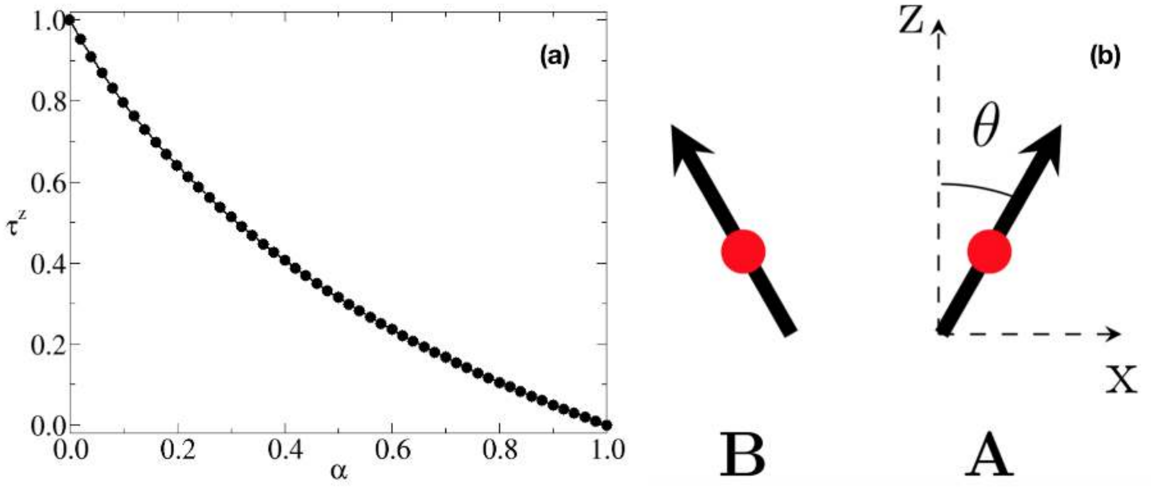

Figure 4.2: Panel (a): Orbital polarisation τ^z as function of α for the non interacting ($U = 0$) case. Panel (b): Schematic representation of the canted AFO phase, assuming that the $U(1)$ symmetry is broken along x, i.e., $\phi = 0$ in Eq. (4.9). The arrows represent the configuration of the orbital pseudo-spin vectors $\boldsymbol{\tau}$ at the two sites (red dots) A and B in the unit cell. θ is the angle between the z direction and the pseudospin $\boldsymbol{\tau}$ on sublattice A (on sublattice B the angle has the value $-\theta$).

4.1.1 Weak and strong coupling analyses

We can actually anticipate some features of the phase diagram by simple arguments in the weak and strong coupling regimes, respectively.

Weak coupling

When $U = 0$, the system describes a quarter-filled two-band metal (2BM) with uniform orbital polarisation $\tau^z = 0$ at $\alpha = 1$ that increases monotonically as α decreases (see Fig. 4.2 (a)). A finite $U \ll \alpha$, small enough to justify the Hartree-Fock approximation, introduces an effective crystal field splitting between the two bands

$$\begin{aligned} H \to H_{\text{HF}} = &-\frac{1}{\sqrt{z}} \sum_{\langle \mathbf{R}\mathbf{R}' \rangle, \sigma} \sum_{a=1}^{2} t_a \left(c^\dagger_{\mathbf{R}a\sigma} c_{\mathbf{R}'a\sigma} + H.c. \right) \\ &- \sum_{\mathbf{R}} \left(\mu_{\text{HF}}\, n_{\mathbf{R}} + \Delta^{\text{eff}}_{\mathbf{R}} \left(n_{1\mathbf{R}} - n_{2\mathbf{R}} \right) \right), \end{aligned} \tag{4.4}$$

where[31, 107]

$$\Delta^{\text{eff}}_{\mathbf{R}} = \frac{U}{2} \langle n_{1\mathbf{R}} - n_{2\mathbf{R}} \rangle = \frac{U}{2} \tau^z, \forall \mathbf{R}, \tag{4.5}$$

which, for any $\alpha < 1$, favors the occupation of the band 1 that has larger bandwidth. If such mean-field result remained valid even at sizeable U, we would expect a topological Lifshitz transition from a quarter-filled 2BM into a half-filled one-band metal (1BM). We note that, as long as the model remains in a quarter-filled 2BM phase, it is stable towards a Stoner-like instability with modulated magnetic and/or orbital ordering, which, in the present case, is expected to corresponds to a translational symmetry breaking where the two-sublattice become inequivalent. On the contrary, the half-filled 1BM phase should become immediately unstable towards such symmetry breaking [108], turning the metal phase into an insulating one with magnetic and/or orbital ordering. In particular, since the hopping is diagonal in the orbital index, we expect a magnetic order that corresponds to a simple Néel antiferromagnet, where, because of spin $SU(2)$ invariance, symmetry can be broken along any spin direction. Conversely, the Hamiltonian for any $\alpha < 1$ is only invariant under orbital $U(1)$ rotations around the pseudo-spin z-axis. Therefore, the possible orbital orderings cannot be anticipated as simply as for the spin ones, and we must resort to some more sophisticated calculation. However, since all transitions are expected to occur at finite U, there is no guarantee that the above mean-field arguments hold, and thus the need of DMFT that is able to provide accurate results for any interaction strength.

Strong coupling

In order to foresee which orbital ordering is most likely to occur, we can still perform some simple analysis. Deep in the Mott insulator, i.e. at strong coupling $U \gg 1$, we can map the lattice model Eq. (4.2) onto an effective Kugel-Khomskii spin-orbital Heisenberg Hamiltonian $H \overset{U\gg 1}{\longrightarrow} H_{\mathrm{KK}}$ [26, 59], where

$$\begin{aligned} H_{\mathrm{KK}} = \frac{1}{z} \sum_{\langle \mathbf{R}\mathbf{R}' \rangle} \Bigg\{ & \frac{1}{16U}\Big(1+\boldsymbol{\sigma}_{\mathbf{R}}\cdot\boldsymbol{\sigma}_{\mathbf{R}'}\Big)\Big[(1+\alpha^2) \\ & + (1-\alpha^2)\Big(\tau^z_{\mathbf{R}}+\tau^z_{\mathbf{R}'}\Big) + (1+\alpha^2)\,\tau^z_{\mathbf{R}}\,\tau^z_{\mathbf{R}'} \\ & + 2\alpha\Big(\tau^x_{\mathbf{R}}\,\tau^x_{\mathbf{R}'} + \tau^y_{\mathbf{R}}\,\tau^y_{\mathbf{R}'}\Big)\Big] \\ & - \frac{1}{8U}(1-\alpha^2)\Big(\tau^z_{\mathbf{R}}+\tau^z_{\mathbf{R}'}\Big) - \frac{1}{4U}(1+\alpha^2)\Bigg\} . \end{aligned} \tag{4.6}$$

We can solve this hamiltonian at the mean field level factorizing the wave-function into a spin part, $\mid \psi_\sigma\rangle$, and an orbital pseudo spin one, $\mid \psi_\tau\rangle$. We assume that the expectation value on the spin wave-function

$$\langle \psi_\sigma \mid \boldsymbol{\sigma}_{\mathbf{R}}\cdot\boldsymbol{\sigma}_{\mathbf{R}'} \mid \psi_\sigma\rangle = -\varepsilon \in [-1,1] . \tag{4.7}$$

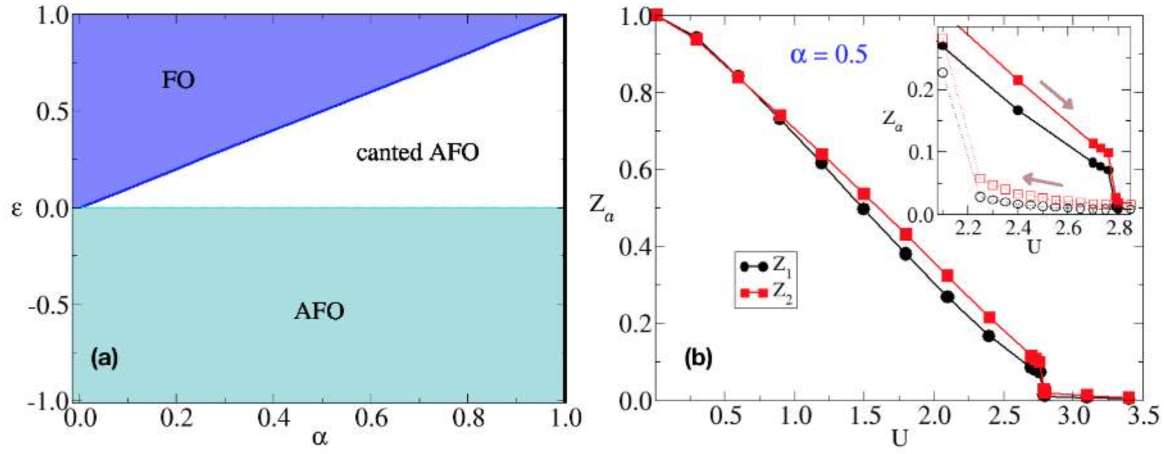

Figure 4.3: Panel (a): mean field phase diagram of the strong coupling Hamiltonian Eq. (4.6) as a function of α and of the phenomenological parameter ε, defined in Eq. (4.7). The diagram shows three distinct phases: a ferro- (FO) and an antiferro- (AFO) orbital state along the z-direction of the pseudospin and a canted AFO. The AFO phase is connected to the canted AFO through a first order transition (dashed line). The FO phase is separated from the canted AFO by a continuous transition (solid line). When $\varepsilon > 0$ ($\varepsilon < 0$) the system has antiferromagnetic (ferromagnetic) correlations. Along the line $\alpha = 1$ the model is $SU(4)$ invariant, and our simple mean field approximation does not apply any more. Panel (b): the quasiparticle residues Z_a as function of U, for $\alpha = 0.5$. Both Z_1 and Z_2 vanish at $U = U_{c2} \simeq 2.80$ signaling transition to the Mott insulator. Inset: Hysteretic behaviour of Z_a near the critical point. Filled (open) symbols are obtained continuing the solution from small (large) values of U.

Let us briefly comment about the meaning of Eq. (4.7). In a generic lattice

$$\langle \boldsymbol{\sigma}_{\mathbf{R}} \cdot \boldsymbol{\sigma}_{\mathbf{R}'} \rangle = \langle \boldsymbol{\sigma}_{\mathbf{R}} \rangle \cdot \langle \boldsymbol{\sigma}_{\mathbf{R}'} \rangle + \mathscr{O}\left(\frac{1}{z}\right), \tag{4.8}$$

so that in the limit of infinite coordination, $z \to \infty$, the parameter ε in Eq. (4.7) is finite as long as spin $SU(2)$ symmetry is broken, in which case the mean-field approximation predicts an antiferromagnetic spin configuration, $\varepsilon = 1$, and a ferro-orbital (FO) one, with expectation value $\langle \psi_\tau \mid \tau^z_{\mathbf{R}} \mid \psi_\tau \rangle = 1$, $\forall \mathbf{R}$. On the contrary, if we were to discuss the mean-field phase diagram of the Hamiltonian (4.6) in the paramagnetic sector and in the limit $z \to \infty$, we should, strictly speaking, set $\varepsilon = 0$. In this case the mean-field approximation for any $0 < \alpha < 1$ predicts two degenerate pseudo spin configurations, one, which we denote as antiferro-orbital (AFO), characterized by the finite expectation value $\langle \psi_\tau \mid \tau^z_{\mathbf{R}} \mid \psi_\tau \rangle = (-1)^R$, and the other, which we denote as canted antiferro-orbital (canted AFO), see Fig. 4.2 (b), with non-zero expectation values

$$\begin{aligned} \langle \psi_\tau \mid \left(\cos\phi\, \tau^x_{\mathbf{R}} + \sin\phi\, \tau^y_{\mathbf{R}}\right) \mid \psi_\tau\rangle &= (-1)^R\, \tau^{||}\,, \\ \langle \psi_\tau \mid \tau^z_{\mathbf{R}} \mid \psi_\tau\rangle &= \tau^z\,, \end{aligned} \tag{4.9}$$

where $\tau^z = \cos\theta = (1-\alpha)/(1+\alpha)$, $\tau^{||} = \sin\theta$ and ϕ is free, signalling breaking of the orbital $U(1)$ symmetry. This result does not agree with DMFT, see below, which suggests that higher order terms in $1/U$, not included in Eq. (4.6), split the above accidental degeneracy. As a matter of fact, the actual DMFT phase diagram can be still rationalized through the mean-field treatment of the simple Hamiltonian (4.6), proviso a finite ε is assumed even in the paramagnetic sector and despite $z \to \infty$.

For the above reason, we shall hereafter take ε as a free parameter, in terms of which the phase diagram as function of α is that shown in Fig. 4.3 (a). Whenever $\varepsilon < 0$ (ferromagnetic correlations) and $\alpha < 1$ the system is in an AFO state. When instead $\varepsilon > 0$, as physically expected, we find either a FO state for $\alpha < \varepsilon$ or a canted AFO one otherwise. The transition between the two phases is continuous within mean-field. Finally, for $\varepsilon = 0$, as we mentioned, the canted AFO and the AFO are accidentally degenerate. The transition between them is first order.

4.2 Paramagnetic DMFT solution

We now turn to exact DMFT and start by analyzing the model (4.2) searching for paramagnetic solutions. However, since the Hamiltonian is not orbital pseudo-spin invariant, we cannot avoid orbital ordering.

As we commented in the previous section, since the Bethe lattice is bipartite and the Hamiltonian is not frustrated, the most likely spatial modulation breaks the symmetry between the two sub-lattices, which we shall label as sublattice $\Lambda = A$ and $\Lambda = B$. Within DMFT, the lattice model is mapped onto two distinct effective impurity problems, one for each sub-lattice. In this work we shall employ zero-temperature exact diagonalization as impurity solver (see Sec. 3.5), with a total number $N_s = 10$ of sites (8 bath levels).

We first consider an intermediate value of the bandwidth ratio $\alpha = 0.5$ and we show how the weakly interacting 2BM is driven to a Mott insulating state by increasing the interaction strength U. Such phase-transition is revealed by the evolution of the quasiparticle residue

$$Z_a = \left(1 - \frac{\partial \mathrm{Re}\Sigma_{aa}(\omega)}{\partial\omega}\right)^{-1}_{|\omega=0}\,, \tag{4.10}$$

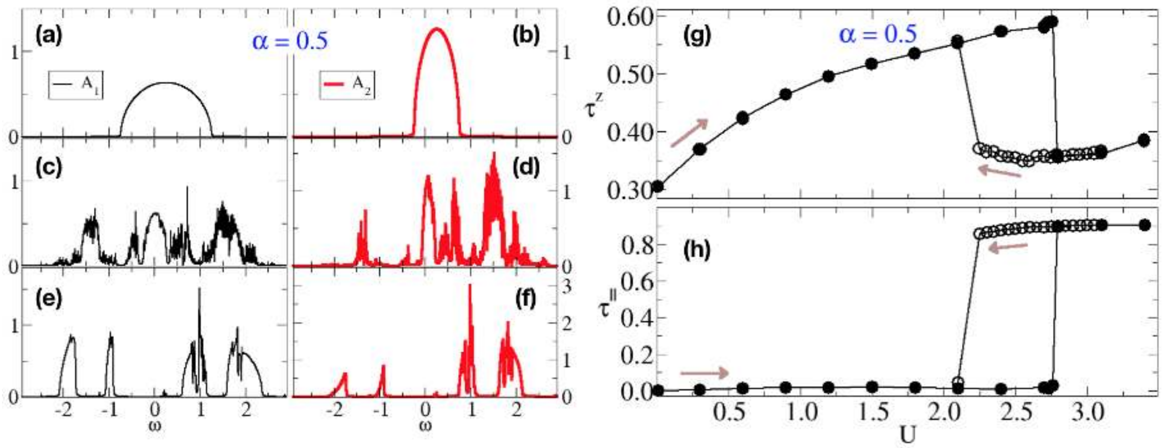

Figure 4.4: Panel (a)-(f): the spectral functions $A_a(\omega)$ for $\alpha = 0.5$ and sublattice $\Lambda = A$. Data for $a = 1$ ($a = 2$) are reported on the left (right) column. The results are for increasing values of U: $U = 0.0$ (panels (a), (b)), $U = 2.1 < U_{c1}$ (panels (c), (d)), $U = 3.1 > U_{c2}$ (panels (e), (f)). Orbital polarisation τ^z (panel (g)) and staggered in-plane component of the pseudospin $\tau^{||}$ (panel (h)) as function of the interaction strength U. Data are for $\alpha = 0.5$. The arrow indicate the direction in the hysteresis cycle.

which quantifies the degree of Mott's localization of quasi-particles, being $Z_a \to 1$ in the non-interacting limit and $Z_a \to 0$ at the Mott transition.

The results for Z_a are reported in Fig. 4.3 (b). In the weakly interacting regime the effects of the interaction are nearly identical on the two bands, i.e. $Z_1 \simeq Z_2$. However, upon increasing U, the two quantities start differentiating, with the wider band becoming more correlated than the narrower one, i.e. $Z_1 < Z_2$ [109], at odds with the paradigm of the orbital selective Mott transition [32]. At a critical value of U, the electrons on both bands localize, as signalled by the simultaneous vanishing of Z_1 and Z_2. We find that the metal-insulator Mott transition is first order. In the inset of Fig. 4.3 (b) we show that Z_a at the transition suddenly jump to zero, and we also observe a clear hysteresis loop. The coexistence region extends between $U_{c1} \simeq 2.20$ and $U_{c2} \simeq 2.80$.

A direct insight into the solution is obtained by the evolution of the spectral functions $A_a(\omega) = -\frac{1}{\pi}\mathrm{Im}G^{aa}_{\mathrm{loc}}(\omega)$ with $a = 1,2$, shown in Fig. 4.4 (a)-(f). At $U = 0$ the spectral functions have the typical semi-elliptical shape of the Bethe lattice. Upon increasing the interaction, see Fig. 4.4 (c)-(d), we observe at high-energy the gradual formation of the Hubbard sidebands, coexisting with the low-energy quasiparticle peaks. For $U > U_{c2}$ the system undergoes a transition into a Mott insulator. The corresponding spectral functions show a large gap around the Fermi level ($\omega = 0$) and the two Hubbard sidebands centered at about $\omega = \pm U/2$.

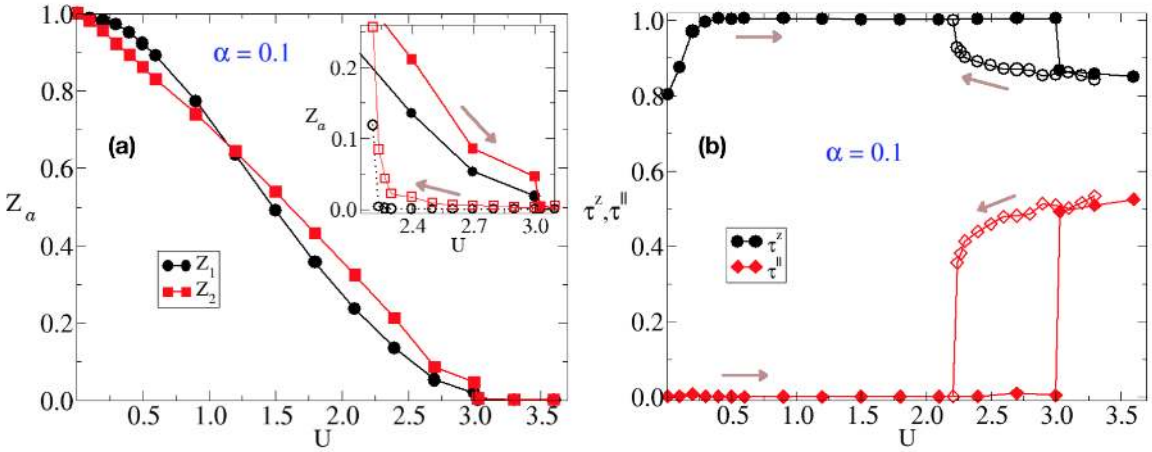

Figure 4.5: Panel (a): quasiparticle residues Z_a as function of U and for $\alpha = 0.1$. Inset: the same quantities near the first order transition. The arrows indicate the hysteresis cycle. Panel (b): uniform orbital polarisation, τ^z, and staggered one, $\tau^{||}$, as a function of U. Data are for $\alpha = 0.1$. The arrows indicate the hysteresis cycle near the Mott transition.

We note that in the Mott insulator the band 2 has still weight below the Fermi level, namely, unlike the mean-field expectation, we do not find a transition into a one-band model with maximum orbital polarisation. In Fig. 4.4 (g) and (h) we show the values of the uniform orbital polarisation, τ^z, and staggered one, $\tau^{||}$, as function of U across the Mott transition. We always find a finite uniform polarisation, but also an antiferro-orbital polarisation in the xy-plane, which we have denoted as canted AFO state (see Fig. 4.2 (b)). This result suggests that the observed degeneracy between the AFO along the z direction and the canted AFO mentioned in Sec. 4.1.1 is removed in favor of the canted AFO state.

In the non-interacting limit, $\tau^{||} = 0$ while the uniform orbital polarisation along z is finite, due to the different bandwidths of the two orbitals. In agreement with mean-field, upon increasing U the wide band population grows at expenses of the narrow one, thus leading to an increase of τ^z while $\tau^{||}$ remains zero. However this tendency does not proceed till a 2BM-to-1BM transition, i.e. till $\tau^z \to 1$; before that happens a first-order Mott transition takes place. At the transition, we find a sudden increase of $\tau^{||}$ to an almost saturated value $\tau^{||} \approx 0.9$, and, consequently, τ^z suddenly drops to a very small value, only slightly larger than the non-interacting one.

We now consider a smaller value of the bandwidth ratio, $\alpha = 0.1$. The large mismatch between the two bandwidth greatly enhances the occupation imbalance among the two orbitals, already in the uncorrelated regime. We start by the behaviour of the quasiparticle residues Z_a, shown in Fig. 4.5 (a). Differently from the previous $\alpha = 0.5$ case, the two bands have distinct Z_a already at relatively small values of U, now with the narrower band more correlated than the wider one. This behaviour is reversed at $U \simeq 1.2$, at which the wider more populated band 1 becomes also the most correlated one. Further increasing the correlation strength eventually drives the system into a Mott insulating state, as before through a first-order transition at which both quasiparticle residues drop to zero.

It is useful to compare the behaviour of Z_a with the evolution of the orbital polarisations τ^z and $\tau^{||}$, shown in Fig. 4.5 (b). For very small U the system is characterized by a large value of uniform polarisation, τ^z, and vanishing staggered one, $\tau^{||}$. By slightly increasing the interaction strength, the orbital polarisation rapidly saturates to $\tau^z = 1$. Concomitantly, the narrower band empties while the wider one reaches half-filling. Therefore correlation drives in this case a continuous topological Lifshitz transition from a 2BM to a 1BM, as predicted by the Hartree-Fock approximation. Interestingly, the narrower band keeps a high degree of correlations, as demonstrated by the decreasing behaviour of Z_2, see Fig. 4.5 (a). In other words, although essentially empty, the band 2 is not completely decoupled from band 1.

More insights can be gained by the behaviour of the spectral functions, shown in Fig. 4.6 (a)-(f). The large orbital occupation imbalance is already visible in the non-interacting limit, with the wider band being nearly centered around the Fermi level and, correspondingly, the narrower one nearly empty. Upon increasing the interaction U, the narrower band 2 gets shifted entirely above the Fermi level, yet it still shows spectral weight at high energy resulting from correlation effects. Simultaneously, the wider band recovers a particle-hole symmetric shape characterized by a three-peaks structure, with a renormalized central feature flanked by the two precursors of the Hubbard sidebands. For $U > U_{c2}$ a spectral gap opens in the the half-filled wider band signaling the onset of a Mott insulating state. Notably, also the previously empty narrow band shows the formation of a Mott gap which separates a large spectral feature above the Fermi level from a tiny spectral weight below it, see the arrows in Fig. 4.6 (f). The systems is thus characterized by $Z_1 = Z_2 = 0$ when it enters into the Mott state, see Fig. 4.5 (a). As for the larger values of α, the resulting insulating state has a finite in-plane staggered polarisation, $\tau^{||}$, and a reduced value of the uniform one, τ^z, see Fig. 4.5 (b).

In order to ascertain the strong-coupling picture of section 4.1.1, we study the evolution of the orbital order in the Mott insulator at large U. In Fig. 4.6 (g) we report the behaviour of both uniform, τ^z, and staggered, $\tau^{||}$, polarisations as function of α for $U = 5$. When $\alpha \to 0$, $\tau^z \to 1$ and $\tau^{||} \to 0$, while the opposite occurs for $\alpha \to 1$. The evolution between these two limits is continuous, namely the critical $\alpha_c = 0$. We note that those results do not change by decreasing or increasing the interaction strength, provided the system remains within the

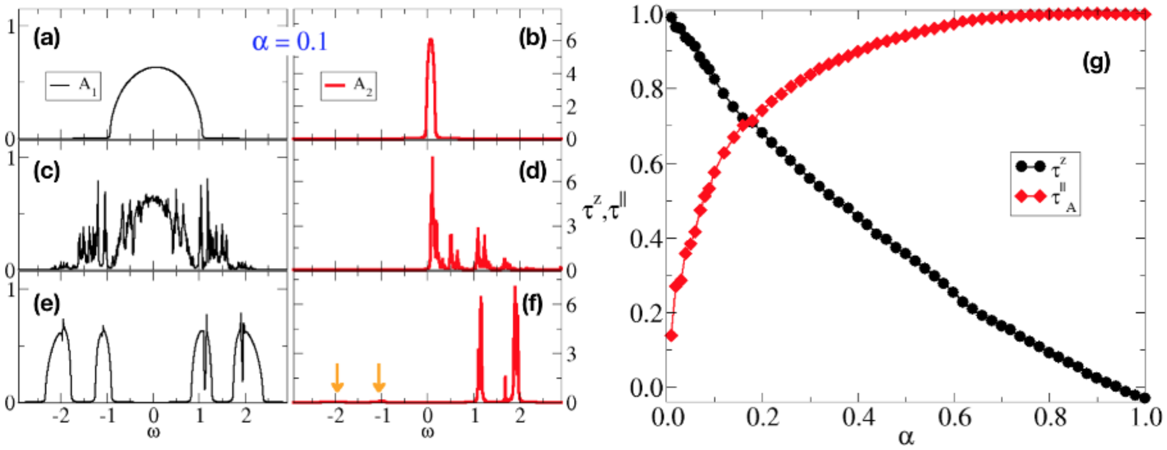

Figure 4.6: Panel (a)-(f): spectral functions for $\alpha = 0.1$ and fixed spin on sub-lattice A. Data are for increasing values of U: $U = 0.0$ (panels (a)-(b)), $U = 1.2$ (panels (c)-(d)) $U = 3.3$ (panels (e)-(f)). Note the different scales in the y-axis. Arrows in panel (f) indicate tiny spectral weight below the Fermi level for narrow band. Panel (g): Uniform orbital polarisation τ^z and staggered in-plane component of the pseudospin $\tau^{||}$ as function of α. Data are for $U = 5.0$.

insulating regime. This result further confirms the larger stability of the canted AFO with respect to the AFO along the z direction in the paramagnetic domain.

We summarize all previous results in the U-α phase-diagram of Fig. 4.7. We find three distinct phases: a metallic state at small U and large enough α in which both bands are occupied (2BM); a metallic phase at small U and α with a half-filled wider band and an empty narrower one (1BM); a canted AFO ordered Mott insulator at large enough interaction. The two metallic phases are connected through a continuous Lifshitz transition [110] associated to the correlation induced emptying of the narrow band. For a generic value of α, increasing the interaction U drives the system into a Mott state through a first-order transition. This transition is associated with a large coexistence region (grey shaded area) for $U_{c1} < U < U_{c2}$ [111]. The merging of the Mott and the Lifshitz transition lines is a tricritical point [112]. Interestingly, the insulator and the 1BM spinodal lines show a residual dependence on α. This reveals the strong entanglement between the two bands. Thus, although in the 1BM phase the wider band is half-filled and particle-hole symmetric, its description can not be simply reduced to that of a single-band Hubbard model.

This description is recovered only in the limit $\alpha \to 0$, where just the broader band is filled for each value of the interaction strength. We emphasize that the quarter filling condition $\langle n_{\mathbf{R}} \rangle = 1$ differentiates this model from the Falicov-Kimball one [113]. We find that the 1BM to Mott insulator transition at $\alpha = 0$ takes place continuously at $U_c = U_{c2}$, as in the DMFT description of the Mott transition in the single-band Hubbard model [29]. However, for any

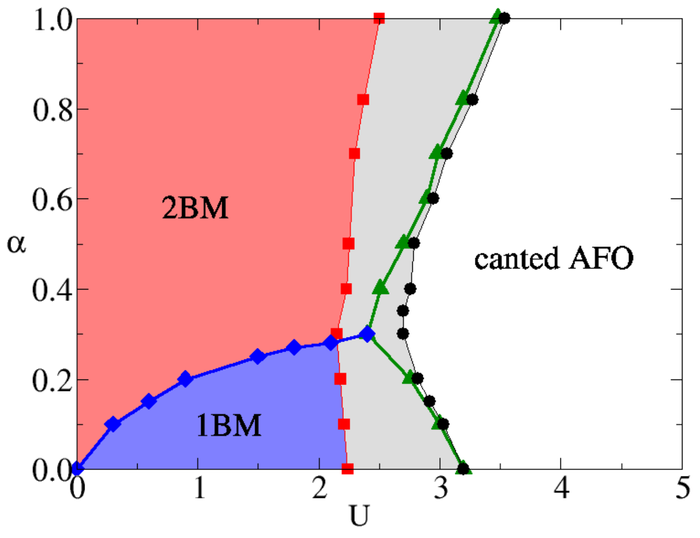

Figure 4.7: The non-magnetic phase diagram of the model in the U–α plane. Three different phases are present: a two-bands metal (2BM) at small U and large enough α; a one-band metal (1BM) for small α and small U; and a Mott insulator with canted AFO order. The 2BM phase is connected to the 1BM through a continuous topological Lifshitz transition (diamonds). The transition to the canted AFO ordered Mott insulator is of first-order. The spinodal lines (filled circles and squares) delimitate the coexistence region. The first-order critical line (filled triangles) is computed from the energy crossing of the two solutions. A tricritical point is present at the merging of the transition line.

non-zero α a finite staggered in-plane polarisation appears, and thus both bands are partially occupied.

4.3 Anti-ferromagnetic DMFT results

In the previous section we artificially prevented the DMFT solution to spontaneously break spin-$SU(2)$ symmetry and order magnetically, specifically into a simple Néel antiferromagnetic configuration since the lattice is bipartite and the Hamiltonian not frustrated. Here we shall instead leave the system free to order also magnetically, and study the interplay between spin and orbital orderings. Because of spin $SU(2)$ symmetry, all symmetry breaking directions are equivalent, and thus we choose for convenience the z-axis and define the staggered magnetization of orbital $a = 1,2$ as

$$m_a = \frac{1}{V}\sum_{\mathbf{R}\in A}\langle n_{\mathbf{R}a\uparrow} - n_{\mathbf{R}a\downarrow}\rangle - \frac{1}{V}\sum_{\mathbf{R}\in B}\langle n_{\mathbf{R}a\uparrow} - n_{\mathbf{R}a\downarrow}\rangle,$$

and the full staggered magnetization as $m = m_1 + m_2$.

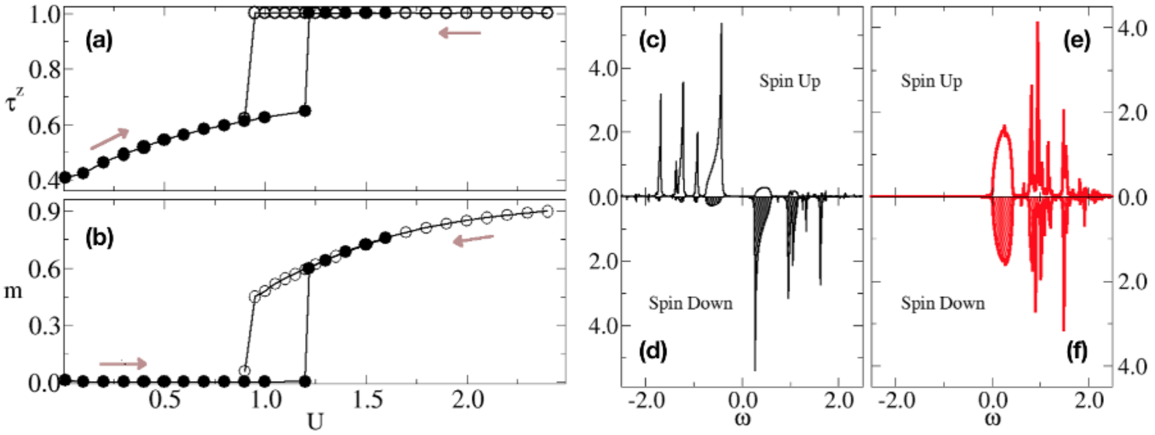

Figure 4.8: Panels (a)-(b): uniform orbital polarisation τ^z and staggered spin magnetization m as functions of the interaction U. Data are for $\alpha = 0.4$. The system undergoes a first-order transition from the 2BM to an antiferromagnetic (AFM) state, with finite m. The orbital polarisation saturates to $\tau^z = 1$ corresponding to a ferro-orbital (FO) ordering of the AFM state. The arrows indicate the directions of the solutions in the coexistence region $U_{c1}^{AFM} = 0.9 < U < 1.2 = U_{c2}^{AFM}$. Panels (c)-(f): Spin resolved spectral functions for $\alpha = 0.4$, sub-lattice $\Lambda = A$, corresponding to majority spin up, and $U = 1.6$. Data for the wide band are in panels (c)-(d), those for the narrow band in panels (e)-(f).

We start taking $\alpha = 0.4$. In Fig. 4.8 (a) and (b) we show the evolution of the uniform orbital polarisation τ^z and staggered magnetization m as function of U. By increasing the interaction from $U = 0$, τ^z slowly increases, but the system remains a paramagnetic 2BM, thus $m = 0$. For $U = U_{c2}^{AFM} \simeq 1.2$ we find a first-order transition to an antiferromagnetic (AFM) ordered state, signaled by the sudden increase of the staggered magnetization m. Concurrently, the uniform orbital polarisation saturates, $\tau^z = 1$. We thus find that the magnetic transition appear simultaneously with the emptying of the narrow band, as expected by the Stoner instability of a half-filled single band.
We can gain insight into the nature of the AFM phase at large U by looking at the spin resolved spectral functions of the two orbitals, shown in Fig. 4.8 (c)-(f). The wider band 1 has a particle-hole symmetric spectrum. Conversely, the narrower band lies entirely above the Fermi level.

We now study how the phase diagram changes with α. In Fig. 4.9 (a) and (b) we show the dependence upon α of the staggered magnetization and polarisation, m and $\tau^{||}$, respectively, and of the uniform orbital polarisation τ^z, deep in the insulating phase at $U = 4.5$. For $\alpha \lesssim 0.7$ we find the same behaviour as at $\alpha = 0.4$, $m \simeq 1$, $\tau^z \simeq 1$ and $\tau^{||} = 0$. Surprisingly, at $\alpha \simeq 0.7$ we observe a second order transition, above which also the orbital $U(1)$ symmetry breaks spontaneously and the model develops a finite staggered polarisation $\tau^{||}$. The staggered magnetization remains almost saturated, but now has contribution from both bands.

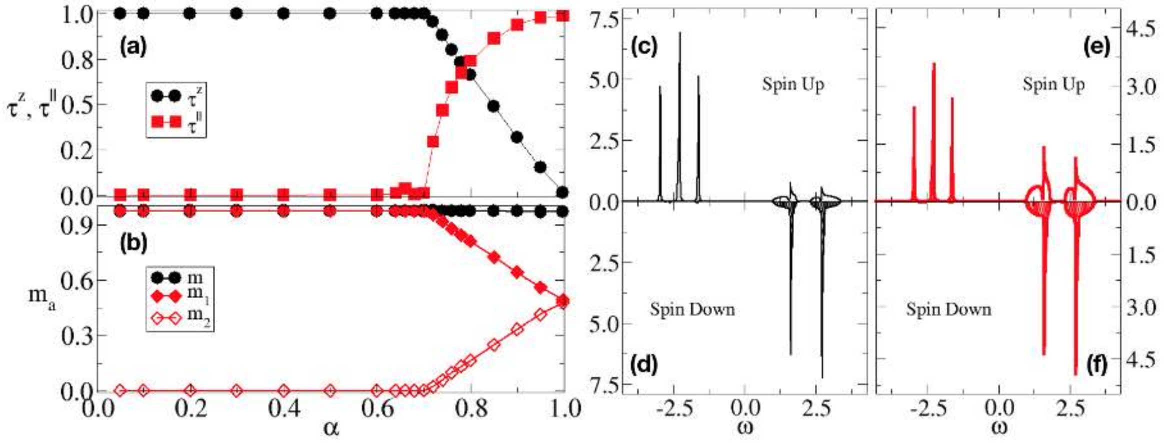

Figure 4.9: Panel (a): uniform orbital polarisation, τ^z, and staggered one, $\tau^{||}$, as function of α. Panel (b): total and orbital resolved staggered magnetization, m, m_1 and m_2, as function of α. Data are for $U = 4.5$. The solution displays a continuous transition from the ferro-orbital antiferromagnetic state to a canted antiferro-orbital but still antiferromagnetic state at $\alpha \simeq 0.7$. Panels (c)-(f): Spin-resolved spectral functions for $\alpha = 0.9$ on sublattice A, $U = 4.5$ for the wide band (panels (a) and (b)) and the narrow one (panels (c) and (d)).

Indeed, since for $\alpha < 1$ the solution corresponds to a canted AFO ordering, the system has a finite FO component along the z-direction of τ, ultimately giving rise to AFM correlations similar to the one-band case.

To get further insight in the nature of the AFM phase for $\alpha > 0.7$ we show in Fig. 4.9 (c)-(f) the spin- and orbital-resolved spectral functions at $\alpha = 0.9$. It is instructive to compare these data with those reported in Fig. 4.8 (c)-(f). For this larger value of the bandwidth ratio, the two orbitals have almost indistinguishable spectral functions, unlike below the transition at $\alpha \simeq 0.7$.

We summarize our findings in the magnetic phase-diagram drawn in Fig. 4.10. We find three distinct phases. At small U the 2BM is stable. For larger U an AFM ordered insulator sets in. The magnetic transition is first-order, with a coexistence region that shrinks on approaching $\alpha = 0$. The magnetic transition takes place for any α and for values of U smaller than those required in the absence of magnetism, i.e. $U_c^{AFM} < U_c$. In particular, as expected by comparison with the single-band Hubbard model, the 1BM region gets completely suppressed by the onset of AFM order. Moreover, the AFM phase is cut in two by a second order transition line associated with a change in orbital ordering. For $\alpha < 0.7$ the AFM has a saturated uniform orbital polarisation, in which only the wide band is occupied and contributes to the magnetic ordering. Increasing the bandwidth ratio above $\alpha \simeq 0.7$ leads to spontaneous orbital-$U(1)$ symmetry breaking, signalled by a finite in-plane staggered

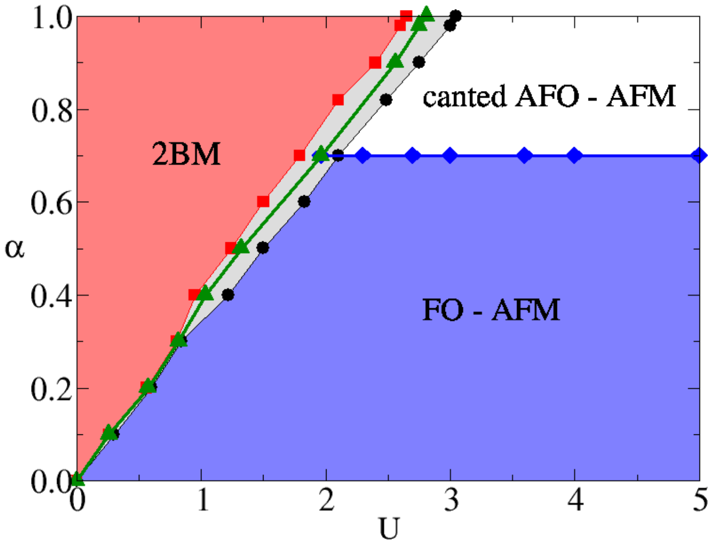

Figure 4.10: Magnetic phase-diagram of the model in the U-α plane. The phase diagram shows two main regions: a paramagnetic 2BM for small values of the interaction U and an AFM insulator for $U > U_c^{AFM}$. The magnetic transition is of the first-order. The (gray) shaded area indicates the coexistence region. The AFM phase is further divided in two by a continuous transition: an AFM with a canted AFO order for $\alpha > 0.7$, and an AFM with full orbital polarisation for $\alpha < 0.7$.

orbital polarisation. In this phase both bands are almost equally occupied and thus both contribute to the AFM order. Interestingly, we find that this transition is independent by the interaction strength U and that we can reproduce it at the mean field level by assuming a value $\varepsilon \approx 0.7$ for the spin-spin correlation parameter that appears in Fig. 4.3 (a).

We emphasize that the above results are valid as long as $\alpha < 1$. When $\alpha = 1$ the enlarged $SU(4)$ symmetry of the model may entail different type of spin-orbital orders [106] that we did not analyze.

4.4 Conclusions

Despite its simplicity, two quarter-filled bands with different bandwidths subject to a monopole Slater integral U, the model (4.2) shows a remarkably rich phase diagram once the interplay between orbital and spin degrees of freedom are fully taken into account. In particular, because of the bandwidth difference, the interaction U generates an effective crystal field that tends to empty the narrower band. This shows that correlations may not just enhance an existing crystal field, as pointed out in Ref. [114] in connection with the physics of V_2O_3, but even generate one despite its absence in the original Hamiltonian. The depletion of the narrower band continues till a topological Lifshitz transition occurs, above which only the wider band remains occupied and specifically half-filled. In our case study, with a bipartite lattice and unfrustrated Hamiltonian, as soon as the narrower band empties, a Stoner instability takes place driving the half-filled wider band into an antiferromagnetic insulator. This magnetic insulator still shows an active role of the orbital degrees of freedom that can drive a further phase transition between an insulator where only the wider band is occupied into another one where a canted antiferro-orbital order appears, and thus both bands are populated.

We argue that, in a generic situation where some degree of frustration is unavoidably present, either geometric or caused by longer range hopping integrals, the one-band metal, with only the wider band occupied, might remain stable till a finite U Mott transition, as we indeed found by preventing magnetism. We thus expect that the generic phase diagram must include, for not too strong repulsion U, a quarter-filled two-band metal separated from a half-filled one-band metal by an interaction-induced Lifshitz transition. Both metal phases must eventually give way to a Mott insulator above a critical U, whose precise magnetic and orbital properties will critically depend on the degree of frustration. We end emphasising that, at odds with the naïve expectation that a narrower band must also be the more correlated one, we here find right the opposite. This is due to the effective crystal field Δ^{eff} that progressively empties the narrow band and at the same time brings the broad band closer and closer to the half filling condition, enhancing the correlation effect on the wider band.

These results permit us to enlighten the concept presented in Chap. 1 of Mott insulator in disguise. Indeed, the Mott insulating phase of the model becomes well describable within an independent particle scheme as, e.g., Hartree-Fock, once symmetry breaking is allowed. Indeed, the Hartree-Fock approximation not only allows to rationalise the gradual depopulation of band 2 upon increasing the interaction U, but also the onset of antiferromagnetism, and the consequent insulating behaviour, as soon as band 2 empties completely thus leaving band 1 half-filled. Nonetheless, several features remain unaccessible to Hartree-Fock, for instance the discontinuous character of the transition at large α and thus large U, revealing the essential importance of the Mott physics.

Chapter 5

Vanadium dioxide: a Mott insulator in disguise

Electronic devices like MOSFETs based on conventional semiconductors are known to have intrinsic size limitations. A gate voltage adds carriers to a semiconductor on a surface layer whose thickness is of the order of the electrostatic screening length, which is usually short. This implies that, upon decreasing the size of the semiconductor device towards the nanometer scale, the carrier surface density becomes smaller and smaller, around $\sim 10^{12} \div 10^{14}\ 1/\mathtt{cm}^2$ [119], and thus also the ON/OFF ratio (the ratio between the flowing currents in the presence and absence of the gate voltage).

A possible route to overcome this limitation consists in using, instead of a semiconductor, a material that can go across a resistive phase transition by changing some external parameter, including a gate voltage. Mott insulators are evidently promising candidates for such a purpose. Indeed a Mott insulator has, typically, a bulk charge density of $\sim 10^{20} \div 10^{22}\ 1/\mathtt{cm}^3$ [120], all of which should become available to electric transport as soon as the insulator turns metallic. The use of Mott insulating materials instead of semiconductors in electronic devices is commonly referred to as Mottronics [121–123]. The most promising candidate for Mottronics is vanadium dioxide, which has the metal-insulator transition temperature $T_c \sim 340\ \mathtt{K}$ closest to room temperature, see Fig. 5.1 (a). This material has a large ON/OFF ratio that remains sizeable by scaling, as displayed in Fig. 5.1 (b) for a 200 nm layer. In that particular case the resistivity jump is about four orders of magnitudes, but for bigger samples jumps up to five orders of magnitudes are observed. Furthermore, the transition temperature can be controlled by strain, leading to highly customisable devices [124]. Changing the temperature is not the only way one can induce the phase transition: the metallic phase can be stabilised starting from the insulator even through the application of an electric field [125, 126, 117] or of a gate voltage in an electric-double layer transistor (EDLT) configuration

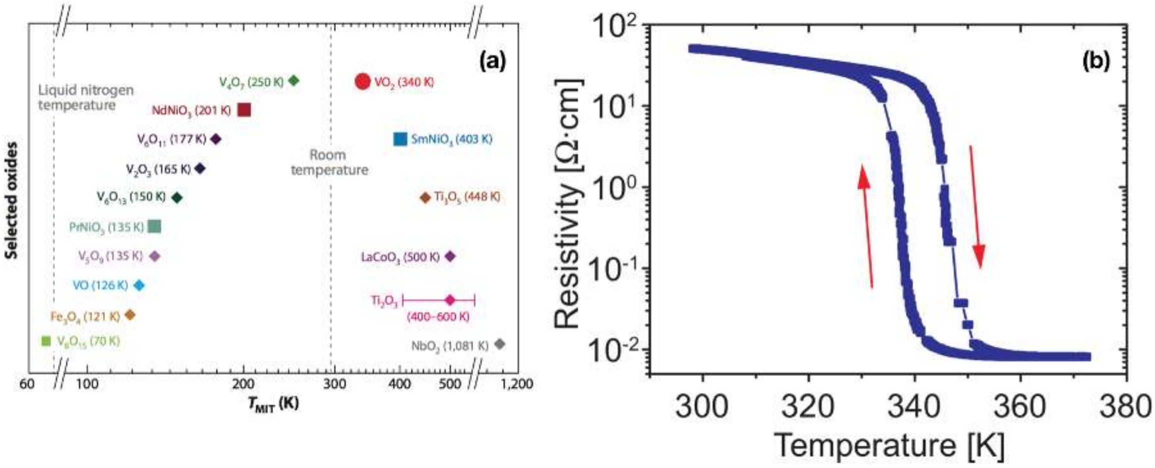

Figure 5.1: Panel (a): metal-insulator transition temperature for several TMO (adapted from [117]). Panel (b): resistivity as function of temperature for a 200 nm layer of VO$_2$ (adapted from [118]).

[127, 128]. For all those reasons, VO$_2$ has been massively studied both theoretically and experimentally since the seminal experiment by Morin in 1959 [67].

In this chapter, we would like to built and solve a simple model that can qualitatively describe the physics of VO$_2$. Before doing so, we shall need to review some properties of this compound.

5.1 Electronic and structural properties of VO$_2$

Simultaneously with the metal-to-insulator transition that occurs decreasing the temperature below $T_c \sim 340$ K, VO$_2$ undergoes also a structural distortion. The high temperature ($T > T_c$) crystal structure is shown in Fig. 5.2 (a); it is a rutile (R) structure with tetragonal symmetry. When $T < T_c$ the lattice structure becomes monoclinic, the so called M1 phase shown in Fig. 5.2 (b). In the M1 phase, pairs of vanadium atoms, originally aligned along the rutile c-axis, c$_R$, see Fig. 5.2 (a), tilt outside this axis and get closer to each other, see Fig. 5.2 (b). In other words, the chains of V along c$_R$ from being straight in the R phase become zig-zag and dimerised in the M1 phase.

Vanadium in VO$_2$ is in the ionic configuration V^{4+}:[Ar] 3d^1. The tetragonal crystal field of the rutile structure splits the 3d shell into a lower threefold degenerate t$_{2g}$ and a higher e$_g$ doublet. The t$_{2g}$ orbitals are shown in Fig. 5.2 (c), (d) and (e). The d$_{x^2-y^2}$ orbital, also called a$_{1g}$, has two lobes pointing towards the c$_R$ axis, and, since c$_R$/a$_R \sim 0.63 < 1$, it gives rise to a band with a pronounced quasi-one-dimensional character. On the contrary, the bands that derive from the d$_{xz}$ and d$_{yz}$ orbitals, so called e$_g^\pi$, are more isotropic.

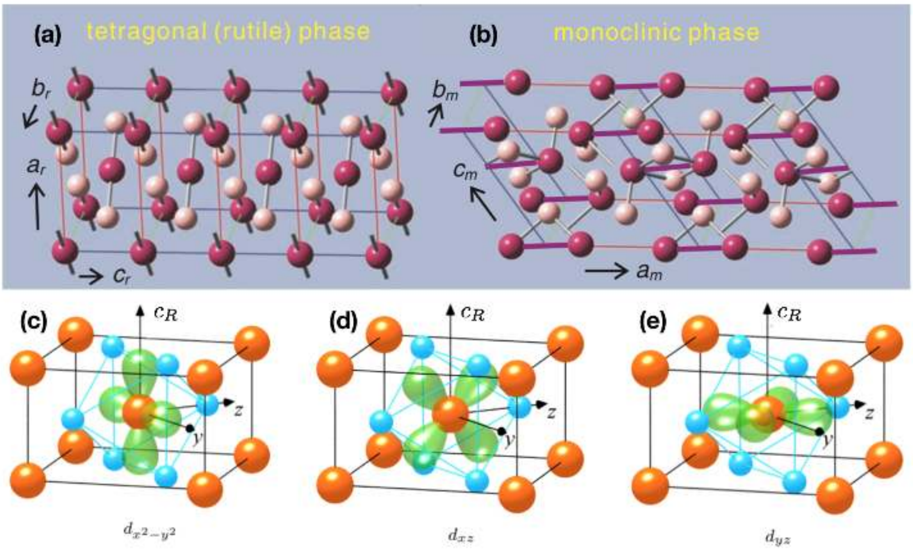

Figure 5.2: Panel (a): crystal structure of the metallic rutile (R) phase with tetragonal symmetry. Here red circles indicate vanadium atoms, instead white circles indicate oxygen atoms. Panel (b): crystal structure of the monoclinic (M1) insulating phase. Couples of vanadium atoms that were belonging to the c_R axis in the rutile phase, in the M1 crystal structure tilt outside it and dimerize. Panels (c), (d) and (e): orbitals of vanadium atoms that mainly contribute to the bands at the Fermi level. Orbital $d_{x^2-y^2}$ has two lobes that lie on the c_R axis. Panels (a)-(b) are adapted from [80], panels (c)-(e) are adapted from [129].

The pictorial representation of the density of states (DOS) of the metallic and insulating phases is shown in Fig. 5.3 (a) and (b), respectively. In the rutile metal, all three bands cross the Fermi level E_F. Note the shape of the a_{1g} DOS, evocative of a quasi one-dimensional system. In the monoclinic insulator, the e_g^π bands are pushed above the Fermi level, while the a_{1g} one is split into two sub-bands, the lower fully occupied and the upper empty. Optical measurements are shown in Fig. 5.3 (c). In the rutile metal, red curve, a Drude peak is observed at zero frequency, whereas in the M1 insulator, blue curve, there is an optical gap at low frequencies, and a first hump around 1.5 eV, denoted with letter A. This peak is believed to derive from the transitions between the lower a_{1g} sub-band and the e_g^π, see Fig. 5.3 (b). The second peak at 2.4 eV, denoted with letter B, is argued to correspond to the transitions between the two a_{1g} sub-bands, compare with Fig. 5.3 (b). The other structures in Fig. 5.3 (c) involve oxygen-p orbitals, not included in Fig. 5.3 (a) and (b).

We already mentioned in Chap. 2 that a satisfying description of the transition was given by Goodenough [81], which we briefly recall here. The structural change that occurs in the M1 phase can be conveniently viewed as an antiferroelectric distortion. Each vanadium atom moves away from the centre of the oxygen octahedron. The displacement has two components, one perpendicular and one parallel to c_R, and is staggered along that axis. The

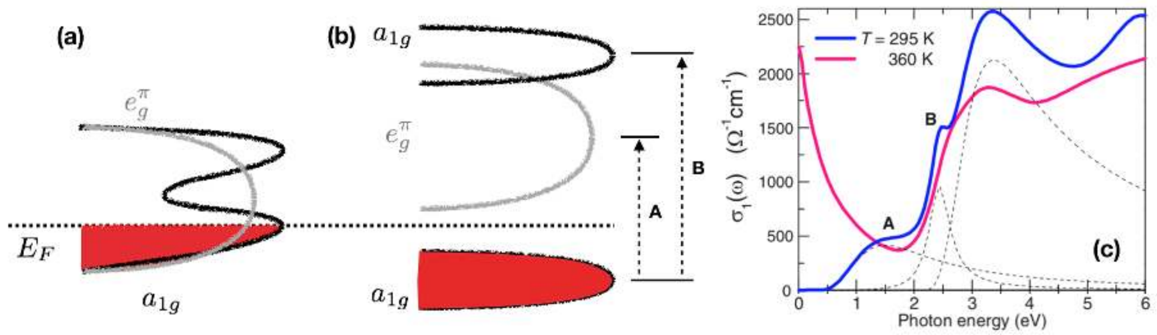

Figure 5.3: Sketch of the DOS in the metallic R phase, panel (a), and insulating M1 phase, panel (b). The dashed line indicates the Fermi level E_F of the system. Panel (c), adapted from [86], shows the real part of the optical conductivity of a 100 `nm` thick sample of VO_2 as function of frequency in the metallic (red) and insulating (blue) phases.

parallel displacement is thus responsible for dimerisation, whilst the perpendicular one of the tilting. The latter, in particular, has the indirect effect of pushing up in energy the e_g^π band much above the Fermi level, as demonstrated by the optical conductivity in Fig. 5.3 (c) and schematically shown in Fig. 5.3 (b). Once the e_g^π band empties, the quasi-one-dimensional a_{1g} one remains half-filled and dimerization, i.e., the displacement || to c_R, can dig a Peierls' hybridisation gap at the Fermi level between bonding and anti-bonding combinations as illustrated in Fig. 5.3 (b). The system thus becomes insulating.

However, Goodenough's view of the transition completely overlooks the contribution that may come from the interaction among the electrons. Several authors, as Mott and Friedman [130] and Zylbersztejn and Mott [82], pointed out the leading role of interaction in determining the gap size of vanadium dioxide. Particularly, they noticed that by slight substitution of V with Cr, $V_{1-x}Cr_xO_2$ enters into a new crystal structure, called M2, which is still insulating. The full phase diagram as function of the temperature and an applied uniaxial pressure (not dissimilar to Cr doping) is shown in Fig. 5.4 (b), and the crystal structures that appear therein are schematically depicted in Fig. 5.4 (a) [74]. The M2 phase is characterized by an alternation of undimerised zig-zag and dimerized straight chains. The phase indicated as T (a shorthand for transitional) has characteristics intermediate between the M1 and the M2 phases and connects them with continuity. The undimerised zig-zag chains show magnetic properties that are well described by a one-dimensional antiferromagnetic Heisenberg model, which can hardly be explained without invoking sizeable electron-electron interaction. Since the M2 phase is observed already for tiny tensile stress, Zylbersztejn and Mott concluded that the interaction in the M1 phase must have a similar strength. Moreover, the size of the optical gap in both phases is almost the same, suggesting that its origin might not be simply

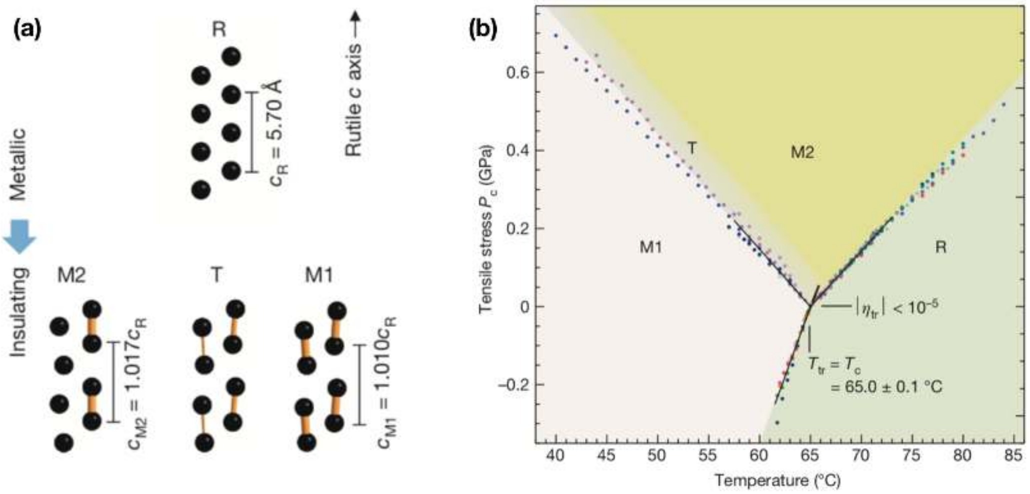

Figure 5.4: Panel (a): sketch of the crystal structures of vanadium dioxide that can be reached by changing its temperature and/or its tensile pressure (chemical doping). Panel (b): tensile stress-temperature phase diagram of VO_2. A positive tensile stress means that we are stretching the sample, a negative value means that we are squeezing it. The transition from the M1 to the M2 phase happens with continuity through the T phase. Adapted from [74].

the structural distortion [131].
One might, therefore, speculate, following Zylbersztejn and Mott, that the metal-insulator transition in vanadium dioxide is solely triggered by electronic correlations, rather than by the structural distortion as in Goodenough's scenario. This is actually not correct. Indeed, if the charge localisation were only due to correlations, the system should remain insulating also above the structural transition, while in reality it is metallic. We then conclude that the electronic correlations are necessary but not sufficient to explain the transition. Moreover, from the behaviour under chromium substitution as well as from the poor metal character of the R phase [132, 84, 133, 83], we must equally conclude that also the lattice distortion is necessary but not sufficient.

We end listing some facts about VO_2 that any theory must cope with:

- the presence of a metal phase above the structural transition;
- the strong first order character of the MIT [134–137, 67, 138];
- the mass divergence of the conduction electrons when the metal gets closer and closer to the insulating state [132, 84, 133, 83];
- the sizeable phonon contribution to the entropy across the transition [139];

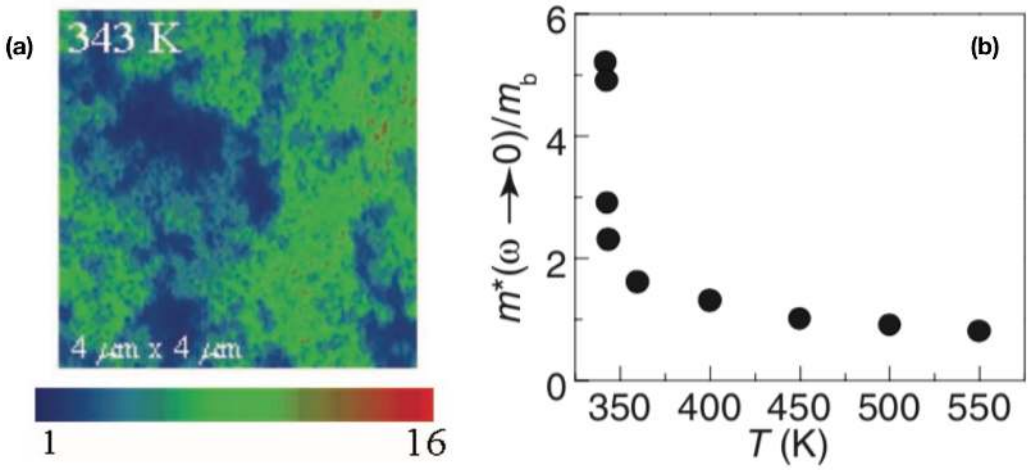

Figure 5.5: Panel (a): near-field scattering amplitude of a sample of VO_2 at 343 K. The red, green and light blue regions represent a metallic phase (where the scattering amplitude is larger), instead the dark blue ones represent an insulator. From the image it emerges the simultaneous presence of metallic and insulating clusters as expected for a first order phase transition. By lowering the temperature the insulating clusters start to nucleate, until they cover the whole sample at 341 K. Panel (b): evolution of the zero-frequency effective mass of the carriers in the metallic system as function of temperature with respect to the bare mass. Adapted from [84].

- the occurrence of a dynamical phase transition in non-equilibrium situations without any structural bottleneck (despite what previously reported) [140–142];
- the existence of an antiferromagnetic insulating phase (M2) for low applied uniaxial pressure or low values of chromium doping [77, 74];
- the almost independence of the gap size by the crystal structure of the different M1, M2 and T phases [82];
- the evidences of a monoclinic metal phase [143–146].

5.1.1 Evidences of a monoclinic metal

We here analyze in more details the aforementioned mass divergence in the metallic phase when the temperature is lowered down to T_c. Due to the first order character of the transition, when the system enters in the coexistence region, phase separation is expected. In such situation, it is not easy to understand which are the properties of the metallic and the insulating phases, separately, since usual experimental measurements provide only space-averaged quantities. The near-field scattering amplitude is shown in Fig. 5.5 (a) permits to distinguish the spatial regions that are metallic from those that are instead insulating, thus making

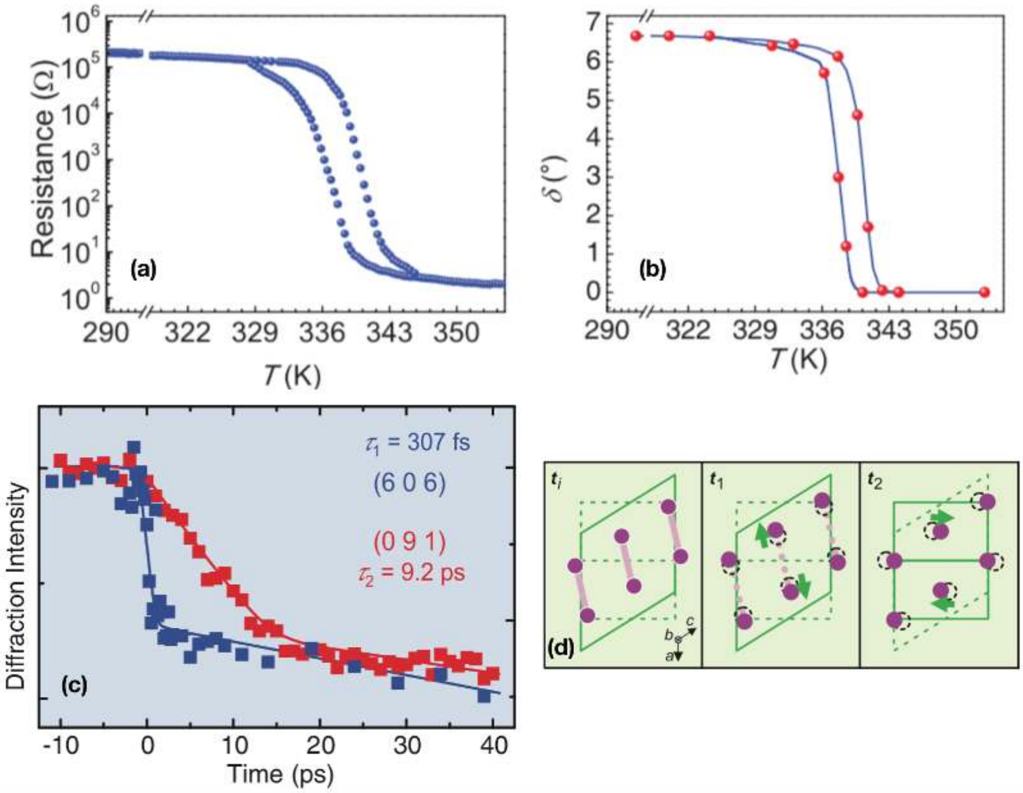

Figure 5.6: Panel (a) and (b): resistance and tilting angle δ of a monocrystal of vanadium dioxide at ambient pressure as function of temperature (adapted from [145]). Panel (c): time evolution of the intensity of two diffraction peaks of vanadium dioxide starting from the M1 phase after a sudden excitation. The blue line corresponds to a diffraction peak sensitive to the dimerization component of the crystal distortion, instead the red one to a peak sensitive to the tilting. The dynamics of the process is schematized in panel (d). At the initial time t_i the system is in the monoclinic M1 insulating phase, then, after the excitation, the dimerization melts at time t_1 and the tilting disappears after a longer time $t_2 > t_1$. Panel (c) and (d) are adapted from [80].

possible to study just the part of the sample with the desired properties. In this way, from the measurement of the real and imaginary parts of the optical conductivity, it was possible [84] to extract the mass renormalization of the carriers in the metallic islands, which we report in Fig. 5.5 (b). It is evident a large increase of the effective mass upon approaching the transition, as predicted by the Brinkman-Rice theory for the MIT [132]. This observation might also indicate a different character of the metallic phase when the coexistence region is approached.

Other experiments point out in a cleaner way that this last possibility is very meaningful. Fig. 5.6 (a) and (b) show the resistance of a single crystal of vanadium dioxide and the value of the tilting angle δ with respect to the c_R axis as function of temperature. From those images we infer that, by increasing the temperature, metallisation starts when the angle δ is still finite, meaning that the system passes through a monoclinic metal before reaching the rutile phase. Moreover, in Fig. 5.6 (c) we can observe the time evolution of two diffraction peaks after a sudden excitation due to a near-infrared pulse, which heats the system above the monoclinic-to-rutile transition. The blue and red lines correspond to diffraction peaks sensitive to dimerization and tilting, respectively. Since the characteristic time for the disappearance of the dimerization, $\tau_1 = 307$ `fm`, is found to be much shorter than that of the tilting, $\tau_2 = 9.2$ `ps`, one must conclude that the latter is far more stable than the former. Fig. 5.6 (d) shows a cartoon of the transition induced by the pulse, where at the initial time the system is in the monoclinic M1 phase. After a time τ_1, the dimerization melts, but only above τ_2 the tilting disappears. In equilibrium conditions, this would correspond to a larger critical temperature of the antiferroelectric component $\perp$ to c_R than that $||$ to c_R and responsible of dimerization. As a matter of fact, such observation was already done by Goodenough in his early work [81]. In view of those pieces of evidence, it is likely that the monoclinic metal phase observed in several experiments [143–146] has a crystal structure with tilting but no dimerization.

In conclusion, there are a wealth of experiments suggesting that a faithful modelling of vanadium dioxide should include the coupling with the two lattice distortions separately [147, 148].

5.1.2 Earlier theoretical works

We would like here to briefly review some of the main theoretical results obtained in the past years about vanadium dioxide. We will overlook the two milestones by Goodenough [81] and Zylbersztejn and Mott [82] since we already discussed them at length. We then start by recalling the argument by Rice, Launois and Pouget [149] to justify the importance of correlations in VO_2. As we said, in the M2 phase the chains that are not dimerised behaves magnetically as one-dimensional Heisenberg antiferromagnets. According to Rice, Launois and Pouget, they must be better viewed as Mott insulators since the Fermi surface does not display perfect nesting [150] and thus magnetism cannot arise by Stoner instability. Since the M1 structure can be interpreted as the superposition of the two types of lattice distortions present in M2, those authors concluded that M1 must be as correlated as M2, and both regarded as Mott insulators.

Another evidence of the importance of correlations comes from band structure calculations. Density functional theory (DFT) calculations based on local density approximation (LDA) or on generalized gradient approximation (GGA) are not able to reproduce the gap opening in the M1 and M2 phases [129]. Nonetheless, they can shed light on the electronic

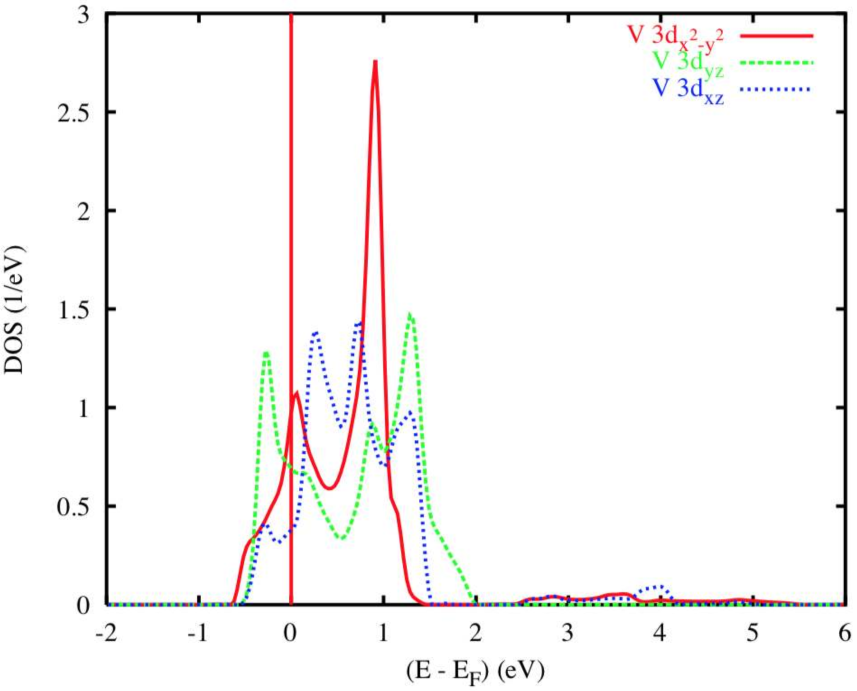

Figure 5.7: Density of states of the three t_{2g} states at the Fermi level of vanadium dioxide in the rutile structure, as obtained by LDA. Adapted from [129].

structure in the rutile phase. Fig. 5.7 shows the LDA density of states around the Fermi level projected onto the three t_{2g} orbitals [129]. The band with mainly $d_{x^2-y^2}$ orbital character has indeed a quasi-one-dimensional shape with two pronounced peaks, as we already mentioned. Also the d_{yz} DOS shows two peaks, though on average lower than the $d_{x^2-y^2}$ ones, which actually result from backfolding the bands from the Brillouin zone of the body-centred tetragonal lattice to the smaller zone of the simple tetragonal cell. We also note that the three bands have almost the same bandwidth, despite what was originally believed [82, 151].

LDA+U calculations can instead reproduce the opening of the gap in both insulating states of VO_2, but they predict an antiferromagnetic ground state not only for the M2 but also for the M1 structure [152, 153]. More refined DFT calculations based on hybrid functionals that improve the exchange energy are instead able to reproduce the gap opening in both the M2 and M1 phases with the proper magnetic properties [30]. As mentioned in Chap. 1, we expect that a single particle approach can reproduce the low temperature broken symmetry phase even of Mott insulators, though this does not answer the key question about the driving force of the MIT in VO_2.

Single-site paramagnetic DMFT calculations showed that an insulating phase can be stabilised without the inclusion of the lattice degrees of freedom, though that requires an unrealistically large value of the Hubbard repulsion ~ 25 `eV` [154]. Once again, this result demonstrates that the lattice must play an important role in VO_2.

Many other theoretical works attached this issue combining *ab initio* methods with DMFT, which is believed to account for the short-range effects of the interaction better than straight DFT-LDA. Since the unit cell of insulating VO_2 contains more than one vanadium, cluster DMFT was implemented. By means of this technique, the authors of Ref. [69] pointed out that strong correlations actually enhance the tendency towards spin-Peierls dimerisation via non-local self-energy corrections, thus explaining the gap opening in the M1 phase. The important role of correlations also in the metal R phase was later highlighted by a calculation based on DFT-LDA combined with single-site DMFT [155], which showed a substantial increase of the effective mass by decreasing temperature, in qualitative agreement with the data shown in Fig. 5.5 (b). Soon after, it was suggested [154] that a possible mechanism able to explain the transition is an orbital selective Mott transition driven by a Peierls distortion. Such possibility was however confuted by a subsequent DMFT study [70] that instead argued for the crucial role played by Mott's localisation in conjunction with a strong inter-site exchange, partly confirming the prediction by Rice, Launois and Pouget.

Therefore, despite those state-of-the-art calculations, existing results are still quite controversial, and it is not easy to find any common framework. This is the reason why it might be better to come back to a simple minimal model that can describe the essential features of the transition in a transparent way. This approach was recently attempted in [156, 71, 73], where it is argued that the dimer Hubbard model (DHM), essentially a single-band Hubbard model at half-filling with a two-atom unit cell, can provide a good description of VO_2. This model, however, ignores completely the e_g^π bands and includes from the start an explicit dimerisation, hence it cannot describe the structural transition accompanying the metal-insulator transition. Other models were actually studied in the past [157, 158, 151], in which lattice deformation is explicitly taken into account. In most cases a simplified Born-Oppenheimer approach is used, where the electronic Hamiltonian at fixed phonon displacement is solved to provide an additional contribution, besides the elastic energy, to the lattice potential, whose minima identify the equilibrium states. Despite the interesting results thus obtained, the models studied therein lacks some ingredients that, in our opinion, may be important, or include others that do not seem to be present according to experiments and *ab-initio* calculations. For instance, in [157] a single-band model was studied without any electron-electron interaction; in [158] a two-band model was considered in which the electrons are coupled just to a dimerizing mode without any electron-electron interaction. The most comprehensive analysis was presented in [151] on a three-band Hubbard model that includes the coupling with a single mode that however induces both dimerisation of the a_{1g} band and the splitting between the latter and the e_g^π one. The a_{1g} bandwidth was assumed smaller than the e_g^π one, which is not compatible with *ab-initio* results, and the interaction treated within Hartree-Fock. The model we are going to present is actually quite close to the previous one, though we shall handle with interaction in a better way through DMFT.

5.2 The model

We consider a quarter filled two-band Hubbard model. One band, the band 1, is meant to describe the a_{1g}, while the other, band 2, the e_g^π. We shall thus ignore the fact that the e_g^π is, in reality, a doublet, which we believe is not essential. We further add two classical dispersionless lattice modes: one, with coordinate X_1, opens a dimerisation gap in the a_{1g}, while the other, with coordinate X_2, modulates the crystal field splitting between the two orbitals.

The model Hamiltonian is

$$H = H_{el} + H_{el-ph} + H_{ph} \,. \tag{5.1}$$

H_{el} is the purely electronic part and reads

$$H_{el} = \sum_{a=1}^{2} \sum_{\boldsymbol{k}} \left(\varepsilon_{a,\boldsymbol{k}} - \mu\right) n_{a,\boldsymbol{k}} + \frac{U}{2} \sum_i n_i \left(n_i - 1\right) , \tag{5.2}$$

where $n_{\boldsymbol{k},a}$ is the occupation number at momentum $\boldsymbol{k}$ of the orbital $a = 1,2$, n_i the total electron number operator at site i, μ the chemical potential that enforces the quarter filling condition, and finally U the on-site Hubbard repulsion. In order to emphasise the quasi-one-dimensional character of band 1 as opposed to band 2, we assume the following density of states (DOS):

$$\begin{aligned} D_1(\varepsilon) &= \frac{1}{\mathscr{N}} \left[a\varepsilon^2 - b\varepsilon^4 + D^2\left(bD^2 - a\right)\right] , \\ D_2(\varepsilon) &= \frac{2}{\pi D} \sqrt{1 - \left(\frac{\varepsilon}{D}\right)^2} \,, \end{aligned} \tag{5.3}$$

with $\varepsilon \in [-D, D]$ and $\mathscr{N}$ a normalisation factor. We take $b > a/D^2 > 0$ so that $D_1(\varepsilon)$ has a double-peak structure evocative of a one-dimensional DOS [151]. Hereafter, we shall take $D = 1$ the energy unit, and fix $aD^3 = 1.9$ and $bD^5 = 2.1$. The resulting DOS's are shown in Fig. 5.9 (a) and (b). We have deliberately chosen the two bands with the same bandwidth as well as centre of gravity, which is indeed suggested by *ab-initio* calculations in the R phase and as also the advantage of better highlighting the interplay of interaction and electron-phonon coupling. Moreover, in Eq. (5.2) we just include the monopole Slater integral $U > 0$, and neglect higher order multipoles responsible of Hund's rules as well as the long-range part of the Coulomb interaction. This approximation, that makes the analysis more transparent, is justified for the values of $U \leq 1.5$ that we shall use.

The classical potential of the lattice, see Eq. (5.1), written as a Ginzburg-Landau theory for the antiferroelectric phase transition [147, 148], has the following expression, valid up to the sixth order in the phonon displacements,

$$\begin{aligned} H_{ph} &\equiv \Phi(X_1,X_2) \\ &= N\left(\frac{1}{2}\alpha\left(X_1^2+X_2^2\right)+\frac{1}{4}\beta_1\left(2X_1X_2\right)^2+\frac{1}{4}\beta_2\left(X_1^2-X_2^2\right)^2+\frac{1}{6}\gamma\left(X_1^2+X_2^2\right)^3\right), \end{aligned} \tag{5.4}$$

where N is the number of sites. The term proportional to β_1 favours a deformation of the lattice that involves just one of the two modes, while the term proportional to β_2 prefers deformations in which $|X_1| = |X_2|$. In the specific example of VO_2, $\beta_2 > \beta_1$, i.e., it is preferable to equally displace both modes [148] rather than just one of them. The electron-phonon coupling can be written as:

$$\begin{aligned} H_{el-ph} &= -gX_1\sum_{\boldsymbol{k}\sigma}\left(c^\dagger_{1,\boldsymbol{k},\sigma}c_{1,\boldsymbol{k}_*,\sigma}+H.c.\right)-\frac{\delta}{2}X_2^2\sum_i\left(n_{1,i}-n_{2,i}\right) \\ &\equiv -gX_1\,\mathscr{O}_{\text{dimer}}-\frac{\delta}{2}X_2^2\,\mathscr{O}_{\text{c.f.}}, \end{aligned} \tag{5.5}$$

where $c_{1,\boldsymbol{k},\sigma}$ creates an electron at the momentum $\boldsymbol{k}$ in band 1 with spin σ, and $\boldsymbol{k}_*$ is the particle-hole conjugate of $\boldsymbol{k}$ such that $\varepsilon_{1,\boldsymbol{k}} = -\varepsilon_{1,\boldsymbol{k}_*}$. The quadratic coupling in the crystal field term is intentional and has a simple physical explanation. The tilting component of the antiferroelectric distortion in the M1 phase corresponds to the displacement of vanadium away from the centre of the oxygen octahedron, parallel to the diagonal of the rutile basal plane. As a result, the hybridisation between the e_g^π and the p-orbitals of the oxygens closer to the new displaced vanadium position increases, while that with the further oxygens decreases. Such hybridisation change has the net effect of raising the e_g^π level of a quantity that is quadratic for small displacements, hence the expression in Eq. (5.5). Since the Hamiltonian is invariant under $X_1 \to -X_1$ and $X_2 \to -X_2$, we shall for simplicity study only the case with $X_1, X_2 > 0$.

Before presenting our results, that we obtained by DMFT, we shall here briefly discuss some general properties of the model that can be anticipated by simple arguments. Since we assume classical phonons, and neglect their kinetic energy, the problem reduces to find the minima of the potential

$$\begin{aligned}\Phi_{\text{eff}}\big(X_1,X_2\big) &= \Phi\big(X_1,X_2\big) + \langle H_{el}\rangle - g\,X_1\,\langle \mathscr{O}_{\text{dimer}}\rangle - \frac{\delta}{2}\,X_2^2\,\langle \mathscr{O}_{\text{c.f.}}\rangle \\ &\equiv \Phi\big(X_1,X_2\big) + E\big(X_1,X_2\big)\,,\end{aligned} \tag{5.6}$$

where the expectation values are calculated on the ground state of the Hamiltonian $H_{el} + H_{el-ph}$ at fixed U, X_1 and X_2. Let us try to infer how the electronic contribution $E\big(X_1,X_2\big)$ may depend on the phonon coordinates. At $U = 0$, the difference in DOS shapes of the two bands implies that band 1 is more populated than band 2, so that $\langle \mathscr{O}_{\text{c.f.}}\rangle \equiv O_{\text{c.f.}}\big(X_1,X_2\big) > 0$, is finite already for $X_2 = X_1 = 0$. For small displacements, such that linear response theory is valid,

$$E\big(X_1,X_2\big) \simeq E\,(0,0) - \frac{\delta}{2}\,X_2^2\,O_{\text{c.f.}}\big(0,0\big) - \frac{1}{2}\,\chi_{\text{dimer}}\,g^2\,X_1^2 - \frac{1}{8}\,\chi_{\text{c.f.}}\,\delta^2\,X_2^4\,, \tag{5.7}$$

where χ_{dimer} and $\chi_{\text{c.f.}}$ are the thermodynamic susceptibilities in the corresponding channels, the mixed one being absent since the two bands are not hybridised with each other. We thus expect a softening of both modes, whose spring constants changes into $\alpha_1 = \alpha - g^2\,\chi_{\text{dimer}}$ for X_1, and $\alpha_2 = \alpha - \delta\,O_{\text{c.f.}}\big(0,0\big)$ for X_2. In addition, a quartic term in X_2 appears, whose strength is larger the larger the electronic susceptibility to a crystal field splitting is. We note that the dimerisation susceptibility $\sim \ln|\mu|$, where $|\mu|$ is the distance between the centre of band 1 DOS, that we assume to be the zero of energy, and the chemical potential $\mu < 0$.

If U is finite but very small, the Hartree-Fock approximation can be safely used. Within Hartree-Fock, the main effect of U is to lower the energy of occupied states and raise that of unoccupied ones. It follows that $O_{\text{c.f.}}\big(0,0\big)$ grows with U, so that mode X_2 gets even softer. Concurrently, since band 2 empties more and more, the chemical potential moves closer to the centre of band 1, hence the dimerisation susceptibility grows. Beyond Hartree-Fock, the interaction U causes also a narrowing of the quasiparticle bandwidth, which implies a further increase of both susceptibilities, especially of $\chi_{\text{c.f.}}$ that behaves similarly to the magnetic susceptibility, one measuring the response to a field that splits the orbital index but not the spin, and the other vice versa. If the dimerisation coupling $g = 0$, further increasing U is thus expected to make phonon X_2 softer and softer, and, at the meantime, larger and larger the strength of the quartic term, which might result into a new minimum appearing in $\Phi_{\text{eff}}\big(X_1,X_2\big)$ at $X_{2*} > 0$, and coexisting with that in the origin if α_2 is still positive. Should such minimum being the absolute one, it would correspond just to a monoclinic metal phase with a depleted band 2. For X_{2*} above a critical value X_{2c}, band 2 empties completely and thus band 1 becomes half-filled, the chemical potential thus reaching zero. In this case and as

soon as $g \neq 0$, also X_1 will displace from the origin and dig a dimerisation gap within band 1, thus leading to the expected insulating behaviour. Even in such a circumstance, a minimum in the origin might still be present.
The above simple-minded discussion already suggests that our model Hamiltonian might indeed reproduce the actual physics of VO_2, as we shall further confirm by a straight DMFT calculation. In order to simplify that calculation, in the following we shall consider just one phonon mode, essentially enforcing the condition $X_1 = X_2 = X$ that corresponds to the preferential direction for a finite displacement, see Eq. (5.4). We shall further neglect β_1 and γ terms in Eq. (5.4), and thus write

$$\Phi\big(X_1, X_2\big) \to \Phi(X) = \frac{k}{2} X^2 . \tag{5.8}$$

and

$$\begin{aligned} H_{el-ph} = &- gX \sum_{\boldsymbol{k}\sigma} \left(c^\dagger_{1,\boldsymbol{k},\sigma} c_{1,\boldsymbol{k}_*,\sigma} + H.c. \right) \\ &- \frac{\delta}{2} X^2 \sum_i \left(n_{1,i} - n_{2,i} \right) , \end{aligned} \tag{5.9}$$

Even with these simplifications, the model Hamiltonian Eq. (5.1) has several parameters to be fixed. We shall take $U = 1.5$, in units of the half bandwidth, which is similar to the value estimated and used in the literature [159, 160, 151] taking into account that the realistic value of the half-bandwidth, our energy unit, is $D \simeq 1\texttt{eV}$. The other parameters, which involve the phonon coordinate, are chosen to be $g = 0.4$, $\delta = 0.05$ and $k = 0.2$, values that provide results compatible with estimates of the electron-phonon coupling [161, 158], and of the lattice energy change across the rutile-to-monoclinic transition [162].

5.3 DMFT results

As mentioned, we have solved this problem by single-site ED DMFT (see Chap. 3) with a bath up to 8 levels. We start by presenting the zero-temperature results and then we move to the analysis of the finite temperature ones.

In Fig. 5.8 we show the evolution of the effective potential Eq. (5.6) as function of the displacement X for several values of U. For each U, even in the non-interacting case, the potential displays two minima, one at $X = 0$ that is always metallic, and one at $X \neq 0$ that is

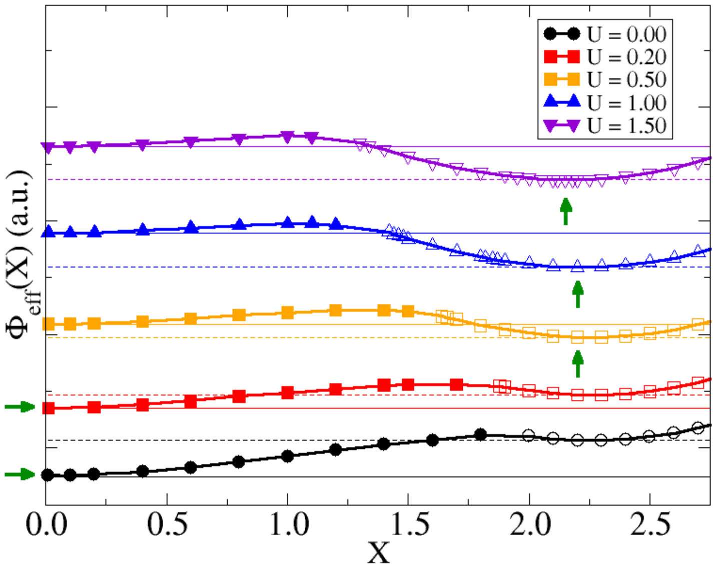

Figure 5.8: Zero-temperature internal energy of the system (in arbitrary units) as function of the amplitude of the crystal distortion X for several values of the Hubbard interaction U. Filled (open) symbols correspond to a metallic (insulating) solution. The continuous (dashed) horizontal lines indicate the values of the metallic (insulating) minimum at each value of U. Arrows indicate the position of the absolute minimum for each value of the interaction.

instead always insulating. The absence of a distorted metallic phase is likely a consequence of using a single variable X rather than two as before. When U is sufficiently small ($U \lesssim 0.5$) the stable phase of the system is the undistorted metal at $X = 0$; the other minimum at finite X thus corresponds to a metastable phase. For bigger values of $U \gtrsim 0.5$ the situation is reversed: the stable phase is now the distorted insulator, while the metal at $X = 0$ is metastable. These results highlight the fundamental role of interaction in stabilising an insulating and distorted ground state, in qualitative accordance with the phase diagram shown in Fig. 5.4 (b).

More insight about the two coexisting solutions can be gained by looking at the spectral functions $A_a(\omega) = -\frac{1}{\pi} Im\, G_{loc,aa}(\omega)$ for $a = 1,2$. In the non-interacting case at $U = 0$ the spectral functions at the two minima are shown in Fig. 5.9. As mentioned, the different shape of the DOS leads to a population imbalance even at $X = 0$, when $n_1 \sim 0.61 > n_2 \sim 0.39$. In the insulating minimum at $X = 2.30$, band 1 is split into a bonding σ ($\omega \sim -0.35$) and anti-bonding σ^* ($\omega \sim 1.95$) combinations by the phonon, see Fig. 5.9 (c). On the contrary, band 2 is pushed above the Fermi level, see Fig. 5.9 (d). As a result, the σ orbital is fully occupied, while band 2 and the uppermost σ^* are empty. This behaviour shows that the presence of a distorted dimerised insulator is possible also without interaction in such simple model and with our choice of Hamiltonian parameters, even though this insulating phase is metastable.

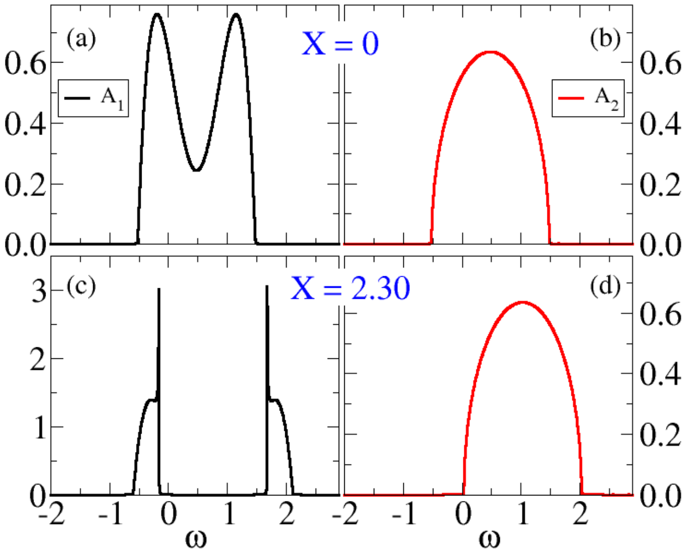

Figure 5.9: The spectral functions $A_a(\omega)$, a$= 1,2$ for the two minima observed in Fig. 5.8 for $U = 0$. The metallic phase corresponds to $X = 0$ [(a) and (b)], while the insulator to $X = 2.30$ [(c) and (d)].

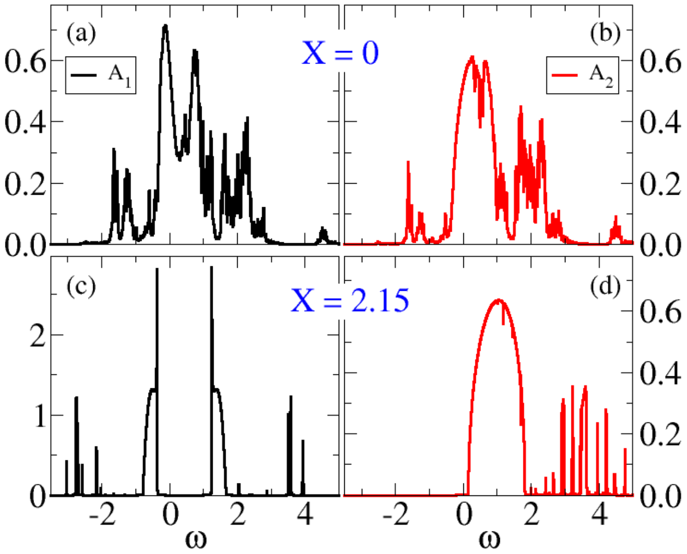

Figure 5.10: The spectral functions $A_a(\omega)$, a$= 1,2$ for the two minima observed in Fig. 5.8 for $U = 1.5$. The metallic phase corresponds to $X = 0$ [(a) and (b)], instead the insulator corresponds to $X = 2.15$ [(c) and (d)].

For $U = 1.5$, which we mentioned is a reasonable estimate of the realistic value in VO_2, the situation is the opposite, the distorted insulator is the stable phase, whereas the undistorted metal is metastable. In the latter both bands start to show the presence of Hubbard side bands, see Fig. 5.10 (a) and (b). At the stable insulating minimum, located at $X = 2.15$, see Fig. 5.10 (c) and (d), the weight of the Hubbard bands seems considerably smaller than that observed in the metallic solution. On the contrary, the size of the gap between σ and band 2 is instead bigger than in the metastable insulating phase at $U = 0$. This behaviour is actually common: once the Mott insulator is allowed to break a symmetry, in the present case $X \to -X$, in order to freeze the residual degrees of freedom, it partly undresses from correlations and ends to resemble more to a conventional band insulator, like the $U = 0$ metastable one in our case study. On the contrary, the dimerisation gap between σ and σ^* is smaller than in the metastable insulator at $U = 0$. This is also not surprising since this is actually a hybridisation gap that must be renormalised downwards by the short-range repulsion. The minimal gap, to be identified with the optical one, separates the filled σ band from the empty band 2, in agreement with experiments, and its value $E_{gap} \sim 0.5$, in units of $D \simeq 1$ `eV`, is not far from the experimental one $E_{gap}^{ex} \sim 0.6$ `eV` [78, 86], which supports our choice of parameters.

In order to get further insights about the degree of correlation, one can study the quasiparticle residues in the metallic phase:

$$Z_a = \left(1 - \frac{\partial \mathrm{Re}\Sigma_{aa}(\omega)}{\partial \omega}\right)^{-1}_{|\omega=0}, \tag{5.10}$$

with $a = 1,2$. The two bands show almost the same value of this quantity and, at $X = 0$, we get $Z_a \sim 0.68$ for both $a = 1,2$, actually consistent with other calculations [160, 155, 154], indicating an intermediate degree of correlation.

We now move to finite temperature T and study the evolution of the free energies corresponding to each of the two minima observed at zero temperature. We compute the entropy as function of T through the equation

$$S(X,T) = \int_0^T dT' \, \frac{1}{T'} \frac{\partial \Phi_{eff}(X,T')}{\partial T'} = \int_{\Phi_{eff}(X,0)}^{\Phi_{eff}(X,T)} \frac{d\Phi_{eff}}{T'\left(\Phi_{eff}\right)}, \tag{5.11}$$

which requires the knowledge of the internal energy that we actually calculate. Estimating the elastic constants through the curvature of each minimum at $U = 1.5$, we find a value ~ 0.02 in the undistorted metal phase, and a larger one ~ 0.10 in the distorted insulator at $X = 2.15$. This result implies softer phonons, hence larger entropy, in the metal than in the insulator, in accordance with experimental estimates [139]. However, since our modelling of

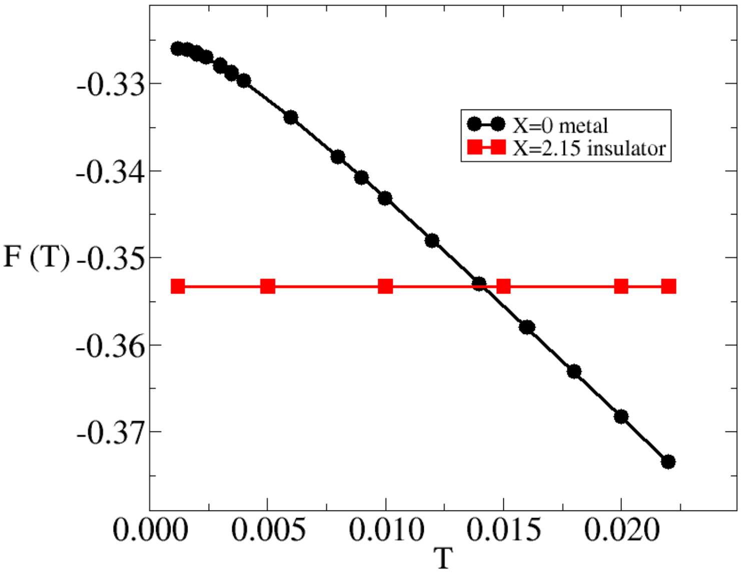

Figure 5.11: Free energy as function of temperature T at the two minima $X = 0$ and $X = 2.15$ observed at zero temperature for $U = 1.5$. The first order transition occurs at $T_c \sim 0.014$.

the distortion is oversimplified with respect to reality, we preferred not include the phonon contribution to the entropy, thus underestimating the metal free energy. In addition, we checked for same values of T that the position in X of the insulating minimum does not move appreciably with temperature since the internal energy does so. For this reason, we kept fixed the displacement of the insulating phase at its $T = 0$ value $X = 2.15$ at $U = 1.5$, see Fig. 5.8.

The free energy $F(X,T) = \Phi_{eff}(X,T) - T\,S(X,T)$ is shown in Fig. 5.11 for $X = 0$ and $X = 2.15$ at $U = 1.5$. We observe a crossing at $T_c \sim 0.014$, signalling a first order phase insulator-to-metal transition. Below T_c, the free energy of the distorted insulating phase is lower than that of the metal at $X = 0$. Above T_c the situation is reversed: the metal at $X = 0$ becomes the most stable phase, whilst the distorted insulator turns metastable. By converting in Kelvin the temperature T_c, we get $T_c \sim 162$ `K`, of the same order of magnitude as the experimental value, once again supporting our choice of parameters.

5.4 Conclusions

Despite its simplicity, the model Hamiltonian Eq. (5.1) seems able to catch some of the main physical properties of vanadium dioxide. We obtained the right order of magnitude for several quantities, such as the band gap of the monoclinic phase, the transition temperature, the energy separation of the bonding and anti-bonding bands and the renormalisation of the bands in the undistorted metal. Moreover, the model leads to a first order insulator-to-metal transition upon increasing the temperature or lowering the interaction. The insulating phase has also the experimentally observed inter-band gap. From our results, it thus emerges that the insulating M1 phase of VO_2 is another example of a Mott insulator in disguise, since, despite its resembling a Peierls's dimerised band insulator, it would not be a stable phase without the interaction U.

Chapter 6

NCA and OCA impurity solvers

In recent years the possibility to create ultrashort laser pulses with a duration of the order of the femtosecond opened the way to the realization of *ultrafast* experimental setups, the most common of them being the pump-probe ones. In such experiments a short and intense laser pulse (the pump) is used to drive a system out of equilibrium and a second one (the probe) is sent on the same sample after a delay Δt in order to measure which are the characteristics of the transient state reached by the system. The typical time scale of the electron-electron interaction is of the order of tens to hundreds of femtoseconds while that of the electron-lattice interaction is typically of the order of picoseconds [22]. Thus, pump-probe experiments enable one to investigate the effects on the dynamics of the electron-electron interaction, even before the coupling to the lattice starts to be relevant for the relaxation. With such experiments it is possible to see the action, at different time-scales, of the intertwined degrees of freedom which characterize a system and its equilibrium properties, beyond the conventional adiabatic point of view. In the same way, pump-probe experiments also give access to novel meta-stable phases which are usually not accessible from the thermal pathway.

These type of experiments have been broadly used to study many correlated materials such as, for example, the vanadium dioxide [142, 163, 117, 141, 164]. For this compound in particular a transition from the monoclinic M1 insulator to a monoclinic metallic phase was observed at the ultrafast time scale, opening the intriguing possibility for the realization of a switch able to operate in the femtosecond domain.

Another phenomenon that comes from the non equilibrium world is related to the possibility of light-induce a transient superconducting phase in the alkali doped fulleride K_3C_{60} above its critical temperature $T_c \sim 20$ K [165]. A clean experimental confirmation of the superconducting nature of the photo-induced phase is still lacking (i.e. a measurement of the Meissner effect), anyway the present experimental result can be rationalized in some theoretical frameworks [166–168]. This state is observed even at room temperature, and it

would give rise to potentially interesting applications.
Despite the large progresses that have been made in this field from the experimental side, from the theory one there are many obscure points that still have to be enlighten. Particularly, the theoretical methods implemented so far are trying to provide a microscopic description of the observed dynamics of correlated materials driven out of equilibrium. A promising methodology is provided by the non equilibrium non-crossing approximation (NE-NCA) applied to DMFT [169]. In this chapter we will first derive the equations to implement equilibrium NCA [170–173] and one crossing approximation (OCA) [174] as a solver for the AIM. Those approximations work well in the limit of small hybridizations and of temperatures larger than the Kondo one. In the last part of the chapter we develop the equations for NE-NCA. Motivated by the previously mentioned experimental achievements we develop a formalism that can be applied in both the cases with and without superconducting symmetry breaking.

6.1 The model

We want to study the multi-orbital attractive Hubbard model, equal to the usual one but with the sign of the interaction changed ($U < 0$), leading to an attractive electron-electron interaction. This model can support superconductive and Bose-Einstein condensate (BEC) solutions [175]. In the spirit of the DMFT analysis, we can write an Anderson-like impurity model that reproduces the same effective action that we obtain for a single site of the original lattice model, see Sec. 3.3. The model that we obtain is the AIM with superconducting bath, explicitly written as [176]:

$$
\begin{aligned}
H &= H_{imp} + H_{bath} + H_{hyb} \ , \\
H_{imp} &= \sum_{a,b} \sum_{\sigma} E_{a,b,\sigma} d^\dagger_{a,\sigma} d_{b,\sigma} + H_{int} \ , \\
H_{bath} &= \sum_{p,\sigma} \varepsilon_{p,\sigma} c^\dagger_{p,\sigma} c_{p,\sigma} - \sum_{p} \left[\Delta c^\dagger_{p,\uparrow} c^\dagger_{-p,\downarrow} + \Delta^* c_{-p,\downarrow} c_{p,\uparrow} \right] \ , \\
H_{hyb} &= \sum_{p,a} \sum_{\sigma} \left[V^a_{p,\sigma} c^\dagger_{p,\sigma} d_{a,\sigma} + V^{a*}_{p,\sigma} d^\dagger_{a,\sigma} c_{p,\sigma} \right] \ ,
\end{aligned}
\tag{6.1}
$$

where a, b are the orbital indexes, σ is the spin, p the bath index. $d_{a,\sigma}$ ($d^\dagger_{a,\sigma}$) is the operator that annihilates (creates) an electron on the level a with spin σ of the impurity, instead $c_{p,\sigma}$ ($c^\dagger_{p,\sigma}$) is the operator that annihilates (creates) an electron on the level p ($= 1, 2, \cdots, N_s$) with spin σ of the bath. $E_{a,b,\sigma}$ is the hopping amplitude of an electron with spin σ from the level b to the level a of the impurity, and H_{int} is the interaction, a local term that involves

just the impurity operators. $\varepsilon_{p,\sigma}$ is the energy of an electron on the level p and spin σ in the bath and Δ is the amplitude of the superconducting coupling of the bath electrons. We assume a complex s-wave kind of superconductivity $\Delta = |\Delta| e^{-2i\phi}$. $V^{a}_{p,\sigma}$ is the amplitude of the coupling of the bath level p with the impurity level a for spin σ. In the following we assume that the bath energy levels are independent by the spin, so $\varepsilon_{p,\sigma} = \varepsilon_p$.
Since we are dealing with superconductivity, it is convenient to define the Nambu spinor of the bath:

$$\psi_p = \begin{pmatrix} c_{p,\uparrow} \\ c^{\dagger}_{-p,\downarrow} \end{pmatrix} , \tag{6.2}$$

and to write the expression of the modulus of the eigenvalues of the bath Hamiltonian H_{bath}, $E_p = \sqrt{\varepsilon_p^2 + |\Delta|^2}$. We can define the imaginary time hybridization matrix in the Nambu index as:

$$\bar{\Delta}_{ab}(\tau) = -\frac{1}{N_s} \sum_p \begin{pmatrix} V^{a*}_{p,\uparrow} & 0 \\ 0 & V^{a}_{-p,\downarrow} \end{pmatrix} \langle T_\tau \psi_p(\tau) \otimes \psi^{\dagger}_p(0) \rangle \begin{pmatrix} V^{b}_{p,\uparrow} & 0 \\ 0 & V^{b*}_{-p,\downarrow} \end{pmatrix} . \tag{6.3}$$

T_τ is the time ordering operator and $\otimes$ the direct product, that has to be interpreted as

$$\psi_p(\tau) \otimes \psi^{\dagger}_p(0) = \begin{pmatrix} c_{p,\uparrow}(\tau) c^{\dagger}_{p,\uparrow}(0) & c_{p,\uparrow}(\tau) c_{-p,\downarrow}(0) \\ c^{\dagger}_{-p,\downarrow}(\tau) c^{\dagger}_{p,\uparrow}(0) & c^{\dagger}_{-p,\downarrow}(\tau) c_{-p,\downarrow}(0) \end{pmatrix} . \tag{6.4}$$

We can explicitly compute the hybridization function of the bath

$$\begin{aligned}
\left(\bar{\Delta}_{ab}(\tau)\right)_{11} &= \frac{1}{N_s} \sum_p \frac{V^{a*}_{p,\uparrow} V^{b}_{p,\uparrow}}{1+e^{\beta E_p}} \begin{cases} -\cos^2(\theta_p)\, e^{(\beta-\tau)E_p} - \sin^2(\theta_p)\, e^{\tau E_p}, \ \tau \in (0,\beta) \\ \cos^2(\theta_p)\, e^{-\tau E_p} + \sin^2(\theta_p)\, e^{(\tau+\beta)E_p}, \ \tau \in (-\beta,0) \end{cases} , \\
\left(\bar{\Delta}_{ab}(\tau)\right)_{12} &= \frac{2e^{2i\phi}}{N_s} \sum_p \frac{V^{a*}_{p,\uparrow} V^{b*}_{-p,\downarrow}}{1+e^{\beta E_p}} e^{\frac{\beta}{2} E_p} \begin{cases} -\sinh\left(\left(\tau - \frac{\beta}{2}\right) E_p\right), \ \tau \in (0,\beta) \\ \sinh\left(\left(\tau + \frac{\beta}{2}\right) E_p\right), \ \tau \in (-\beta,0) \end{cases} , \\
\left(\bar{\Delta}_{ab}(\tau)\right)_{21} &= \left(\bar{\Delta}_{ab}(\tau)\right)^{*}_{12} , \\
\left(\bar{\Delta}_{ab}(\tau)\right)_{22} &= \frac{1}{N_s} \sum_p \frac{V^{a}_{-p,\downarrow} V^{b*}_{-p,\downarrow}}{1+e^{\beta E_p}} \begin{cases} -\sin^2(\theta_p)\, e^{(\beta-\tau)E_p} - \cos^2(\theta_p)\, e^{\tau E_p}, \ \tau \in (0,\beta) \\ \sin^2(\theta_p)\, e^{-\tau E_p} + \cos^2(\theta_p)\, e^{(\tau+\beta)E_p}, \ \tau \in (-\beta,0) \end{cases} ,
\end{aligned} \tag{6.5}$$

where the third relation is true if we can map $\left(V^{a*}_{p,\uparrow}, V^{b*}_{-p,\downarrow}\right)$ in $\left(V^{a}_{-p,\downarrow}, V^{b}_{p,\uparrow}\right)$, and we assume that this is the case. The angle θ_p is defined as:

$$\sin^2(\theta_p) = \frac{1}{2}\left[1 - \frac{\varepsilon_p}{E_p}\right] . \tag{6.6}$$

6.2 Aim of the calculation

We want to develop a DMFT solver, so, as we saw in Sec. 3.2 an important step in this direction consist in the computation of the single-particle impurity Green's function of the problem. In real time this is defined as:

$$G_{a,b}(t_2 - t_1) = -i\langle T_t\, \Psi_a(t_2) \otimes \Psi^\dagger_b(t_1)\rangle \tag{6.7}$$

where the spinor $\Psi_a(t)$ is equal to:

$$\Psi_a(t) = \begin{pmatrix} 1 & 0 \\ 0 & -1 \end{pmatrix} \begin{pmatrix} d_{a,\uparrow}(t) \\ d^\dagger_{a,\downarrow}(t) \end{pmatrix} = \begin{pmatrix} d_{a,\uparrow}(t) \\ -d^\dagger_{a,\downarrow}(t) \end{pmatrix}$$

The spinorial operators that appear in Eq. (6.7) are written in the Heisenberg representation, so they evolve through the time translation operator that involves the full Hamiltonian of the problem:

$$\Psi_a(t) = e^{iHt}\Psi_a(0)\, e^{-iHt} \tag{6.8}$$

We define $H_0 = H_{imp} + H_{bath}$ and $H_1 = H_{hyb}$, so the total Hamiltonian H is equal to the sum of an unperturbed part H_0 and of a perturbation H_1. We have to bear in mind that, since the part of the Hamiltonian H_{imp} that belongs to the unperturbed H_0 is non-quadratic, Wick's theorem does not apply for the impurity operators. This may lead to some complications if we have to compute the average of a product of operators [177].

In order to write the propagator of the system in a suitable form to apply perturbation theory in the hybridization coupling, we have to review some basic notions related to the pictures in quantum mechanics. The time evolution of an operator in the Heisenberg and in the interaction representations is given, respectively, by:

$$\begin{aligned} A_H(t) &= e^{iHt} A_S e^{-iHt} \,, \\ A_I(t) &= e^{iH_0 t} A_S e^{-iH_0 t} \,, \end{aligned} \tag{6.9}$$

instead the time evolution of a state in the Schroedinger and interaction pictures is written, respectively, as:

$$\begin{aligned} |\phi_S(t)\rangle &= e^{-iH(t-t_0)}|\phi_S(t_0)\rangle = U_S(t,t_0)|\phi_S(t_0)\rangle \ , \\ |\phi_I(t)\rangle &= e^{iH_0t}U_S(t,t_0)e^{-iH_0t_0}|\phi_I(t_0)\rangle = U_I(t,t_0)|\phi_I(t_0)\rangle \ . \end{aligned} \tag{6.10}$$

From the definition of $U_I(t,t_0)$ and by considering its time derivative, it immediately follows

$$i\partial_t U_I(t,t_0) = H_{1,I}(t)\,U_I(t,t_0) \ . \tag{6.11}$$

The differential equation Eq. (6.11) can be iteratively solved, arriving at the solution

$$U_I(t,t_0) = T_t\left[e^{-i\int_{t_0}^{t}dt' H_{1,I}(t')}\right] \ . \tag{6.12}$$

The generic operator written in Heisenberg picture respect the following identity

$$\begin{aligned} A_H(t) &= e^{iHt}\left(e^{-iH_0t}A_I(t)\,e^{iH_0t}\right)e^{-iHt} = U_I(0,t)A_I(t)\,U_I(t,0) \\ &= U_I(0,t)\,e^{iH_0t}A_Se^{-iH_0t}U_I(t,0) \ . \end{aligned} \tag{6.13}$$

so that, by comparing Eq. (6.9) with Eq. (6.13), we get the equivalence $e^{-iHt} = e^{-iH_0t}U_I(t,0)$. This means that Eq. (6.8) can be rephrased as

$$\begin{aligned} \Psi_a(t) &= U_I(0,t)\,e^{iH_0t}\Psi_a(0)\,e^{-iH_0t}U_I(t,0) \\ &= U_I(0,t)\,e^{iH_{imp}t}\Psi_a(0)\,e^{-iH_{imp}t}U_I(t,0) \ , \end{aligned} \tag{6.14}$$

where the last equivalence follows from the commutation among the impurity and bath operators. We can define the un-hybridized impurity and bath propagators, respectively, as:

$$\begin{aligned} R_0(t,0) &= e^{-iH_{imp}t} \ , \\ R_0^B(t,0) &= e^{-iH_{bath}t} \ , \end{aligned} \tag{6.15}$$

so that the total un-hybridized propagator is simply given by the product of the two expressions in Eq. (6.15):

$$\widetilde{R}_0(t,0) = R_0(t,0)\,R_0^B(t,0) = e^{-i\left(H_{imp}+H_{bath}\right)t} \ . \tag{6.16}$$

The previous definitions allow us to write the full propagator of the impurity as

$$R(t,0) = e^{-iH_{imp}t}U_I(t,0) = R_0(t,0)\,T_t\left[e^{-i\int_0^t dt'\widetilde{R}_0(0,t')H_{hyb}\widetilde{R}_0(t',0)}\right] \ , \tag{6.17}$$

in which we have to trace out the bath operators. Eq. (6.8) straightforwardly becomes:

$$\Psi_a(t) = R(0,t)\,\Psi_a(0)\,R(t,0)\ .$$

The computation of the full impurity propagator $R(t,t_0)$ is crucial to get the impurity Green's function Eq. (6.7). In the next section we give a scheme to obtain this quantity in the NCA.

6.3 Derivation of the NCA equations at equilibrium

In Sec. 6.2 we defined the propagators for the system in real time, anyway, in order to perform perturbation theory it is more convenient to work in imaginary time τ, so that we do not have to deal with the signs coming from the presence of the imaginary units. We work under equilibrium conditions, so the propagators depend just by the time difference between the final and the initial time of the propagation. The full expression of the evolution operator for the impurity is then:

$$R(\tau) = R_0(\tau)\,T_\tau\left[e^{-\int_0^\tau d\tau' \widetilde{R}_0(-\tau')H_{hyb}\widetilde{R}_0(\tau')}\right] \tag{6.18}$$

If the bath and the impurity are un-hybridized, meaning that the Hamiltonian H_{hyb} goes to zero, the dressed impurity propagator becomes equal to the bare one, as expected. Since we do not know how to compute exactly the time ordered term that appears in Eq. (6.18), we can rewrite its expression by a Taylor expansion

$$\begin{aligned} T_\tau\left[e^{-\int_0^\tau d\tau' \widetilde{R}_0(-\tau')H_{hyb}\widetilde{R}_0(\tau')}\right] &= \hat{1} - \int_0^\tau d\tau' \widetilde{R}_0(-\tau')H_{hyb}\widetilde{R}_0(\tau') + \\ + \int_0^\tau d\tau' \int_0^{\tau'} d\tau'' \widetilde{R}_0(-\tau')H_{hyb}\widetilde{R}_0(\tau')\,\widetilde{R}_0(-\tau'')H_{hyb}\widetilde{R}_0(\tau'') &+ \cdots \end{aligned} \tag{6.19}$$

All the odd powers in Eq. (6.19) do not preserve the parity of the number of particles in the bath, so when we trace out the operators of the bath they go to zero. Since the unperturbed Hamiltonian H_0 is quadratic in the bath operators, Wick's theorem can be applied. The first non-trivial term different from zero is the second order one. If we stop the expansion at that stage Eq. (6.18) becomes:

$$\hat{R}(\tau) = \hat{R}_0(\tau) + \int_0^\tau d\tau' \int_0^{\tau'} d\tau'' \hat{R}_0(\tau-\tau')\,\hat{S}^{(1)}(\tau'-\tau'')\,\hat{R}_0(\tau'') \tag{6.20}$$

with:

$$\hat{S}^{(1)}(\tau) = \sum_{a,b}\left[\hat{\Psi}^{t}_{a}\left(1_{2\times 2}\otimes\hat{R}_{0}(\tau)\right)\bar{\Delta}^{t}_{ba}(-\tau)\left(\hat{\Psi}^{\dagger}_{b}\right)^{t} - \hat{\Psi}^{\dagger}_{a}\left(1_{2\times 2}\otimes\hat{R}_{0}(\tau)\right)\bar{\Delta}_{ab}(\tau)\hat{\Psi}_{b}\right] \tag{6.21}$$

The notation with the hat means that now we are dealing with matrices written in the local Hilbert space of the impurity. The matrix $1_{2\times 2}$ is the identity in the Nambu space, and the product $1_{2\times 2}\otimes\hat{R}_{0}(\tau)$ means that the matrix $\hat{R}_{0}(\tau)$ acts on both the components of the Nambu vectors. Of course the dimension of the local Hilbert space dramatically depends by the number of orbitals of the considered problem.

Eq. (6.20) and Eq. (6.21) have the drawback that they do not constitute a self-consistent approximation. We can cure this problem by substituting the bare propagators in Eq. (6.20) and Eq. (6.21) with the dressed ones. In this way we get the NCA equations:

$$\hat{R}(\tau) = \hat{R}_{0}(\tau) + \int_{0}^{\tau} d\tau' \int_{0}^{\tau'} d\tau'' \hat{R}(\tau-\tau')\,\hat{S}_{NCA}(\tau'-\tau'')\,\hat{R}_{0}(\tau'') \ , \tag{6.22}$$

with

$$\hat{S}_{NCA}(\tau) = \sum_{a,b}\left[\hat{\Psi}^{t}_{a}\left(1_{2\times 2}\otimes\hat{R}(\tau)\right)\bar{\Delta}^{t}_{ba}(-\tau)\left(\hat{\Psi}^{\dagger}_{b}\right)^{t} - \hat{\Psi}^{\dagger}_{a}\left(1_{2\times 2}\otimes\hat{R}(\tau)\right)\bar{\Delta}_{ab}(\tau)\hat{\Psi}_{b}\right] . \tag{6.23}$$

By considering the diagrammatic representation of this equation, the name of the approximation scheme becomes apparent: just the diagrams without any crossing of the bath lines appear in the expansion. The role played by $\hat{S}_{NCA}(\tau)$ is the same played by the self energy in the usual Dyson equation for the Green's function, so we call it in the same way. Once we have solved self-consistently Eq. (6.22) we become able to compute the impurity Green's function in the NCA.

If the superconducting coupling is settled equal to zero, so that the hybridization function in Eq. (6.5) is purely diagonal, we recover the same equations obtained for the AIM without superconducting terms in the bath [178].

6.3.1 Useful quantities in NCA

In order to stress the importance of the quantity $\hat{R}(\tau)$, we explicitly show how it is related to some observables and to other useful functions. We start by illustrating the form of the imaginary time impurity Green's function $G_{ab}(\tau_2 - \tau_1)$ in the NCA scheme:

$$\begin{aligned}
&G_{ab}(\tau_2-\tau_1) = -\langle T_\tau \Psi_a(\tau_2)\otimes\Psi_b^\dagger(\tau_1)\rangle = \\
&= -\theta(\tau_2-\tau_1)\langle\Psi_a(\tau_2)\otimes\Psi_b^\dagger(\tau_1)\rangle + \theta(\tau_1-\tau_2)\langle\Psi_b^\dagger(\tau_1)\otimes\Psi_a(\tau_2)\rangle = \\
&= -\theta(\tau_2-\tau_1)\frac{1}{Z}\mathrm{Tr}\left[\hat{R}(\beta+\tau_1-\tau_2)\hat{\Psi}_a\hat{R}(\tau_2-\tau_1)\otimes\hat{\Psi}_b^\dagger\right] + \\
&+ \theta(\tau_1-\tau_2)\frac{1}{Z}\mathrm{Tr}\left[\hat{R}(\beta+\tau_2-\tau_1)\hat{\Psi}_b^\dagger\hat{R}(\tau_1-\tau_2)\otimes\hat{\Psi}_a\right] ,
\end{aligned}$$

where we omitted, for simplicity, the direct product of the $\hat{R}$ matrix with the identity in the Nambu space. The trace appearing therein has to be considered just on the local Hilbert space and not on the Nambu one. The partition function Z is:

$$Z = \mathrm{Tr}\left[\hat{R}(\beta)\right] .$$

and the statistical average of a generic local operator A can still be written in terms of $\hat{R}(\beta)$:

$$\langle A\rangle = \frac{1}{Z}\mathrm{Tr}\left[\hat{R}(\beta)\hat{A}\right] .$$

6.4 Derivation of the OCA equations

We can now go a step further in the hybridization expansion, by considering the next different from zero order in Eq. (6.19). By retaining just the terms that correspond to Feynman diagrams in which the hybridization lines cross one time, we arrive to write the expression of the self-energy in the OCA. We follow the same procedure depicted in Sec. 6.3, and the self-energy that we obtain is:

$$\begin{aligned}
&\hat{S}_{OCA}(\tau) = -\sum_{a,b}\sum_{c,d}\sum_{l,m}\sum_{h,k}\int_0^{\tau} d\tau_2 \int_0^{\tau_2} d\tau_1 \\
&[\left(\hat{\Psi}^t_a\right)_l \hat{R}(\tau-\tau_2)\left(\hat{\Psi}_b\right)_m \hat{R}(\tau_2-\tau_1)\left(\hat{\Psi}^{\dagger}_c\right)_h \hat{R}(\tau_1)\left(\hat{\Psi}^{\dagger t}_d\right)_k \\
&\left(\bar{\Delta}_{ca}(\beta+\tau_1-\tau)\right)_{l,h}\left(\bar{\Delta}_{db}(\beta-\tau_2)\right)_{m,k} + \\
&+\left(\hat{\Psi}^t_a\right)_l \hat{R}(\tau-\tau_2)\left(\hat{\Psi}^{\dagger t}_b\right)_m \hat{R}(\tau_2-\tau_1)\left(\hat{\Psi}^{\dagger}_c\right)_h \hat{R}(\tau_1)\left(\hat{\Psi}_d\right)_k \\
&\left(\bar{\Delta}_{ca}(\beta+\tau_1-\tau)\right)_{l,h}\left(\bar{\Delta}_{bd}(\tau_2)\right)_{m,k} + \\
&+\left(\hat{\Psi}^{\dagger}_a\right)_l \hat{R}(\tau-\tau_2)\left(\hat{\Psi}^{\dagger t}_b\right)_m \hat{R}(\tau_2-\tau_1)\left(\hat{\Psi}^t_c\right)_h \hat{R}(\tau_1)\left(\hat{\Psi}_d\right)_k \\
&\left(\bar{\Delta}_{ac}(\tau-\tau_1)\right)_{l,h}\left(\bar{\Delta}_{bd}(\tau_2)\right)_{m,k} + \\
&+\left(\hat{\Psi}^{\dagger}_a\right)_l \hat{R}(\tau-\tau_2)\left(\hat{\Psi}_b\right)_m \hat{R}(\tau_2-\tau_1)\left(\hat{\Psi}^t_c\right)_h \hat{R}(\tau_1)\left(\hat{\Psi}^{\dagger t}_d\right)_k \\
&\left(\bar{\Delta}_{ac}(\tau-\tau_1)\right)_{l,h}\left(\bar{\Delta}_{db}(\beta-\tau_2)\right)_{m,k}] \, ,
\end{aligned} \tag{6.24}$$

where $l,m,h,k = 1,2$ are Nambu indexes. The total self-energy of the problem is given by the sum of the NCA and the OCA terms in Eq. (6.23) and Eq. (6.24), so we write:

$$\hat{S}_{tot}(\tau) = \hat{S}_{NCA}(\tau) + \hat{S}_{OCA}(\tau) \ . \tag{6.25}$$

The Dyson equation remains substantially unchanged with respect to the one that we wrote in Eq. (6.22), the only difference being that the self-energy is the one in Eq. (6.25):

$$\hat{R}(\tau) = \hat{R}_0(\tau) + \int_0^{\tau} d\tau' \int_0^{\tau'} d\tau'' \hat{R}(\tau-\tau')\,\hat{S}_{tot}(\tau'-\tau'')\,\hat{R}_0(\tau'') \ . \tag{6.26}$$

The self-energy in the OCA Eq. (6.24) is much more involved with respect to the one in the NCA, especially for the presence of the double time integral. Luckily we can simplify its computation by defining some *ad hoc* functions so that, at the end, we can reduce the double integral as two single-variable integrals. We define:

$$\begin{aligned}
\left(\hat{f}_1\right)^{ad}_{l,k}(\tau,\tau_2) &= \sum_{b,m} \left(\hat{\Psi}^{t}_{a}\right)_l \hat{R}(\tau-\tau_2) \left(\hat{\Psi}_{b}\right)_m \left(\bar{\Delta}_{db}(\beta-\tau_2)\right)_{m,k} , \\
\left(\hat{f}_2\right)^{ad}_{l,k}(\tau,\tau_2) &= \sum_{b,m} \left(\hat{\Psi}^{t}_{a}\right)_l \hat{R}(\tau-\tau_2) \left(\hat{\Psi}^{\dagger t}_{b}\right)_m \left(\bar{\Delta}_{bd}(\tau_2)\right)_{m,k} , \\
\left(\hat{f}_3\right)^{ad}_{l,k}(\tau,\tau_2) &= \sum_{b,m} \left(\hat{\Psi}^{\dagger}_{a}\right)_l \hat{R}(\tau-\tau_2) \left(\hat{\Psi}^{\dagger t}_{b}\right)_m \left(\bar{\Delta}_{bd}(\tau_2)\right)_{m,k} , \\
\left(\hat{f}_4\right)^{ad}_{l,k}(\tau,\tau_2) &= \sum_{b,m} \left(\hat{\Psi}^{\dagger}_{a}\right)_l \hat{R}(\tau-\tau_2) \left(\hat{\Psi}_{b}\right)_m \left(\bar{\Delta}_{db}(\beta-\tau_2)\right)_{m,k} ,
\end{aligned} \tag{6.27}$$

and:

$$\begin{aligned}
(\hat{g}_1)^{da}_{k,l}(\tau,\tau_2) &= \sum_{c,h} \int_0^{\tau_2} d\tau_1 \hat{R}(\tau_2-\tau_1) \left(\hat{\Psi}^{\dagger}_{c}\right)_h \hat{R}(\tau_1) \left(\hat{\Psi}^{\dagger t}_{d}\right)_k \left(\bar{\Delta}_{ca}(\beta+\tau_1-\tau)\right)_{l,h} , \\
(\hat{g}_2)^{da}_{k,l}(\tau,\tau_2) &= \sum_{c,h} \int_0^{\tau_2} d\tau_1 \hat{R}(\tau_2-\tau_1) \left(\hat{\Psi}^{\dagger}_{c}\right)_h \hat{R}(\tau_1) \left(\hat{\Psi}_{d}\right)_k \left(\bar{\Delta}_{ca}(\beta+\tau_1-\tau)\right)_{l,h} , \\
(\hat{g}_3)^{da}_{k,l}(\tau,\tau_2) &= \sum_{c,h} \int_0^{\tau_2} d\tau_1 \hat{R}(\tau_2-\tau_1) \left(\hat{\Psi}^{t}_{c}\right)_h \hat{R}(\tau_1) \left(\hat{\Psi}_{d}\right)_k \left(\bar{\Delta}_{ac}(\tau-\tau_1)\right)_{l,h} , \\
(\hat{g}_4)^{da}_{k,l}(\tau,\tau_2) &= \sum_{c,h} \int_0^{\tau_2} d\tau_1 \hat{R}(\tau_2-\tau_1) \left(\hat{\Psi}^{t}_{c}\right)_h \hat{R}(\tau_1) \left(\hat{\Psi}^{\dagger t}_{d}\right)_k \left(\bar{\Delta}_{ac}(\tau-\tau_1)\right)_{l,h} .
\end{aligned}$$

At the end, the OCA part of the self-energy Eq. (6.24) can be written

$$\hat{S}_{OCA}(\tau) = -\sum_{a,d}\sum_{l,k}\sum_{\eta=1}^{4} \int_0^{\tau} d\tau_2 \left(\hat{f}_\eta\right)^{ad}_{l,k}(\tau,\tau_2) \left(\hat{g}_\eta\right)^{da}_{k,l}(\tau,\tau_2) .$$

In this last form it is easier to computationally perform the self consistent cycle to solve the Dyson equation Eq. (6.26). We just mention that the way in which useful quantities can be computed in the OCA is reported in [178].

6.5 Derivation of the NCA equations for the non equilibrium case

We want now to consider an out of equilibrium problem. In this respect, we have to slightly modify the definition of the impurity propagator with respect to the one that we gave in the previous sections [179, 169, 180]. We are interested in studying the transient dynamics of the system and not just the asymptotic state reached at infinite times. Due to this reason

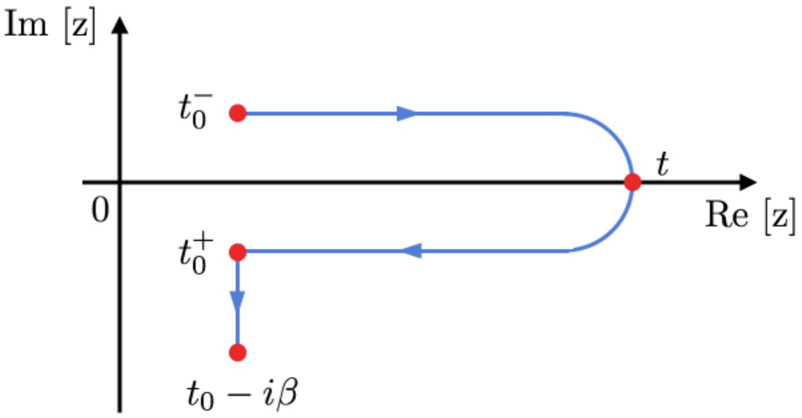

Figure 6.1: Kostantinov-Perel contour C in the complex plane. We notice that this is an oriented contour in which the upper branch goes in the forward direction, instead the lower one goes in the backward one.

we have to consider a time evolution of the operators on the Kostantinov-Perel contour (the Keldysh contour from t_0 to t plus a peace along the imaginary axis from t_0 to $t_0 - i\beta$) shown in Fig. 6.1. Since we are out of equilibrium, the propagator depends by the two times among which we are evolving the system.

By using a notation similar to the one we introduced before, the bare impurity propagator gets the form:

$$R_0\left(z, z'\right) = -iT_C\left[e^{-i\int_C dz_1 H_{imp}(z_1)}\right] , \tag{6.28}$$

where z, z' are complex variables that live on the Kostantinov-Perel contour C and T_C is the time ordering operator on C. The integral that appears at the exponent of the exponential has to be performed along the contour. With respect to the equilibrium case, we have defined the propagator with an imaginary unit that was not included before. Due to this reason we have to be careful when we compute the composition of two propagators. The initial condition will be changed as:

$$R_0\left(z, z^-\right) = -i1 , \tag{6.29}$$

where z^- is infinitesimally before z and 1 is the identity operator.
In a similar way we can define the bath and the total bare propagators as:

$$\begin{aligned} R_0^B\left(z, z'\right) &= iT_C\left[e^{-i\int_C dz_1 H_{bath}(z_1)}\right] , \\ \widetilde{R}_0\left(z, z'\right) &= R_0\left(z, z'\right) R_0^B\left(z, z'\right) , \end{aligned} \tag{6.30}$$

with initial conditions:

$$\begin{aligned} R_0^B\left(z,z^-\right) &= i1 \ , \\ \widetilde{R}_0\left(z,z^-\right) &= 1 \ . \end{aligned} \tag{6.31}$$

The fully dressed impurity propagator has the same formal expression as Eq. (6.18), but the time ordering and the integration at the exponent of the exponential have to be considered on the contour. Moreover the propagators depend explicitly by the initial and final times. The procedure that we implement in order to get the NCA equations for the non equilibrium case is the same as in equilibrium, and as a matter of fact the result that we get has the same formal structure:

$$\hat{R}\left(z,z'\right) = \hat{R}_0\left(z,z'\right) + \int_C dz_1 \int_C dz_2\, \hat{R}_0\left(z,z_1\right) \hat{S}_{NCA}\left(z_1,z_2\right) \hat{R}\left(z_2,z'\right) \ , \tag{6.32}$$

where the self-energy is:

$$\begin{aligned} \hat{S}_{NCA}\left(z_1,z_2\right) = i\sum_{a,b} [&\hat{\Psi}_a^t \left(1_{2\times2} \otimes \hat{R}\left(z_1,z_2\right)\right) \bar{\Delta}_{b,a}^t\left(z_2,z_1\right) \left(\hat{\Psi}_b^\dagger\right)^t \\ &- \hat{\Psi}_a^\dagger \left(1_{2\times2} \otimes \hat{R}\left(z_1,z_2\right)\right) \bar{\Delta}_{a,b}\left(z_1,z_2\right) \hat{\Psi}_b] \ . \end{aligned} \tag{6.33}$$

The contour integrals in Eq. (6.32) have to be interpreted in the following way:

$$\int_C dz_1 \longrightarrow \begin{cases} \int_{z'}^{z} dz_1 \ , \ z > z' \\ \int_{t_0}^{z} dz_1 + \int_{t_0}^{t_0 - i\beta} dz_1 + \int_{z'}^{t_0} dz_1 \ , \ z < z' \end{cases} \ . \tag{6.34}$$

Again, Eq. (6.32) can be solved self-consistently, but in this case the un-known matrix of functions $\hat{R}\left(z_1,z_2\right)$ depends by two variables, making the problem much more difficult to be solved with respect to the equilibrium one. For this reason we want to find another way to solve it. The bare impurity propagator $R_0\left(z,z'\right)$ satisfies the equation of motion:

$$\left[i\partial_z - H_{imp}\left(z\right)\right] R_0\left(z,z'\right) = \delta_C\left(z,z'\right) \ , \tag{6.35}$$

where $\delta_C\left(z,z'\right)$ is the Dirac's delta on the contour. By applying $\left[i\partial_z - \hat{H}_{imp}\left(z\right)\right]$ to Eq. (6.32) we get an integro-differential equation

$$i\partial_z \hat{R}\left(z,z'\right) = \hat{H}_{imp}\left(z\right) \hat{R}\left(z,z'\right) + \int_C dz_1 \hat{S}_{NCA}\left(z,z_1\right) \hat{R}\left(z_1,z'\right) + \delta_C\left(z,z'\right) \ . \tag{6.36}$$

If in Eq. (6.36) we exclude the case $z = z'$, the Dirac's delta can be canceled out. This equation is less computationally expansive to be solved than Eq. (6.32); indeed, once that we have an initial condition for the propagator, we have a recipe to evolve it in time. In order to explicitly solve this problem, we have to project it on its Keldysh components. This is done in App. B.

6.5.1 Useful quantities in non-equilibrium NCA

In this section we follow [181]. If we set $t_0 = 0$ we can write the partition function of the system:

$$Z = \mathrm{Tr}\left[i\hat{R}\left(-i\beta, 0^+\right)\right] .$$

The occupation for spin σ on the impurity level a is given by:

$$\begin{aligned} n_{a,\sigma}(z) = \langle d^\dagger_{a,\sigma}(z)\, d_{a,\sigma}\left(z^-\right)\rangle &= \frac{1}{Z}\mathrm{Tr}\left[\hat{R}(0,z)\,\hat{d}^\dagger_{a,\sigma}\hat{R}(z,0)\,\hat{R}\left(0,z^-\right)\hat{d}_{a,\sigma}\hat{R}\left(z^-,0\right)\right] = \\ &= -\frac{1}{Z}\mathrm{Tr}\left[\hat{R}\left(z^-,0\right)\hat{R}(0,z)\,\hat{d}^\dagger_{a,\sigma}\hat{d}_{a,\sigma}\right] = \frac{i}{Z}\mathrm{Tr}\left[\hat{R}\left(z^-,z\right)\hat{d}^\dagger_{a,\sigma}\hat{d}_{a,\sigma}\right] \end{aligned}$$

For the double occupancies of the level a of the impurity we have:

$$D_a(z) = \langle d^\dagger_{a,\uparrow}(z)\, d_{a,\uparrow}\left(z^-\right) d^\dagger_{a,\downarrow}\left(z^{--}\right) d_{a,\downarrow}\left(z^{---}\right)\rangle = \frac{i}{Z}\mathrm{Tr}\left[\hat{R}\left(z^-,z\right)\hat{d}^\dagger_{a,\uparrow}\hat{d}_{a,\uparrow}\hat{d}^\dagger_{a,\downarrow}\hat{d}_{a,\downarrow}\right]$$

We can even write the normal part of the impurity Green's function, given by:

$$\begin{aligned} G_{a,b,\sigma}\left(z,z'\right) &= -i\langle T_C d_{a,\sigma}(z)\, d^\dagger_{b,\sigma}\left(z'\right)\rangle = \\ &= -i\left[\theta_C\left(z,z'\right)\langle d_{a,\sigma}(z)\, d^\dagger_{b,\sigma}\left(z'\right)\rangle - \theta_C\left(z',z\right)\langle d^\dagger_{b,\sigma}\left(z'\right) d_{a,\sigma}(z)\rangle\right] = \\ &= \frac{i}{Z}\left(\theta_C\left(z,z'\right) - \theta_C\left(z',z\right)\right)\mathrm{Tr}\left[\hat{R}\left(z',z\right)\hat{d}_{a,\sigma}\hat{R}\left(z,z'\right)\hat{d}^\dagger_{b,\sigma}\right] \end{aligned}$$

The anomalous Green's function is instead:

$$\begin{aligned} F_{a,b,\sigma}\left(z,z'\right) &= -i\langle T_C d^\dagger_{a,\uparrow}(z)\, d^\dagger_{b,\downarrow}\left(z'\right)\rangle = \\ &= \frac{i}{Z}\left(\theta_C\left(z,z'\right) - \theta_C\left(z',z\right)\right)\mathrm{Tr}\left[\hat{R}\left(z',z\right)\hat{d}^\dagger_{a,\uparrow}\hat{R}\left(z,z'\right)\hat{d}^\dagger_{b,\downarrow}\right] \end{aligned}$$

To conclude we write also the superconducting order parameter:

$$\delta_{a,b}(z) = \langle d^\dagger_{a,\uparrow}(z)\, d^\dagger_{b,\downarrow}\left(z^-\right)\rangle = \frac{i}{Z}\mathrm{Tr}\left[\hat{R}\left(z^-,z\right)\hat{d}^\dagger_{a,\uparrow}\hat{d}^\dagger_{b,\downarrow}\right]$$

6.6 Conclusions

In this chapter we obtained a complete set of equations that permit to solve the impurity problem with superconducting bath under equilibrium conditions in the framework of the non crossing and of the one-crossing approximations. Moreover, we obtained the equations for solving the same problem out of equilibrium in the NCA. The derivation that we implemented is clean and permit to reproduce, in the non-superconducting case, the equations already in the literature. Once implemented they open the possibility for the study of a broad number of systems, ranging from the metal-insulator transition induced by out of equilibrium sources to the Bose-Einstein condensate induced by external perturbations. We will comment a bit more about those possible realizations in Chap. 7 devoted to the general conclusions and perspectives for future works.

Chapter 7

Conclusions and perspectives

In this thesis, we analyzed the simplest generalizations of the single band Hubbard model at half filling, so systems with two bands interacting through a local Hubbard repulsion at quarter filling. More specifically, we analyzed the effect of the breaking of the orbital degeneracy in two cases: one with two bands with the same shape but different bandwidth, the second with same bandwidth but different shape coupled to a lattice deformation. We believe that the second of those provides a good description of the qualitative physics of vanadium dioxide.

The method that we used in order to study those problems is DMFT with exact diagonalization as impurity solver, particularly cheap from the computational point of view. This method of solution of the Anderson problem is not exact but quickly converges to a good approximation of the true solution as it is common for variable grid methods (indeed, both the energy levels of the bath and the hybridization of them with the impurity are free to adjust themselves). In Chap. 3 we presented the DMFT with particular emphasis on its ED formulation.

In Chap. 4 we analyzed the system with bands with different bandwidth at quarter filling. For this model, we were able to draw the phase diagrams both in the paramagnetic and the magnetic cases as a function of the Hubbard interaction U and of the bandwidth ratio α. The obtained results are at zero temperature. For what concerns the metallic phase the picture that we get is, to some extent, the opposite with respect to the one for the same model at half filling. There the band with the smaller bandwidth is the more correlated one, instead at quarter filling there are some regimes in which it is the broader band the most correlated. In the insulating state, we observe a spontaneous symmetry breaking of the orbital $U(1)$ symmetry, leading to a canted AFO order in the paramagnetic case. When we allow for the presence of a magnetic kind of order antiferromagnetism settles in for each value of the bandwidth ratio, and we observe the occurrence of an orbital-flip transition at a finite value of α. Particularly, when the two bands have a comparable bandwidth ($\alpha > 0.7$) we observe again the canted AFO order, instead when one band has a bandwidth quite smaller than the other ($\alpha < 0.7$) just the broad band is filled. In any case, the system remains an antiferromagnet across the orbital transition.

Chap. 5 was devoted to the presentation of some experimental and theoretical results about vanadium dioxide that suggest a Mott nature for the insulating phases of VO_2, even if disguised by a lattice distortion that plays an important role for its stabilization. The correlated nature of this compound can be directly observed by looking at the *bad metallic* behaviour of the high-temperature rutile phase. We also introduced a model that can describe some of those features. Particularly, we were able to observe the correct qualitative behaviuor for the transition from a distorted insulator to an undistorted metal induced by increasing the temperature or by decreasing the Hubbard interaction. Moreover, we obtained the proper order of magnitude for several quantities as the energy gap in the monoclinic insulating phase, the energy separation between the bonding and the anti-bonding states and the critical temperature for the occurrence of the first order transition.

Due to a large number of experiments available about vanadium dioxide, it would be interesting to study the dynamics of this model in the out of equilibrium case. Of course, the presence of the lattice distortion complicate the description, and ad hoc methods have to be tailored to treat such problem.

Despite the nice portrait of the material properties that we got from this model study, yet there are some limitations. A better description of the compound can be gained by considering two distinct phonons coupled to the two interactions since there is experimental evidence that the components of the structural phase transition are two. It will be challenging to understand which is the proper range of variation for the coupling constants α, β_1, β_2 and γ that appear in Eq. (5.4), for which we can try to refer to some experimental results [139]. Those considerations pave the way to further theoretical investigation that can lead to a better description of the compound and possibly explain other experimental observations, e.g. the presence of the monoclinic metal.

In Chap. 6 we focused on the derivation of the equations that permit to implement an impurity solver in the NCA or OCA in the equilibrium case and in NCA for the out of equilibrium condition. The equations are suitable for the description of a superconducting or a BEC state. Unfortunately, we did not have time to implement the equations in a code and then to get some results, but we are planning to do so in the next future. The system that we would like to study is, at the present time, a single band model at half-filling with attractive Hubbard interaction U. Since NCA works well in the limit of small hybridizations, i.e., large values of U, we have to work in the region where we have, at low temperatures, the BEC, and at larger temperatures the pseudo-gap phase with preformed pairs. In this case, it would be interesting to study the possibility of a transition from the pseudo-gap phase to the BEC by driving the system out of equilibrium.

Another ongoing project that will be the object of subsequent analysis is related to the results reported in App. A. We consider again a two band system, but with a different occupation with respect to the one mainly considered in this thesis. Indeed, we studied the large U limit of a two bands model at half-filling, allowing for the presence of a crystal field splitting and Hund's coupling. In a model close to the mentioned one [182], studied on a square lattice in a ribbon geometry, a magnetic pattern not of the (π,π) kind is observed, and an explanation for its occurrence is still lacking. We hope to get some information more about this peculiar kind of order by analyzing the strong coupling expansion of a simpler model with respect to the one in which the phenomenon was first observed, but with the same lattice geometry.

Ringraziamenti

Giunto alla conclusione di questo percorso durato quattro anni, le prime persone che voglio ringraziare sono Michele Fabrizio ed Adriano Amaricci, in modo particolare per la pazienza e la disponibilità sempre dimostrata nei miei confronti, nonché per le innumerevoli cose che mi hanno permesso di imparare.
In secondo luogo ringrazio Massimo Capone, con il quale ho avuto il piacere di poter collaborare.

Un ringraziamento particolare va a tutti gli amici che hanno reso questi anni passati a Trieste indimenticabili. Ringrazio Maja, Daniele, Giulia e Tommaso per il tempo trascorso assieme in ufficio (e non solo) ed anche tutti i compagni con cui ho condiviso gioie e dolori del dottorato, con menzione particolare a Simone, Mariam, Loris e Seher. Un saluto, che forse non arriverà mai a destinazione, va a Kang.
Ringrazio inoltre gli amici di vecchia data che si sono trasferiti a Trieste, ossia Tommaso e Federico. Soprattutto Tommaso per avermi sopportato quattro anni come coinquilino.

Infine vorrei ringraziare la mia famiglia e Carmela, per le quali le parole non bastano per esprimere la gratitudine nei loro confronti.

Appendix A

Strong coupling expansion

General derivation

In this section we will follow [183] in order to develop a general formalism that permits to perform a strong coupling expansion for a generic Hamiltonian problem. We consider the Hamiltonian $H = H_0 + V$ that acts on a Hilbert space $\mathscr{H}$. This Hamiltonian satisfies the eigenvalue equation:

$$H|\psi\rangle = E|\psi\rangle\ . \tag{A.1}$$

H_0 has a degenerate ground state, and this manifold belongs to the Hilbert space $\mathscr{H}_0$. The Hamiltonian satisfies the eigenvalue problem:

$$H_0|\psi_0\rangle = E_0|\psi_0\rangle\ .$$

We define two projectors: P, that projects on the Hilbert space $\mathscr{H}_0$, and $Q = 1 - P$, that projects on $\mathscr{H} \setminus \mathscr{H}_0$, so that $P + Q$ acts as the identity on $\mathscr{H}$. We can rewrite Eq. (A.1) as:

$$(P+Q)\,H\,(P+Q)\,|\psi\rangle = E\,(P+Q)\,|\psi\rangle\ ,$$

so on $\mathscr{H}_0$:

$$PHP|\psi\rangle + PHQ|\psi\rangle = EP|\psi\rangle\ , \tag{A.2}$$

and on $\mathscr{H} \setminus \mathscr{H}_0$:

$$QHP|\psi\rangle + QHQ|\psi\rangle = EQ|\psi\rangle\ .$$

Since, for a projector, holds the property $Q^2 = Q$, we can rewrite the last equation as:

$$(E - QHQ)\,Q|\psi\rangle = QHP|\psi\rangle\ ,$$

and, at the end:

$$Q|\psi\rangle = (E - QHQ)^{-1} QHP|\psi\rangle \, . \tag{A.3}$$

By substituting Eq. (A.3) into Eq. (A.2) we get:

$$PHP|\psi\rangle + PHQ\frac{1}{E - QHQ}QHP|\psi\rangle = EP|\psi\rangle \, .$$

Now we can define an effective Hamiltonian H_{eff} that acts on the Hilbert space $\mathscr{H}_0$ starting from the Hamiltonian that acts on the full Hilbert space $\mathscr{H}$:

$$H_{eff} = P(H_0 + V)P + P(H_0 + V)Q\frac{1}{E - QHQ}Q(H_0 + V)P \, .$$

Since H_0 has eigenstates in $\mathscr{H}_0$, the product QH_0P is equal to zero. We can rewrite:

$$H_{eff} = PH_0P + PVP + PVQ\frac{1}{(E_0 - QH_0Q) - (E_0 - E + QVQ)}QVP \, .$$

By using the expansion:

$$\frac{1}{A - B} = \frac{1}{A}\sum_{n=0}^{\infty}\left(B\frac{1}{A}\right)^n \, ,$$

where, in our case, $A = E_0 - QH_0Q$ and $B = E_0 - E + QVQ$, we arrive at the expression

$$\begin{aligned} H_{eff} =& PH_0P + PVP + \\ &+ PVQ\frac{1}{E_0 - QH_0Q}\sum_{n=0}^{\infty}\left[(E_0 - E + QVQ)\frac{1}{E_0 - QH_0Q}\right]^n QVP \, . \end{aligned} \tag{A.4}$$

By stopping the expansion at $n = 0$, we get

$$H_{eff}^{n=0} = PH_0P + PVP + PVQ\frac{1}{E_0 - QH_0Q}QVP \, . \tag{A.5}$$

Eq. (A.4) is not good if we want to go beyond the $n = 0$ limit. In that case we need to know the true ground state energy of the system E that generally is not known. In that case is better to use Kato's perturbation theory.

In the next sections we apply this general formalism to two specific cases:

- two bands at quarter filling with different bandwidth interacting by the Hubbard interaction;
- two un-hybridized bands at half filling with the same bandwidth interacting by the Hubbard and Hund interactions, lifted by a crystal field.

Warming up: the Kugel-Khomskii Hamiltonian

Let us consider a two band Hubbard model with bands with different bandwidth. We consider the system at quarter filling, so with an average occupation of one electron per site. The Hamiltonian of the problem reads as:

$$H = -\sum_{\langle \mathbf{R},\mathbf{R}'\rangle}\sum_{a,b}\sum_{\sigma} t_{a,b}\left(c^{\dagger}_{\mathbf{R},a,\sigma}c_{\mathbf{R}',b,\sigma} + h.c.\right) + \frac{U}{2}\sum_{\mathbf{R}} n_{\mathbf{R}}\left(n_{\mathbf{R}}-1\right) - \mu\sum_{\mathbf{R}} n_{\mathbf{R}} \, . \tag{A.6}$$

with $\mathbf{R}$ and $\mathbf{R}'$ lattice site labels, and the summation over $\mathbf{R}$ and $\mathbf{R}'$ in the kinetic term has to be performed just over nearest-neighbor sites. $c_{\mathbf{R},a,\sigma}$ ($c^{\dagger}_{\mathbf{R},a,\sigma}$) is the annihilation (creation) operator of one electron on site $\mathbf{R}$ in orbital $a = 1,2$ and spin $\sigma = \uparrow,\downarrow$. $n_{\mathbf{R}}$ is the number operator on site $\mathbf{R}$, $t_{a,b}$ the probability amplitude of the hopping process of an electron from orbital b on site $\mathbf{R}'$ to orbital a on site $\mathbf{R}$ nearest neighbor of $\mathbf{R}'$, and vice versa. U is the strength of the Hubbard interaction, and μ the chemical potential that we change in order to fix the occupation. Essentially, the model Eq. (A.6) has the same structure of the one presented in Sec. 4.1, except for the fact that here we are allowing for inter-band hoppings. We want to derive an effective Hamiltonian for model Eq. (A.6) valid in the limit of strong correlation regime $U \gg t_{a,b}\ \forall\ a,b = 1,2$. This problem was already treated by Kugel and Khomskii in [59], and we briefly sketch its derivation. In order to do so we can use Eq. (A.5), with

$$\begin{aligned} H_0 &= \frac{U}{2}\sum_{R} n_R\left(n_R-1\right) - \mu\sum_{R} n_R \, , \\ V &= -\sum_{\langle \mathbf{R},\mathbf{R}'\rangle}\sum_{a,b}\sum_{\sigma} t_{a,b}\left(c^{\dagger}_{\mathbf{R},a,\sigma}c_{\mathbf{R}',b,\sigma} + h.c.\right) \, . \end{aligned} \tag{A.7}$$

Instead of considering the whole lattice, let's restrict the calculation to two nearest neighbor sites $\mathbf{R}$ and $\mathbf{R}'$. In the limit of large interaction, the electrons are localized, so the Hilbert space $\mathscr{H}_0$ on which the projector P acts is the one of one electron states. We can write the states that we use in order to build the projector P as the direct product of the local state with one electron on each of the two sites $\{|\uparrow,0\rangle, |\downarrow,0\rangle, |0,\uparrow\rangle, |0,\downarrow\rangle\}_{\mathbf{R}} \otimes \{|\uparrow,0\rangle, |\downarrow,0\rangle, |0,\uparrow\rangle, |0,\downarrow\rangle\}_{\mathbf{R}'}$ with the convention that $|\uparrow,0\rangle_{\mathbf{R}}$ means that we have one electron with spin up in orbital 1 on site $\mathbf{R}$. Since the kinetic term V changes the occupations on the sites involved in the hopping process, we can conclude that $P\left(V\right)_{\mathbf{R},\mathbf{R}'}P = 0$. For each state that appears in the projector P the expectation value of the Hamiltonian $(H_0)_{\mathbf{R},\mathbf{R}'}$ is equal to -2μ. The action of $(V)_{\mathbf{R},\mathbf{R}'}$ on a state that belongs to $\mathscr{H}_0$ leads the system to arrive in a state that belongs to the set $\{|0,0\rangle\}_{\mathbf{R}} \otimes \{|\uparrow\downarrow,0\rangle, |0,\uparrow\downarrow\rangle, |\uparrow,\downarrow\rangle, |\downarrow,\uparrow\rangle, |\uparrow,\uparrow\rangle, |\downarrow,\downarrow\rangle\}_{\mathbf{R}'} \cup \{|\uparrow\downarrow,0\rangle, |0,\uparrow\downarrow\rangle, |\uparrow,\downarrow\rangle, |\downarrow,\uparrow$

$\rangle, |\uparrow,\uparrow\rangle, |\downarrow,\downarrow\rangle\}_{\mathbf{R}} \otimes \{|0,0\rangle\}_{\mathbf{R}'}$. The projector Q has a non null action just on this subspace of $\mathscr{H} \setminus \mathscr{H}_0$. The expectation value of H_0 on one of those states is always equal to $U - 2\mu$, and since $E_0 = -2\mu$ we can rewrite Eq. (A.5) without the projectors, by simply reminding that the Hamiltonian as to act on the states with one electron per site

$$\begin{aligned} H_{eff}^{\mathbf{R},\mathbf{R}'} = -\frac{1}{U}\sum_{\sigma,\sigma'}\sum_{a,b}\sum_{a',b'} t_{a,b}t_{a',b'}(c^{\dagger}_{\mathbf{R},a,\sigma}c_{\mathbf{R}',b,\sigma}c^{\dagger}_{\mathbf{R}',b',\sigma'}c_{\mathbf{R},a',\sigma'}+ \\ +c^{\dagger}_{\mathbf{R}',b,\sigma}c_{\mathbf{R},a,\sigma}c^{\dagger}_{\mathbf{R},a',\sigma'}\hat{c}_{\mathbf{R}',b',\sigma'}) = \end{aligned} \tag{A.8}$$

$$\begin{aligned} = \frac{1}{U}\sum_{\sigma,\sigma'}\sum_{a,b}\sum_{a',b'} t_{a,b}t_{a',b'}(c^{\dagger}_{\mathbf{R},a,\sigma}c_{\mathbf{R},a',\sigma'}c^{\dagger}_{\mathbf{R}',b',\sigma'}c_{\mathbf{R}',b,\sigma}+ \\ +c^{\dagger}_{\mathbf{R}',b,\sigma}\hat{c}_{\mathbf{R}',b',\sigma'}c^{\dagger}_{\mathbf{R},a',\sigma'}c_{\mathbf{R},a,\sigma})+ \\ -\frac{1}{U}\sum_{\sigma}\sum_{a,a'}\sum_{b} t_{a,b}t_{a',b}(c^{\dagger}_{\mathbf{R},a,\sigma}c_{\mathbf{R},a',\sigma}+c^{\dagger}_{\mathbf{R}',a,\sigma}c_{\mathbf{R}',a',\sigma})\,. \end{aligned}$$

In order to encode directly in the operators the constraint about the number of the electrons per site, we can map the action of couples of fermionic operators in some spin and pseudospin ones. Indeed we can characterize each local state with two quantum numbers, one related to the spin $\langle\sigma^z_{\mathbf{R}}\rangle = \pm 1$, where $\langle\sigma^z_{\mathbf{R}}\rangle = +1$ ($\langle\sigma^z_{\mathbf{R}}\rangle = -1$) means that we have an electron with spin up (down) on site $\mathbf{R}$, and the other related to the orbital or pseudospin degree of freedom $\langle\tau^z_{\mathbf{R}}\rangle = \pm 1$, where $\langle\tau^z_{\mathbf{R}}\rangle = +1$ ($\langle\tau^z_{\mathbf{R}}\rangle = -1$) means that we have one electron in orbital 1 (2) on site $\mathbf{R}$. The mapping is performed as follows:

$$\begin{aligned} c^{\dagger}_{\mathbf{R},a,\uparrow}c_{\mathbf{R},a,\downarrow} &\longrightarrow \left(\frac{1}{2}+(-1)^{a-1}\tau^z_{\mathbf{R}}\right)\sigma^+_{\mathbf{R}}\,, \\ c^{\dagger}_{\mathbf{R},a,\downarrow}c_{\mathbf{R},a,\uparrow} &\longrightarrow \left(\frac{1}{2}+(-1)^{a-1}\tau^z_{\mathbf{R}}\right)\sigma^-_{\mathbf{R}}\,, \\ c^{\dagger}_{\mathbf{R},1,\sigma}c_{\mathbf{R},2,\sigma} &\longrightarrow \tau^+_{\mathbf{R}}\left(\frac{1}{2}+(-1)^{\sigma-1}\sigma^z_{\mathbf{R}}\right)\,, \\ c^{\dagger}_{\mathbf{R},2,\sigma}c_{\mathbf{R},1,\sigma} &\longrightarrow \tau^-_{\mathbf{R}}\left(\frac{1}{2}+(-1)^{\sigma-1}\sigma^z_{\mathbf{R}}\right)\,, \\ c^{\dagger}_{\mathbf{R},a,\sigma}c_{\mathbf{R},a,\sigma} &\longrightarrow \left(\frac{1}{2}+(-1)^{a-1}\tau^z_{\mathbf{R}}\right)\left(\frac{1}{2}+(-1)^{\sigma-1}\sigma^z_{\mathbf{R}}\right)\,, \\ c^{\dagger}_{\mathbf{R},1,\uparrow}c_{\mathbf{R},2,\downarrow} &\longrightarrow \tau^+_{\mathbf{R}}\sigma^+_{\mathbf{R}}\,, \\ c^{\dagger}_{\mathbf{R},1,\downarrow}c_{\mathbf{R},2,\uparrow} &\longrightarrow \tau^+_{\mathbf{R}}\sigma^-_{\mathbf{R}}\,, \\ c^{\dagger}_{\mathbf{R},2,\uparrow}c_{\mathbf{R},1,\downarrow} &\longrightarrow \tau^-_{\mathbf{R}}\sigma^+_{\mathbf{R}}\,, \\ c^{\dagger}_{\mathbf{R},2,\downarrow}c_{\mathbf{R},1,\uparrow} &\longrightarrow \tau^-_{\mathbf{R}}\sigma^-_{\mathbf{R}}\,. \end{aligned} \tag{A.9}$$

With this map we are reducing the local Hilbert space of the problem from the dimension of 16 ($\{|\,0,0\rangle, |\uparrow,0\rangle, |\downarrow,0\rangle, |\,0,\uparrow\rangle, |\,0,\downarrow\rangle, |\uparrow\downarrow,0\rangle, |\,0,\uparrow\downarrow\rangle, |\uparrow,\downarrow\rangle, |\downarrow,\uparrow\rangle, |\uparrow,\uparrow\rangle, |\downarrow,\downarrow\rangle, |\uparrow\downarrow,\uparrow\rangle, |\uparrow\downarrow,\downarrow\rangle, |\uparrow,\uparrow\downarrow\rangle, |\downarrow,\uparrow\downarrow\rangle, |\uparrow\downarrow,\uparrow\downarrow\rangle\}$) to the dimension of 4 ($\{|\uparrow,0\rangle, |\downarrow,0,\rangle, |\,0,\uparrow\rangle, |\,0,\downarrow\rangle\}$) . This is allowed since we are in the limit of huge interaction compared to the kinetic term, so the charge fluctuations are suppressed.
By performing the substitutions we arrive at the form

$$\begin{aligned}
H_{eff}^{\mathbf{R},\mathbf{R}'} = \frac{1}{4U}\left(1+\boldsymbol{\sigma}_{\mathbf{R}}\cdot\boldsymbol{\sigma}_{\mathbf{R}'}\right)\{ & t_{11}^2+t_{22}^2+2t_{12}^2+\left(t_{11}^2-t_{22}^2\right)\left(\tau_{\mathbf{R}}^z+\tau_{\mathbf{R}'}^z\right)+ \\
& +\left(t_{11}^2+t_{22}^2-2t_{12}^2\right)\tau_{\mathbf{R}}^z\tau_{\mathbf{R}'}^z+2t_{12}\left[t_{11}+t_{22}+\left(t_{11}-t_{22}\right)\tau_{\mathbf{R}}^z\right]\tau_{\mathbf{R}'}^x+ \\
& +2t_{12}\left[t_{11}+t_{22}+\left(t_{11}-t_{22}\right)\tau_{\mathbf{R}'}^z\right]\tau_{\mathbf{R}}^x+ \\
& +2\left[t_{11}t_{22}\left(\tau_{\mathbf{R}}^x\tau_{\mathbf{R}'}^x+\tau_{\mathbf{R}}^y\tau_{\mathbf{R}'}^y\right)+t_{12}^2\left(\tau_{\mathbf{R}}^x\tau_{\mathbf{R}'}^x-\tau_{\mathbf{R}}^y\tau_{\mathbf{R}'}^y\right)\right]\}+ \\
& -\frac{t_{12}}{U}\left(t_{11}+t_{22}\right)\left(\tau_{\mathbf{R}}^x+\tau_{\mathbf{R}'}^x\right)-\frac{1}{2U}\left(t_{11}^2-t_{22}^2\right)\left(\tau_{\mathbf{R}}^z+\tau_{\mathbf{R}'}^z\right)+ \\
& -\frac{1}{U}\left(t_{11}^2+t_{22}^2+2t_{12}^2\right)\ .
\end{aligned} \tag{A.10}$$

If we impose $t_{12}=0$, $t_{11}=1/2$ and $t_{22}=\alpha/2$, we get $H_{\mathrm{KK}}=\frac{1}{z}\sum_{\langle\mathbf{R},\mathbf{R}'\rangle}H_{eff}^{\mathbf{R},\mathbf{R}'}$ encountered in Eq. (4.6).

A less-trivial derivation: two bands at half filling

We consider a two-band Hubbard model with bands with different bandwidth. The system is at half filling, so with an average occupation of two electrons per site. The Hamiltonian of the problem reads as:

$$\begin{aligned}
H = & -\sum_{\langle\mathbf{R},\mathbf{R}'\rangle}\sum_{a,b}\sum_{\sigma}t_{a,b}\left(c_{\mathbf{R},a,\sigma}^{\dagger}c_{\mathbf{R}',b,\sigma}+h.c.\right)+\frac{U}{2}\sum_{\mathbf{R}}n_{\mathbf{R}}\left(n_{\mathbf{R}}-1\right) \\
& -\Delta\sum_{\mathbf{R}}\left(n_{\mathbf{R},1}-n_{\mathbf{R},2}\right)-\frac{2}{3}JN_s+J\sum_{\mathbf{R}}\left(\boldsymbol{\tau}_{\mathbf{R}}^2-\left(\tau_{\mathbf{R}}^z\right)^2\right)\ .
\end{aligned} \tag{A.11}$$

Δ is a crystal field term, instead J represents the intensity of the Hund's coupling. In the following we will consider a situation of the kind $U > J, \Delta \gg t_{a,b}$. We can divide the

Hamiltonian as:

$$\begin{aligned}
H_0 &= \frac{U}{2}\sum_R n_R\,(n_R-1)\ , \\
V &= -\sum_{\langle \mathbf{R},\mathbf{R}'\rangle}\sum_{a,b}\sum_{\sigma} t_{a,b}\left(c^{\dagger}_{\mathbf{R},a,\sigma}c_{\mathbf{R}',b,\sigma}+h.c.\right)-\Delta\sum_{\mathbf{R}}\left(n_{\mathbf{R},1}-n_{\mathbf{R},2}\right)-\frac{2}{3}JN_s+J\sum_{\mathbf{R}}\left(\boldsymbol{\tau}^2_{\mathbf{R}}-\left(\tau^z_{\mathbf{R}}\right)^2\right)\ .
\end{aligned} \tag{A.12}$$

The first part of the expansion will be the same as before, with the only difference that, since this time we have two electrons per site, the denominator of Eq. (A.5) will be equal to $-2U$ instead of $-U$ as in Sec. A. The subspace in which we act is given by the local states $\{|\uparrow\downarrow,0\rangle,|0,\uparrow\downarrow\rangle,|\uparrow,\downarrow\rangle,|\downarrow,\uparrow\rangle,|\uparrow,\uparrow\rangle,|\downarrow,\downarrow\rangle\}_{\mathbf{R}}$. Those states can be identified by using four quantum numbers, like the total spin σ, its z component σ^z, the total pseudospin τ and its z component τ^z. We can write:

$$\begin{aligned}
|\uparrow,\uparrow\rangle &= |\sigma=1,\sigma^z=+1;\tau=0,\tau^z=0\rangle\ , \\
|\downarrow,\downarrow\rangle &= |\sigma=1,\sigma^z=-1;\tau=0,\tau^z=0\rangle\ , \\
\frac{|\uparrow,\downarrow\rangle+|\downarrow,\uparrow\rangle}{\sqrt{2}} &= |\sigma=1,\sigma^z=0;\tau=0,\tau^z=0\rangle\ , \\
\frac{|\uparrow,\downarrow\rangle-|\downarrow,\uparrow\rangle}{\sqrt{2}} &= |\sigma=0,\sigma^z=0;\tau=1,\tau^z=0\rangle\ , \\
|\uparrow\downarrow,0\rangle &= |\sigma=0,\sigma^z=0;\tau=1,\tau^z=+1\rangle\ , \\
|0,\uparrow\downarrow\rangle &= |\sigma=0,\sigma^z=0;\tau=1,\tau^z=-1\rangle\ .
\end{aligned}$$

Once we have mapped the states on those generalized angular momenta, we can map them on some bosonic states through the Schwinger's map [184, 185], that works as:

$$\begin{aligned}
\sigma^+ &\longrightarrow a^{\dagger}_{s,1}a_{s,2}\ , \\
\sigma^- &\longrightarrow a^{\dagger}_{s,2}a_{s,1}\ , \\
\sigma^z &\longrightarrow \frac{1}{2}\left(n_{s,1}-n_{s,2}\right)\ , \\
\boldsymbol{\sigma}^2 &\longrightarrow \frac{1}{4}\left(n_{s,1}+n_{s,2}+1\right)^2-\frac{1}{4}\ ,
\end{aligned}$$

with $a_{s,l}$ ($a^{\dagger}_{s,l}$) the bosonic operator that annihilates (creates) a boson in a level $l=1,2$. Essentially, we map the spin and the pseudospin degree of freedom into two bosonic states each, so the map for the states becomes:

$$
\begin{aligned}
&|\uparrow,\uparrow\rangle = |\sigma=1,\sigma^z=+1;\tau=0,\tau^z=0\rangle = |n_{s,1}=2,n_{s,2}=0;n_{t,1}=0,n_{t,2}=0\rangle\ ,\\
&|\downarrow,\downarrow\rangle = |\sigma=1,\sigma^z=-1;\tau=0,\tau^z=0\rangle = |n_{s,1}=0,n_{s,2}=2;n_{t,1}=0,n_{t,2}=0\rangle\ ,\\
&\frac{|\uparrow,\downarrow\rangle+|\downarrow,\uparrow\rangle}{\sqrt{2}} = |\sigma=1,\sigma^z=0;\tau=0,\tau^z=0\rangle = |n_{s,1}=1,n_{s,2}=1;n_{t,1}=0,n_{t,2}=0\rangle\ ,\\
&\frac{|\uparrow,\downarrow\rangle-|\downarrow,\uparrow\rangle}{\sqrt{2}} = |\sigma=0,\sigma^z=0;\tau=1,\tau^z=0\rangle = |n_{s,1}=0,n_{s,2}=0;n_{t,1}=1,n_{t,2}=1\rangle\ ,\\
&|\uparrow\downarrow,0\rangle = |\sigma=0,\sigma^z=0;\tau=1,\tau^z=+1\rangle = |n_{s,1}=0,n_{s,2}=0;n_{t,1}=2,n_{t,2}=0\rangle\ ,\\
&|0,\uparrow\downarrow\rangle = |\sigma=0,\sigma^z=0;\tau=1,\tau^z=-1\rangle = |n_{s,1}=0,n_{s,2}=0;n_{t,1}=0,n_{t,2}=2\rangle\ .
\end{aligned}
$$

It is useful to have the states written this way because the combination of two hopping processes (one electron that moves from one site and another one that go back to the original lattice position) can change all the four local quantum numbers of the starting configuration. This means that the total spin and the total pseudospin are generally not conserved quantities. Since it is not easy to write down an operator that does not conserve the total angular momentum when it has to act on the basis of the total angular momentum and its z component [186], it is better to use this other basis, where the action of an operator of that kind is trivial.

By defining few operators, we can perform a quite compact mapping of couples of fermionic operators:

$$
\begin{aligned}
n_{\mathbf{R},a,\sigma} &\longrightarrow \begin{array}{l} \frac{1}{2}\left(K^z_{s,\mathbf{R}}+(-1)^{\sigma-1}\,\sigma^z_{\mathbf{R}}+K^z_{t,\mathbf{R}}+(-1)^{a-1}\,\tau^z_{\mathbf{R}}\right)+ \\ (-1)^{\sigma-1}(-1)^{a-1}\left(K^x_{s,\mathbf{R}}K^x_{t,\mathbf{R}}+K^y_{s,\mathbf{R}}K^y_{t,\mathbf{R}}\right) \end{array}\ ,\\
c^\dagger_{\mathbf{R},a,\sigma}c_{\mathbf{R},a,\bar{\sigma}} &\longrightarrow \begin{array}{l} \left(K^z_{s,\mathbf{R}}-1\right)\sigma^\sigma_{\mathbf{R}}- \\ (-1)^{a-1}\left[K^x_{t,\mathbf{R}}Q^x_{s,\mathbf{R}}+K^y_{t,\mathbf{R}}Q^y_{s,\mathbf{R}}+i(-1)^{\sigma-1}\left(K^x_{t,\mathbf{R}}P^y_{s,\mathbf{R}}-K^y_{t,\mathbf{R}}P^x_{s,\mathbf{R}}\right)\right] \end{array}\ ,\\
c^\dagger_{\mathbf{R},a,\sigma}c_{\mathbf{R},\bar{a},\sigma} &\longrightarrow \begin{array}{l} \left(K^z_{t,\mathbf{R}}-1\right)\tau^a_{\mathbf{R}}- \\ (-1)^{\sigma-1}\left[K^x_{s,\mathbf{R}}Q^x_{t,\mathbf{R}}+K^y_{s,\mathbf{R}}Q^y_{t,\mathbf{R}}+i(-1)^{\sigma-1}\left(K^x_{s,\mathbf{R}}P^y_{t,\mathbf{R}}-K^y_{s,\mathbf{R}}P^x_{t,\mathbf{R}}\right)\right] \end{array}\ ,\\
c^\dagger_{\mathbf{R},a,\sigma}c_{\mathbf{R},\bar{a},\bar{\sigma}} &\longrightarrow \begin{array}{l} \left[Q^x_{s,\mathbf{R}}Q^x_{t,\mathbf{R}}+Q^y_{s,\mathbf{R}}Q^y_{t,\mathbf{R}}-(-1)^{\sigma-1}(-1)^{a-1}\left(P^x_{s,\mathbf{R}}P^x_{t,\mathbf{R}}+P^y_{s,\mathbf{R}}P^y_{t,\mathbf{R}}\right)\right]+ \\ i\left[(-1)^{\sigma-1}\left(P^y_{s,\mathbf{R}}Q^x_{t,\mathbf{R}}-P^x_{s,\mathbf{R}}Q^y_{t,\mathbf{R}}\right)+(-1)^{a-1}\left(Q^x_{s,\mathbf{R}}P^y_{t,\mathbf{R}}-Q^y_{s,\mathbf{R}}P^x_{t,\mathbf{R}}\right)\right] \end{array}\ ,
\end{aligned}
\tag{A.13}
$$

where $\tau^1 = \tau^+$ ($\tau^2 = \tau^-$), $\sigma^\uparrow = \sigma^+$ ($\sigma^\downarrow = \sigma^-$) and:

$$\begin{aligned}
K^z_{\Gamma,\mathbf{R}} &= \frac{1}{2}\left(1 + n_{\Gamma,\mathbf{R},1} + n_{\Gamma,\mathbf{R},2}\right) \, , \\
K^+_{\Gamma,\mathbf{R}} &= a^\dagger_{\Gamma,\mathbf{R},1} a^\dagger_{\Gamma,\mathbf{R},2} \, , \\
K^-_{\Gamma,\mathbf{R}} &= a_{\Gamma,\mathbf{R},1} a_{\Gamma,\mathbf{R},2} \, , \\
P^+_{\Gamma,\mathbf{R}} &= \frac{1}{2}\left(\left(a^\dagger_{\Gamma,\mathbf{R},1}\right)^2 + \left(a^\dagger_{\Gamma,\mathbf{R},2}\right)^2\right) \, , \\
P^-_{\Gamma,\mathbf{R}} &= \frac{1}{2}\left(\left(a_{\Gamma,\mathbf{R},1}\right)^2 + \left(a_{\Gamma,\mathbf{R},2}\right)^2\right) \, , \\
Q^+_{\Gamma,\mathbf{R}} &= \frac{1}{2}\left(\left(a^\dagger_{\Gamma,\mathbf{R},1}\right)^2 - \left(a^\dagger_{\Gamma,\mathbf{R},2}\right)^2\right) \, , \\
Q^-_{\Gamma,\mathbf{R}} &= \frac{1}{2}\left(\left(a_{\Gamma,\mathbf{R},1}\right)^2 - \left(a_{\Gamma,\mathbf{R},2}\right)^2\right) \, ,
\end{aligned} \tag{A.14}$$

with $\Gamma = s,t$. The K operators are the ones introduced by Schwinger. They satisfy an hyperbolic algebra and K^+ and K^- change the value of the total angular momentum. The P and Q operators change, instead, also the z component and not just the total angular momentum. Even if those operators permit to write the effective Hamiltonian in a more compact way, they do not encode the constrain about the occupation of two particles for each state. The simplest way in which we can impose it is through a projection of the Hamiltonian that we get on the generic local wave-function:

$$|\psi_\mathbf{R}\rangle = \sum_{n=1}^{6} c_\mathbf{R}(n)\, |n\rangle_\mathbf{R} \, , \tag{A.15}$$

having labeled:

$$\begin{aligned}
|1\rangle &= |n_{s,1} = 2, n_{s,2} = 0; n_{t,1} = 0, n_{t,2} = 0\rangle \, , \\
|2\rangle &= |n_{s,1} = 1, n_{s,2} = 1; n_{t,1} = 0, n_{t,2} = 0\rangle \, , \\
|3\rangle &= |n_{s,1} = 0, n_{s,2} = 2; n_{t,1} = 0, n_{t,2} = 0\rangle \, , \\
|4\rangle &= |n_{s,1} = 0, n_{s,2} = 0; n_{t,1} = 2, n_{t,2} = 0\rangle \, , \\
|5\rangle &= |n_{s,1} = 0, n_{s,2} = 0; n_{t,1} = 1, n_{t,2} = 1\rangle \, , \\
|6\rangle &= |n_{s,1} = 0, n_{s,2} = 0; n_{t,1} = 0, n_{t,2} = 2\rangle \, .
\end{aligned}$$

Without any loss of generality, we can assume a real local wave-function in Eq. (A.15). When $t_{11} = t_{22} = t$, the average value of the effective two sites Hamiltonian is equal to

$$
\begin{aligned}
H_{eff}^{\mathbf{R},\mathbf{R}'} = & \frac{t^2+t_{12}^2}{U}\left[\left(c_{\mathbf{R}}(1)^2 - c_{\mathbf{R}}(3)^2\right)\left(c_{\mathbf{R}'}(1)^2 - c_{\mathbf{R}'}(3)^2\right) - 1\right] + \\
& \frac{t^2-t_{12}^2}{U}\left(c_{\mathbf{R}}(4)^2 - c_{\mathbf{R}}(6)^2\right)\left(c_{\mathbf{R}'}(4)^2 - c_{\mathbf{R}'}(6)^2\right) + \\
& \frac{2\left(t^2+t_{12}^2\right)}{U} c_{\mathbf{R}}(2)\left(c_{\mathbf{R}}(1) + c_{\mathbf{R}}(3)\right) c_{\mathbf{R}'}(2)\left(c_{\mathbf{R}'}(1) + c_{\mathbf{R}'}(3)\right) + \\
& \frac{2\left(t^2-t_{12}^2\right)}{U} c_{\mathbf{R}}(5)\left(c_{\mathbf{R}}(1) - c_{\mathbf{R}}(3)\right) c_{\mathbf{R}'}(5)\left(c_{\mathbf{R}'}(1) - c_{\mathbf{R}'}(3)\right) + \\
& \frac{4\left(t^2-t_{12}^2\right)}{U} c_{\mathbf{R}}(2) c_{\mathbf{R}}(5) c_{\mathbf{R}'}(2) c_{\mathbf{R}'}(5) + \\
& \frac{2\sqrt{2}t\, t_{12}}{U}[\left(c_{\mathbf{R}}(1)^2 - c_{\mathbf{R}}(3)^2\right) c_{\mathbf{R}'}(2)\left(c_{\mathbf{R}'}(4) - c_{\mathbf{R}'}(6)\right) + \\
& \left(c_{\mathbf{R}'}(1)^2 - c_{\mathbf{R}'}(3)^2\right) c_{\mathbf{R}}(2)\left(c_{\mathbf{R}}(4) - c_{\mathbf{R}}(6)\right) + \\
& c_{\mathbf{R}}(2)\left(c_{\mathbf{R}}(1) + c_{\mathbf{R}}(3)\right)\left(c_{\mathbf{R}'}(1) - c_{\mathbf{R}'}(3)\right)\left(c_{\mathbf{R}'}(4) - c_{\mathbf{R}'}(6)\right) + \\
& c_{\mathbf{R}'}(2)\left(c_{\mathbf{R}'}(1) + c_{\mathbf{R}'}(3)\right)\left(c_{\mathbf{R}}(1) - c_{\mathbf{R}}(3)\right)\left(c_{\mathbf{R}}(4) - c_{\mathbf{R}}(6)\right)] + \\
& \frac{2t^2}{U}[c_{\mathbf{R}}(5)\left(c_{\mathbf{R}}(4) + c_{\mathbf{R}}(6)\right) c_{\mathbf{R}'}(5)\left(c_{\mathbf{R}'}(4) + c_{\mathbf{R}'}(6)\right) + \\
& c_{\mathbf{R}}(2)\left(c_{\mathbf{R}}(4) - c_{\mathbf{R}}(6)\right) c_{\mathbf{R}'}(2)\left(c_{\mathbf{R}'}(4) - c_{\mathbf{R}'}(6)\right) + \\
& \left(c_{\mathbf{R}}(4) c_{\mathbf{R}}(1) + c_{\mathbf{R}}(6) c_{\mathbf{R}}(3)\right)\left(c_{\mathbf{R}'}(4) c_{\mathbf{R}'}(1) + c_{\mathbf{R}'}(6) c_{\mathbf{R}'}(3)\right) + \\
& \left(c_{\mathbf{R}}(4) c_{\mathbf{R}}(3) + c_{\mathbf{R}}(6) c_{\mathbf{R}}(1)\right)\left(c_{\mathbf{R}'}(4) c_{\mathbf{R}'}(3) + c_{\mathbf{R}'}(6) c_{\mathbf{R}'}(1)\right)] + \\
& \frac{2t_{12}^2}{U}[c_{\mathbf{R}}(5)\left(c_{\mathbf{R}}(4) + c_{\mathbf{R}}(6)\right) c_{\mathbf{R}'}(5)\left(c_{\mathbf{R}'}(4) + c_{\mathbf{R}'}(6)\right) + \\
& c_{\mathbf{R}}(2)\left(c_{\mathbf{R}}(4) - c_{\mathbf{R}}(6)\right) c_{\mathbf{R}'}(2)\left(c_{\mathbf{R}'}(4) - c_{\mathbf{R}'}(6)\right) - \\
& \left(c_{\mathbf{R}}(4) c_{\mathbf{R}}(1) + c_{\mathbf{R}}(6) c_{\mathbf{R}}(3)\right)\left(c_{\mathbf{R}'}(4) c_{\mathbf{R}'}(1) + c_{\mathbf{R}'}(6) c_{\mathbf{R}'}(3)\right) - \\
& \left(c_{\mathbf{R}}(4) c_{\mathbf{R}}(3) + c_{\mathbf{R}}(6) c_{\mathbf{R}}(1)\right)\left(c_{\mathbf{R}'}(4) c_{\mathbf{R}'}(3) + c_{\mathbf{R}'}(6) c_{\mathbf{R}'}(1)\right)] + \\
& 2U - 2\Delta\left(c_{\mathbf{R}}(4)^2 - c_{\mathbf{R}}(6)^2 + c_{\mathbf{R}'}(4)^2 - c_{\mathbf{R}'}(6)^2\right) - \frac{4}{3}J + \\
& 2J\left(c_{\mathbf{R}}(5)^2 + c_{\mathbf{R}'}(5)^2\right) + J\left(c_{\mathbf{R}}(4)^2 + c_{\mathbf{R}}(6)^2 + c_{\mathbf{R}'}(4)^2 + c_{\mathbf{R}'}(6)^2\right) .
\end{aligned}
\tag{A.16}
$$

In order to find the ground state of the Hamiltonian we have to minimize this expression with respect to all the $c_{\mathbf{R}}(n)$ parameters.

Appendix B

Useful out of equilibrium relations

Green's function on the Keldysh contour

In order to avoid an abuse of terminology, we will refer, in the following, to the Kostantinov-Perel contour in Fig. B.1 as to the Keldysh contour. As shown in Fig. B.1 we can divide the contour in three branches $C_1 = \left(t_0^-, \tilde{t}\right)$, $C_2 = \left(\tilde{t}, t_0^+\right)$ and $C_3 = \left(t_0^+, t_0 - i\beta\right)$. We can also introduce the generic Green's function:

$$G\left(t,t'\right) = -i\langle T_C c\left(t\right) c^\dagger\left(t'\right)\rangle \ ,$$

where we omitted the indexes of the operators to simplify the notation. We can introduce the 3×3 matrix $G_{\alpha,\beta}\left(t,t'\right)$ with $t \in C_\alpha$ and $t' \in C_\beta$, $\alpha, \beta = 1,2,3$.
Let's now assume that $t \leq t'$ and take into account $G_{11}\left(t,t'\right)$ (Fig. B.2) and $G_{12}\left(t,t'\right)$ (Fig. B.3). By comparing Fig. B.2 with Fig. B.3 we realize that the part of the Keldysh contour that is included in Fig. B.3 and not in Fig. B.2 cancels out. From this consideration

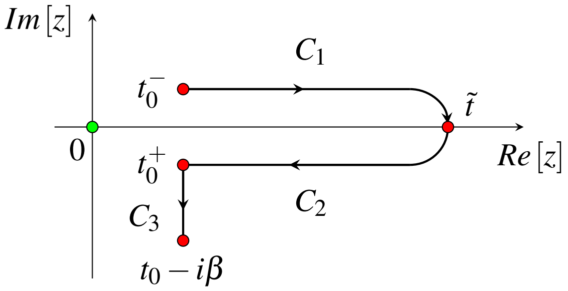

Figure B.1: Kostantinov-Perel contour $C = C_1 \cup C_2 \cup C_3$ in the complex plane.

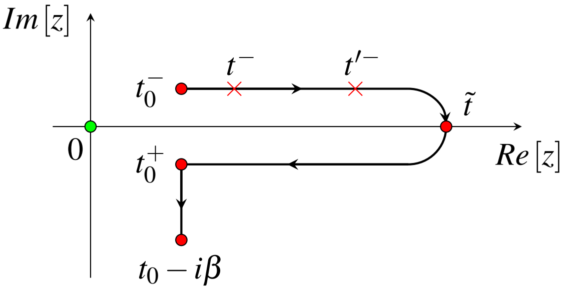
$Im[z]$
t_0^-
t^-
t'^-
$\tilde{t}$
0
$Re[z]$
t_0^+
$t_0 - i\beta$

Figure B.2: Kostantinov-Perel contour C in the complex plane. Case in which both t and t' belong to the branch C_1.

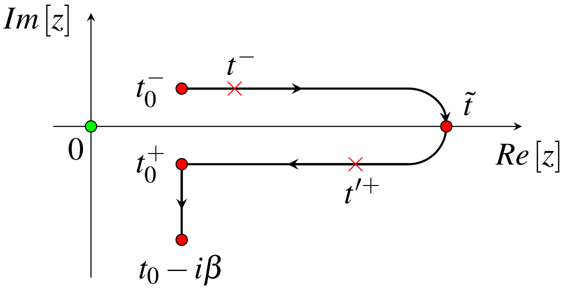
$Im[z]$
t_0^-
t^-
$\tilde{t}$
0
$Re[z]$
t_0^+
t'^+
$t_0 - i\beta$

Figure B.3: Kostantinov-Perel contour C in the complex plane. Case in which t belongs to the branch C_1 and t' belongs to C_2.

follows that:

$$G_{11}\left(t,t'\right)=G_{12}\left(t,t'\right)\ ,\ t\leq t'\ .$$

In the same way we can show that:

$$\begin{aligned}
&G_{11}\left(t,t'\right)=G_{21}\left(t,t'\right)\ ,\ t>t'\ ,\\
&G_{22}\left(t,t'\right)=G_{21}\left(t,t'\right)\ ,\ t<t'\ ,\\
&G_{22}\left(t,t'\right)=G_{12}\left(t,t'\right)\ ,\ t\geq t'\ ,\\
&G_{13}\left(t,\tau'\right)=G_{23}\left(t,\tau'\right)\ ,\\
&G_{31}\left(\tau,t'\right)=G_{32}\left(\tau,t'\right)\ .
\end{aligned}$$

By summing some of those relations, we get:

$$G_{11}\left(t,t'\right)+G_{22}\left(t,t'\right)=G_{12}\left(t,t'\right)+G_{21}\left(t,t'\right)\ .$$

Due to the presence of three constrains

$$\begin{aligned}
&G_{11}\left(t,t'\right)+G_{22}\left(t,t'\right)=G_{12}\left(t,t'\right)+G_{21}\left(t,t'\right)\ ,\\
&G_{13}\left(t,\tau'\right)=G_{23}\left(t,\tau'\right)\ ,\\
&G_{31}\left(\tau,t'\right)=G_{32}\left(\tau,t'\right)\ ,
\end{aligned}$$

just six of the nine components $G_{\alpha,\beta}\left(t,t'\right)$ are independent. Now we want to establish a connection among the Keldysh components of the Green's function and the real time ones. We start by considering the lesser component, defined as

$$G^{<}\left(t,t'\right)=i\langle c^{\dagger}\left(t'\right)c\left(t\right)\rangle\ .$$

This expression does not change if we are in the regime of $t>t'$ or $t'>t$, where t and t' are defined on the real axis. If we want to pass on the Keldysh contour, we have to compare the previous expression with:

$$G_{12}\left(t,t'\right)=-i\langle T_{C}c\left(t^{-}\right)c^{\dagger}\left(t'^{+}\right)\rangle=i\langle c^{\dagger}\left(t'\right)c\left(t\right)\rangle\ ,$$

so that:

$$G^{<}\left(t,t'\right)=G_{12}\left(t,t'\right)\ .$$

In the same way we can write all the other components, which are the greater, the retarded, the Matsubara, the left and the right mixing Green's functions:

$$
\begin{aligned}
&G^{>}\left(t,t'\right) = -i\langle c\left(t\right)c^{\dagger}\left(t'\right)\rangle = G_{21}\left(t,t'\right) \ , \\
&G^{R}\left(t,t'\right) = -i\theta\left(t-t'\right)\langle\{c\left(t\right),c^{\dagger}\left(t'\right)\}\rangle = \frac{1}{2}\left[G_{11}\left(t,t'\right)+G_{21}\left(t,t'\right)-G_{22}\left(t,t'\right)-G_{12}\left(t,t'\right)\right] \ , \\
&G^{M}\left(\tau,\tau'\right) = -\langle T_{\tau}c\left(\tau\right)c^{\dagger}\left(\tau'\right)\rangle = -iG_{33}\left(\tau,\tau'\right) \ , \\
&G^{\neg}\left(t,\tau'\right) = i\langle c^{\dagger}\left(\tau'\right)c\left(t\right)\rangle = \frac{1}{2}\left[G_{13}\left(t,\tau'\right)+G_{23}\left(t,\tau'\right)\right] \ , \\
&G^{\ulcorner}\left(\tau,t'\right) = -i\langle c\left(\tau\right)c^{\dagger}\left(t'\right)\rangle = \frac{1}{2}\left[G_{31}\left(\tau,t'\right)+G_{32}\left(\tau,t'\right)\right] \ .
\end{aligned}
$$

In principle we have defined six linearly independent functions, so we do not have to compute any other. Anyway it can be useful to write down also the remaining components in order to have all of them, so that we can choose which ones are more suitable for the implementation. For this reason we consider also the advanced and the Keldysh Green's functions

$$
\begin{aligned}
&G^{A}\left(t,t'\right) = i\theta\left(t'-t\right)\langle\{c\left(t\right),c^{\dagger}\left(t'\right)\}\rangle = \frac{1}{2}\left[G_{11}\left(t,t'\right)-G_{21}\left(t,t'\right)-G_{22}\left(t,t'\right)+G_{12}\left(t,t'\right)\right] \ , \\
&G^{K}\left(t,t'\right) = -i\langle\left[c\left(t\right),c^{\dagger}\left(t'\right)\right]\rangle = \frac{1}{2}\left[G_{11}\left(t,t'\right)+G_{21}\left(t,t'\right)+G_{22}\left(t,t'\right)+G_{12}\left(t,t'\right)\right] \ .
\end{aligned}
$$

There are some non linear operators that connect the different components. We write:

$$
\begin{aligned}
\left[G^{<}\left(t,t'\right)\right]^{*} &= -G^{<}\left(t',t\right) \ , \\
\left[G^{>}\left(t,t'\right)\right]^{*} &= -G^{>}\left(t',t\right) \ , \\
\left[G^{R}\left(t,t'\right)\right]^{*} &= G^{A}\left(t',t\right) \ , \\
\left[G^{\neg}\left(t,\tau'\right)\right]^{*} &= G^{\ulcorner}\left(\beta-\tau',t\right) \ , \\
G^{M}\left(\tau,\tau'\right) &= G^{M}\left(\tau-\tau'\right) \ , \\
\left[G^{M}\left(\tau\right)\right]^{*} &= G^{M}\left(\tau\right) \ ,
\end{aligned}
$$

so the Matsubara Green's function is real. The boundary conditions for the Green's function on C are given by:

$$
\begin{aligned}
G\left(0^{-},t\right) &= -G\left(-i\beta,t\right) \ , \\
G\left(t,0^{-}\right) &= -G\left(t,-i\beta\right) \ .
\end{aligned}
$$

Different components of the hybridization function

The hybridization function on the Keldysh contour is defined as:

$$\bar{\Delta}_{ab}\left(t,t'\right)=\frac{i}{N_s}\sum_p\begin{pmatrix}V^{a*}_{p,\uparrow} & 0\\ 0 & V^{a}_{-p,\downarrow}\end{pmatrix}\langle T_C\psi_p\left(t\right)\otimes\psi^{\dagger}_p\left(t'\right)\rangle\begin{pmatrix}V^{b}_{p,\uparrow} & 0\\ 0 & V^{b*}_{-p,\downarrow}\end{pmatrix}=$$

$$=\frac{i}{N_s}\sum_p\begin{pmatrix}V^{a*}_{p,\uparrow} & 0\\ 0 & V^{a}_{-p,\downarrow}\end{pmatrix}\begin{pmatrix}\langle T_C c_{p,\uparrow}\left(t\right)c^{\dagger}_{p,\uparrow}\left(t'\right)\rangle & \langle T_C c_{p,\uparrow}\left(t\right)c_{-p,\downarrow}\left(t'\right)\rangle\\ \langle T_C c^{\dagger}_{-p,\downarrow}\left(t\right)c^{\dagger}_{p,\uparrow}\left(t'\right)\rangle & \langle T_C c^{\dagger}_{-p,\downarrow}\left(t\right)c_{-p,\downarrow}\left(t'\right)\rangle\end{pmatrix}\begin{pmatrix}V^{b}_{p,\uparrow} & 0\\ 0 & V^{b*}_{-p,\downarrow}\end{pmatrix},$$

and by reminding that the expression of the Nambu spinor of the bath in terms of its eigenoperators is:

$$\psi_p=\begin{pmatrix}e^{i\phi}\left[\cos\left(\theta_p\right)\gamma_{2,p}+\sin\left(\theta_p\right)\gamma_{1,p}\right]\\ e^{-i\phi}\left[-\sin\left(\theta_p\right)\gamma_{2,p}+\cos\left(\theta_p\right)\gamma_{1,p}\right]\end{pmatrix},$$

we can compute all the components of the hybridization function. We can start by considering the lesser one:

$$K^{<}\left(t,t'\right)=i\langle\psi^{\dagger}_p\left(t'\right)\otimes\psi_p\left(t\right)\rangle=i\begin{pmatrix}\langle c^{\dagger}_{p,\uparrow}\left(t'\right)c_{p,\uparrow}\left(t\right)\rangle & \langle c^{\dagger}_{p,\uparrow}\left(t'\right)c^{\dagger}_{-p,\downarrow}\left(t\right)\rangle\\ \langle c_{-p,\downarrow}\left(t'\right)c_{p,\uparrow}\left(t\right)\rangle & \langle c_{-p,\downarrow}\left(t'\right)c^{\dagger}_{-p,\downarrow}\left(t\right)\rangle\end{pmatrix}=$$

$$=\begin{pmatrix}G^{<}_{p,\uparrow}\left(t,t'\right) & \bar{F}^{<}\left(t,t'\right)\\ F^{<}\left(t,t'\right) & G^{<}_{-p,\downarrow}\left(t,t'\right)\end{pmatrix},$$

that of course is related to:

$$\bar{\Delta}^{<}_{ab}\left(t,t'\right)=\frac{i}{N_s}\sum_p\begin{pmatrix}V^{a*}_{p,\uparrow} & 0\\ 0 & V^{a}_{-p,\downarrow}\end{pmatrix}K^{<}\left(t,t'\right)\begin{pmatrix}V^{b}_{p,\uparrow} & 0\\ 0 & V^{b*}_{-p,\downarrow}\end{pmatrix}.$$

An analogous definition can be applied for all of them. We can explicitly write all the 11 and the 21 components in the Nambu space:

$$G^{<}_{p,\uparrow}\left(t,t'\right)=\frac{i}{1+e^{\beta E_p}}\left[\cos^2\left(\theta_p\right)e^{-i(t-t')E_p}+\sin^2\left(\theta_p\right)e^{[\beta+i(t-t')]E_p}\right],$$

$$G^{>}_{p,\uparrow}\left(t,t'\right)=-\frac{i}{1+e^{\beta E_p}}\left[\cos^2\left(\theta_p\right)e^{[\beta-i(t-t')]E_p}+\sin^2\left(\theta_p\right)e^{i(t-t')E_p}\right],$$

$$G^{R}_{p,\uparrow}\left(t,t'\right)=-i\theta\left(t-t'\right)\left[\cos^2\left(\theta_p\right)e^{-i(t-t')E_p}+\sin^2\left(\theta_p\right)e^{i(t-t')E_p}\right],$$

$$G^{\urcorner}_{p,\uparrow}\left(t,\tau'\right)=\frac{i}{1+e^{\beta E_p}}\left[\cos^2\left(\theta_p\right)e^{-(it-\tau')E_p}+\sin^2\left(\theta_p\right)e^{(\beta+it-\tau')E_p}\right],$$

$$G^{\ulcorner}_{p,\uparrow}\left(\tau,t'\right)=-\frac{i}{1+e^{\beta E_p}}\left[\cos^2\left(\theta_p\right)e^{(\beta+it'-\tau)E_p}+\sin^2\left(\theta_p\right)e^{(\tau-it')E_p}\right],$$

$$\begin{aligned}
G^{M}_{p,\uparrow}(\tau) &= -\frac{\theta(\tau)}{1+e^{\beta E_p}}\left[\cos^2(\theta_p)\, e^{(\beta-\tau)E_p} + \sin^2(\theta_p)\, e^{\tau E_p}\right] + \\
&\quad + \frac{\theta(-\tau)}{1+e^{\beta E_p}}\left[\cos^2(\theta_p)\, e^{-\tau E_p} + \sin^2(\theta_p)\, e^{(\beta+\tau)E_p}\right] , \\
F^{<}\left(t,t'\right) &= i\frac{e^{2i\phi}\sin(\theta_p)\cos(\theta_p)}{1+e^{\beta E_p}}\left[e^{[\beta+i(t-t')]E_p} - e^{-i(t-t')E_p}\right] , \\
F^{>}\left(t,t'\right) &= i\frac{e^{-2i\phi}\sin(\theta_p)\cos(\theta_p)}{1+e^{\beta E_p}}\left[e^{[\beta-i(t-t')]E_p} - e^{i(t-t')E_p}\right] , \\
F^{R}\left(t,t'\right) &= \theta\left(t-t'\right) e^{2i\phi}\sin(2\theta_p)\sin\left(\left(t-t'\right)E_p\right) \\
F^{\neg}\left(t,\tau'\right) &= i\frac{e^{2i\phi}\sin(\theta_p)\cos(\theta_p)}{1+e^{\beta E_p}}\left[e^{(\beta+it-\tau')E_p} - e^{-(it-\tau')E_p}\right] , \\
F^{\ulcorner}\left(\tau,t'\right) &= i\frac{e^{-2i\phi}\sin(\theta_p)\cos(\theta_p)}{1+e^{\beta E_p}}\left[e^{(\tau-it')E_p} - e^{(it'-\tau+\beta)E_p}\right] , \\
F^{M}(\tau) &= -\frac{\sin(\theta_p)\cos(\theta_p)}{1+e^{\beta E_p}}\left(e^{-\tau E_p} - e^{(\tau+\beta)E_p}\right)\left(\theta(\tau)\, e^{-2i\phi} + \theta(-\tau)\, e^{2i\phi}\right) .
\end{aligned}$$

From those expressions we can obtain the complete matrix, since the following relations hold:

$$\begin{aligned}
G^{<}_{-p,\downarrow}\left(t,t'\right) &= -G^{>}_{p,\uparrow}\left(t',t\right) = \left[G^{>}_{p,\uparrow}\left(t,t'\right)\right]^{*} = \begin{cases} -G^{<}_{p,\uparrow}(t',t) - G^{R}_{p,\uparrow}(t',t), & t'>t \\ \left[G^{<}_{p,\uparrow}(t,t')\right]^{*} + \left[G^{R}_{p,\uparrow}(t,t')\right]^{*}, & t>t' \end{cases} \\
\bar{F}^{<}\left(t,t'\right) &= -\left[F^{<}\left(t',t\right)\right]^{*} , \\
G^{>}_{-p,\downarrow}\left(t,t'\right) &= -G^{<}_{p,\uparrow}\left(t',t\right) = \left[G^{<}_{p,\uparrow}\left(t,t'\right)\right]^{*} = \begin{cases} -G^{<}_{p,\uparrow}(t',t) - G^{R}_{p,\uparrow}(t',t), & t'<t \\ \left[G^{<}_{p,\uparrow}(t,t')\right]^{*} + \left[G^{R}_{p,\uparrow}(t,t')\right]^{*}, & t<t' \end{cases} \\
\bar{F}^{>}\left(t,t'\right) &= -\left[F^{>}\left(t',t\right)\right]^{*} , \\
G^{R}_{-p,\downarrow}\left(t,t'\right) &= -\left[G^{R}_{p,\uparrow}\left(t,t'\right)\right]^{*} , \\
\bar{F}^{R}\left(t,t'\right) &= \left[F^{R}\left(t,t'\right)\right]^{*} , \\
G^{\neg}_{-p,\downarrow}\left(t,\tau'\right) &= -G^{\ulcorner}_{p,\uparrow}\left(\tau',t\right) = -\left[G^{\neg}_{p,\uparrow}\left(t,\beta-\tau'\right)\right]^{*} , \\
\bar{F}^{\neg}\left(t,\tau'\right) &= \left[F^{\neg}\left(t,\beta-\tau'\right)\right]^{*} , \\
G^{\ulcorner}_{-p,\downarrow}\left(\tau,t'\right) &= -G^{\neg}_{p,\uparrow}\left(t',\tau\right) = -\left[G^{\ulcorner}_{p,\uparrow}\left(\beta-\tau,t'\right)\right]^{*} , \\
\bar{F}^{\ulcorner}\left(\tau,t'\right) &= \left[F^{\ulcorner}\left(\beta-\tau,t'\right)\right]^{*} , \\
G^{M}_{-p,\downarrow}(\tau) &= G^{M}_{p,\uparrow}(\beta-\tau) \\
\bar{F}^{M}(\tau) &= \left[F^{M}(\tau)\right]^{*} .
\end{aligned}$$

Langreth rules

We want to consider the real time components of Eq. (6.36). The only part that is not straightforward to be projected is

$$\hat{C}\left(z,z'\right)=\int_C dz_1 \hat{S}_{NCA}\left(z,z_1\right)\hat{R}\left(z_1,z'\right) \ .$$

By taking the greater component and by reminding that $\tilde{t}$ was defined in Fig. B.1 we obtain:

$$\begin{aligned}
&\hat{C}^{>}\left(t,t'\right)=\hat{C}\left(t^{+},t'^{-}\right)=\int_{t'^{-}}^{t^{+}} dz_1 \hat{S}_{NCA}\left(t^{+},z_1\right)\hat{R}\left(z_1,t'^{-}\right)=\\
&=\int_{t'^{-}}^{\tilde{t}} dz_1 \hat{S}_{NCA}\left(t^{+},z_1\right)\hat{R}\left(z_1,t'^{-}\right)+\int_{\tilde{t}}^{t^{+}} dz_1 \hat{S}_{NCA}\left(t^{+},z_1\right)\hat{R}\left(z_1,t'^{-}\right)=\\
&=\int_{t'^{-}}^{\tilde{t}} dt_1^{-} \hat{S}_{NCA}\left(t^{+},t_1^{-}\right)\hat{R}\left(t_1^{-},t'^{-}\right)+\int_{\tilde{t}}^{t^{+}} dt_1^{+} \hat{S}_{NCA}\left(t^{+},t_1^{+}\right)\hat{R}\left(t_1^{+},t'^{-}\right)=\\
&=\int_{t'}^{\tilde{t}} dt_1 \left(\hat{S}_{NCA}\left(t,t_1\right)\right)_{21}\left(\hat{R}\left(t_1,t'\right)\right)_{11}+\int_{\tilde{t}}^{t} dt_1 \left(\hat{S}_{NCA}\left(t,t_1\right)\right)_{22}\left(\hat{R}\left(t_1,t'\right)\right)_{21} \ .
\end{aligned}$$

Since we know that, for the generic function of two times $A\left(t,t'\right)$:

$$\begin{aligned}
\left(\hat{A}\left(t,t'\right)\right)_{11}&=\theta\left(t-t'\right)\left(\hat{A}\left(t,t'\right)\right)_{21}+\theta\left(t'-t\right)\left(\hat{A}\left(t,t'\right)\right)_{12} \ ,\\
\left(\hat{A}\left(t,t'\right)\right)_{22}&=\theta\left(t-t'\right)\left(\hat{A}\left(t,t'\right)\right)_{12}+\theta\left(t'-t\right)\left(\hat{A}\left(t,t'\right)\right)_{21} \ ,
\end{aligned}$$

we arrive at the expression

$$\begin{aligned}
&\hat{C}^{>}\left(t,t'\right)=\int_{t'}^{\tilde{t}} dt_1 \left(\hat{S}_{NCA}\left(t,t_1\right)\right)_{21}\left(\hat{R}\left(t_1,t'\right)\right)_{21}+\int_{\tilde{t}}^{t} dt_1 \left(\hat{S}_{NCA}\left(t,t_1\right)\right)_{21}\left(\hat{R}\left(t_1,t'\right)\right)_{21}=\\
&=\int_{t'}^{t} dt_1 \left(\hat{S}_{NCA}\left(t,t_1\right)\right)_{21}\left(\hat{R}\left(t_1,t'\right)\right)_{21}=\int_{t'}^{t} dt_1 \hat{S}_{NCA}^{>}\left(t,t_1\right)\hat{R}^{>}\left(t_1,t'\right) \ ,
\end{aligned}$$

where:

$$\begin{aligned}
&\hat{S}_{NCA}^{>}\left(t,t_1\right)=\hat{S}_{NCA}\left(t^{+},t_1^{-}\right)=\\
&=i\sum_{a,b}\left[\hat{\Psi}_a^{t}\left(1_{2\times2}\otimes\hat{R}^{>}\left(t,t_1\right)\right)\left(\bar{\Delta}_{b,a}^{t}\left(t_1,t\right)\right)^{<}\left(\hat{\Psi}_b^{\dagger}\right)^{t}-\hat{\Psi}_a^{\dagger}\left(1_{2\times2}\otimes\hat{R}^{>}\left(t,t_1\right)\right)\bar{\Delta}_{a,b}^{>}\left(t,t_1\right)\hat{\Psi}_b\right] \ .
\end{aligned}$$

At the end we can write

$$i\partial_t\hat{R}^{>}\left(t,t'\right)=\hat{H}_{imp}\left(t\right)\hat{R}^{>}\left(t,t'\right)+\int_{t'}^{t} dt_1 \hat{S}_{NCA}^{>}\left(t,t_1\right)\hat{R}^{>}\left(t_1,t'\right) \ .$$

In the same way we write the other components of the dynamical equations. By considering firstly the self energy, we obtain:

$$
\begin{aligned}
\hat{S}^{<}_{NCA}(t,t_1) &= i\sum_{a,b}[\hat{\Psi}^{t}_{a}\left(1_{2\times 2}\otimes \hat{R}^{<}(t,t_1)\right)\left(\bar{\Delta}^{t}_{b,a}(t_1,t)\right)^{>}\left(\hat{\Psi}^{\dagger}_{b}\right)^{t} \\
&\quad -\hat{\Psi}^{\dagger}_{a}\left(1_{2\times 2}\otimes \hat{R}^{<}(t,t_1)\right)\bar{\Delta}^{<}_{a,b}(t,t_1)\hat{\Psi}_{b}]\,, \\
\hat{S}^{R}_{NCA}(t,t_1) &= \theta(t-t_1)\left[\hat{S}^{>}_{NCA}(t,t_1)-\hat{S}^{<}_{NCA}(t,t_1)\right]\ , \\
\hat{S}^{\urcorner}_{NCA}(t,\tau_1) &= i\sum_{a,b}[\hat{\Psi}^{t}_{a}\left(1_{2\times 2}\otimes \hat{R}^{\urcorner}(t,\tau_1)\right)\left(\bar{\Delta}^{t}_{b,a}(\tau_1,t)\right)^{\ulcorner}\left(\hat{\Psi}^{\dagger}_{b}\right)^{t} \\
&\quad -\hat{\Psi}^{\dagger}_{a}\left(1_{2\times 2}\otimes \hat{R}^{\urcorner}(t,\tau_1)\right)\bar{\Delta}^{\urcorner}_{a,b}(t,\tau_1)\hat{\Psi}_{b}]\,, \\
\hat{S}^{\ulcorner}_{NCA}(\tau,t_1) &= i\sum_{a,b}[\hat{\Psi}^{t}_{a}\left(1_{2\times 2}\otimes \hat{R}^{\ulcorner}(\tau,t_1)\right)\left(\bar{\Delta}^{t}_{b,a}(t_1,\tau)\right)^{\urcorner}\left(\hat{\Psi}^{\dagger}_{b}\right)^{t} \\
&\quad -\hat{\Psi}^{\dagger}_{a}\left(1_{2\times 2}\otimes \hat{R}^{\ulcorner}(\tau,t_1)\right)\bar{\Delta}^{\ulcorner}_{a,b}(\tau,t_1)\hat{\Psi}_{b}]\,, \\
\hat{S}^{M}_{NCA}(\tau) &= \sum_{a,b}[\hat{\Psi}^{t}_{a}\left(1_{2\times 2}\otimes R^{M}(\tau)\right)\left(\bar{\Delta}^{t}_{b,a}(-\tau)\right)^{M}\left(\hat{\Psi}^{\dagger}_{b}\right)^{t} \\
&\quad -\hat{\Psi}^{\dagger}_{a}\left(1_{2\times 2}\otimes R^{M}(\tau)\right)\bar{\Delta}^{M}_{a,b}(\tau)\hat{\Psi}_{b}]\,,
\end{aligned}
$$

so that:

$$
\begin{aligned}
& i\partial_t\hat{R}^{<}\left(t,t'\right) = \hat{H}_{imp}(t)\hat{R}^{<}\left(t,t'\right)+\int_{t_0}^{t}dt_1\hat{S}^{>}_{NCA}(t,t_1)\hat{R}^{<}\left(t_1,t'\right)+ \\
& -\int_{t_0}^{t'}dt_1\hat{S}^{<}_{NCA}(t,t_1)\hat{R}^{>}\left(t_1,t'\right)-i\int_{it_0}^{it_0+\beta}d\tau_1\hat{S}^{\urcorner}_{NCA}(t,\tau_1)\hat{R}^{\ulcorner}\left(\tau_1,t'\right)\ , \\
& i\partial_t\hat{R}^{R}\left(t,t'\right) = \hat{H}_{imp}(t)\hat{R}^{R}\left(t,t'\right)+\theta\left(t-t'\right)[\int_{t_0}^{t}dt_1\hat{S}^{>}_{NCA}(t,t_1)\left(\hat{R}^{>}\left(t_1,t'\right)-\hat{R}^{<}\left(t_1,t'\right)\right)+ \\
& +\int_{t_0}^{t'}dt_1\left(\hat{S}^{<}_{NCA}(t,t_1)-\hat{S}^{>}_{NCA}(t,t_1)\right)\hat{R}^{>}\left(t_1,t'\right)+i\int_{it_0}^{it_0+\beta}d\tau_1\hat{S}^{\urcorner}_{NCA}(t,\tau_1)\hat{R}^{\ulcorner}\left(\tau_1,t'\right)]\,, \\
& i\partial_t\hat{R}^{\urcorner}\left(t,\tau'\right) = \hat{H}_{imp}(t)\hat{R}^{\urcorner}\left(t,\tau'\right)+\int_{t_0}^{t}dt_1\hat{S}^{<}_{NCA}(t,t_1)\hat{R}^{\urcorner}\left(t_1,\tau'\right)+ \\
& +\int_{it_0+\tau'}^{it_0+\beta}d\tau_1\hat{S}^{\urcorner}_{NCA}(t,\tau_1)\hat{R}^{M}\left(\tau_1-\tau'\right)\ , \\
& \partial_\tau\hat{R}^{\ulcorner}\left(\tau,t'\right) = \hat{H}_{imp}(\tau)\hat{R}^{\ulcorner}\left(\tau,t'\right)-\int_{t_0}^{t'}dt_1\hat{S}^{\ulcorner}_{NCA}(\tau,t_1)\hat{R}^{>}\left(t_1,t'\right)+ \\
& +\int_{it_0}^{it_0+\tau}d\tau_1\hat{S}^{M}_{NCA}(\tau-\tau_1)\hat{R}^{\ulcorner}\left(\tau_1,t'\right)\ , \\
& \partial_\tau\hat{R}^{M}(\tau) = \hat{H}_{imp}(\tau)\hat{R}^{M}(\tau)+\int_{0}^{\tau}d\tau_1\hat{S}^{M}_{NCA}(\tau-\tau_1)\hat{R}^{M}(\tau_1)\ .
\end{aligned}
$$

In order to properly define those differential equations, we have to specify the initial conditions for the unknown functions. Particularly, we can start by solving the equations for the Matsubara or the greater components, since they do not involve any other components of the local propagator. We can write:

$$\begin{aligned}
&\hat{R}^{M}\left(0\right)=-1\\
&\hat{R}^{>}\left(t_0,t_0^-\right)=-i1\\
&\hat{R}^{<}\left(t_0,t_0^-\right)=i\hat{R}^{M}\left(\beta\right)\\
&\hat{R}^{R}\left(t_0,t_0^-\right)=-i\left[1+\hat{R}^{M}\left(\beta\right)\right]\\
&\hat{R}^{\urcorner}\left(t_0,\tau\right)=i\hat{R}^{M}\left(\beta-\tau\right)\\
&\hat{R}^{\ulcorner}\left(\tau,t_0\right)=i\hat{R}^{M}\left(\tau\right)
\end{aligned}$$

where 1 is a representation of the identity over the local Hilbert space of the problem.

Bibliography

[1] Andrea Cavagna and Irene Giardina. Bird flocks as condensed matter. *Annual Review of Condensed Matter Physics*, 5(1):183–207, 2014.

[2] D. J. T. Sumpter. The principles of collective animal behaviour. *Philosophical Transactions of the Royal Society B: Biological Sciences*, 361(1465):5–22, 2005.

[3] P. W. Anderson. More is different. *Science*, 177(4047):393–396, 1972.

[4] Murray Gell-Mann. *The Quark and the Jaguar: Adventures in the Simple and the Complex*. W. H. Freeman & Co., New York, NY, USA, 1995.

[5] Ig. Tamm. Über die quantentheorie der molekularen lichtzerstreuung in festen körpern. *Zeitschrift für Physik*, 60(5):345–363, May 1930.

[6] L Landau. On the theory of a Fermi liquid. *Soviet Physics JETP*, 3:920–925, 1957.

[7] J. Bardeen, L. N. Cooper, and J. R. Schrieffer. Theory of superconductivity. *Phys. Rev.*, 108:1175–1204, Dec 1957.

[8] N F Mott. The Basis of the Electron Theory of Metals, with Special Reference to the Transition Metals. *Proc. Phys. Soc. (London)*, A62:416–422, 1949.

[9] N. F. Mott. On the transition to metallic conduction in semiconductors. *Canadian Journal of Physics*, 34(12A):1356–1368, 1956.

[10] N. F. Mott. The transition to the metallic state. *The Philosophical Magazine: A Journal of Theoretical Experimental and Applied Physics*, 6(62):287–309, 1961.

[11] N F Mott. Metal-Insulator Transition. *Rev. Mod. Phys.*, 40(4):677–683, 1968.

[12] N. F. Mott. *Metal-insulator transitions*. Taylor and Francis ;Barnes and Noble Books London : New York, 1974.

[13] F. Bloch. Über die quantenmechanik der elektronen in kristallgittern. *Zeitschrift für Physik*, 52(7):555–600, Jul 1929.

[14] A. H. Wilson. The theory of electronic semi-conductors. *Proceedings of the Royal Society of London A: Mathematical, Physical and Engineering Sciences*, 133(822):458–491, 1931.

[15] A. H. Wilson. The theory of electronic semi-conductors. - ii. *Proceedings of the Royal Society of London A: Mathematical, Physical and Engineering Sciences*, 134(823):277–287, 1931.

[16] Maxwell F. Parsons, Anton Mazurenko, Christie S. Chiu, Geoffrey Ji, Daniel Greif, and Markus Greiner. Site-resolved measurement of the spin-correlation function in the fermi-hubbard model. *Science*, 353(6305):1253–1256, 2016.

[17] R. Jördens, N. Strohmaier, K. Günter, H. Moritz, and T. Esslinger. A mott insulator of fermionic atoms in an optical lattice. *Nature*, 455:204, Sep 2008.

[18] Christian Gross and Immanuel Bloch. Quantum simulations with ultracold atoms in optical lattices. *Science*, 357(6355):995–1001, 2017.

[19] M. Greiner, O. Mandel, T. Esslinger, T. W. Hänsch, and I. Bloch. Quantum phase transition from a superfluid to a mott insulator in a gas of ultracold atoms. *Nature*, 415:39, Jan 2002.

[20] Masatoshi Imada, Atsushi Fujimori, and Yoshinori Tokura. Metal-insulator transitions. *Rev. Mod. Phys.*, 70(4):1039–1263, 1998.

[21] Daniel I. Khomskii. *Transition Metal Compounds*. Cambridge University Press, 2014.

[22] J. Zhang and R.D. Averitt. Dynamics and control in complex transition metal oxides. *Annual Review of Materials Research*, 44(1):19–43, 2014.

[23] J.L. Smith and E.A. Kmetko. Magnetism or bonding: A nearly periodic table of transition elements. *Journal of the Less Common Metals*, 90(1):83 – 88, 1983.

[24] P.W. Anderson. Resonating valence bonds: A new kind of insulator? *Materials Research Bulletin*, 8(2):153 – 160, 1973.

[25] P. W. ANDERSON. The resonating valence bond state in la2cuo4 and superconductivity. *Science*, 235(4793):1196–1198, 1987.

[26] P. W. Anderson. New approach to the theory of superexchange interactions. *Phys. Rev.*, 115:2–13, Jul 1959.

[27] Naoto Tsuji and Philipp Werner. Nonequilibrium dynamical mean-field theory based on weak-coupling perturbation expansions: Application to dynamical symmetry breaking in the hubbard model. *Phys. Rev. B*, 88:165115, Oct 2013.

[28] H. Park, K. Haule, and G. Kotliar. Cluster dynamical mean field theory of the mott transition. *Phys. Rev. Lett.*, 101:186403, Oct 2008.

[29] Antoine Georges, Gabriel Kotliar, Werner Krauth, and Marcelo J. Rozenberg. Dynamical mean-field theory of strongly correlated fermion systems and the limit of infinite dimensions. *Rev. Mod. Phys.*, 68:13–125, Jan 1996.

[30] V. Eyert. vo_2: A novel view from band theory. *Phys. Rev. Lett.*, 107:016401, Jun 2011.

[31] Matteo Sandri, Massimo Capone, and Michele Fabrizio. Finite-temperature gutzwiller approximation and the phase diagram of a toy model for v_2o_3. *Phys. Rev. B*, 87:205108, May 2013.

[32] Akihisa Koga, Norio Kawakami, T. M. Rice, and Manfred Sigrist. Orbital-selective mott transitions in the degenerate hubbard model. *Phys. Rev. Lett.*, 92:216402, May 2004.

[33] Michel Ferrero, Federico Becca, Michele Fabrizio, and Massimo Capone. Dynamical behavior across the mott transition of two bands with different bandwidths. *Phys. Rev. B*, 72:205126, Nov 2005.

[34] Luca de' Medici, Antoine Georges, and Silke Biermann. Orbital-selective Mott transition in multiband systems: Slave-spin representation and dynamical mean-field theory. *Phys. Rev. B*, 72(20):205124, 2005.

[35] Eberhard Jakobi, Nils Blümer, and Peter van Dongen. Orbital-selective mott transitions in a doped two-band hubbard model with crystal field splitting. *Phys. Rev. B*, 87:205135, May 2013.

[36] E. A. Winograd and L. de' Medici. Hybridizing localized and itinerant electrons: A recipe for pseudogaps. *Phys. Rev. B*, 89:085127, Feb 2014.

[37] Luca de' Medici. Hund's coupling and its key role in tuning multiorbital correlations. *Phys. Rev. B*, 83:205112, May 2011.

[38] Tomoko Kita, Takuma Ohashi, and Norio Kawakami. Mott transition in three-orbital hubbard model with orbital splitting. *Phys. Rev. B*, 84:195130, Nov 2011.

[39] Yilin Wang, Li Huang, Liang Du, and Xi Dai. Doping-driven orbital-selective mott transition in multi-band hubbard models with crystal field splitting. *Chinese Physics B*, 25(3):037103, 2016.

[40] Luca de' Medici, S. R. Hassan, Massimo Capone, and Xi Dai. Orbital-selective mott transition out of band degeneracy lifting. *Phys. Rev. Lett.*, 102:126401, Mar 2009.

[41] Yashar Komijani and Gabriel Kotliar. Analytical slave-spin mean-field approach to orbital selective mott insulators. *Phys. Rev. B*, 96:125111, Sep 2017.

[42] Rong Yu and Qimiao Si. Orbital-selective mott phase in multiorbital models for iron pnictides and chalcogenides. *Phys. Rev. B*, 96:125110, Sep 2017.

[43] Shintaro Hoshino and Philipp Werner. Spontaneous orbital-selective mott transitions and the jahn-teller metal of A_3c_{60}. *Phys. Rev. Lett.*, 118:177002, Apr 2017.

[44] Li Huang, Yilin Wang, Lei Wang, and Philipp Werner. Detecting phase transitions and crossovers in hubbard models using the fidelity susceptibility. *Phys. Rev. B*, 94:235110, Dec 2016.

[45] Philipp Werner, Emanuel Gull, and Andrew J. Millis. Metal-insulator phase diagram and orbital selectivity in three-orbital models with rotationally invariant hund coupling. *Phys. Rev. B*, 79:115119, Mar 2009.

[46] K. Bouadim, G. G. Batrouni, and R. T. Scalettar. Determinant quantum monte carlo study of the orbitally selective mott transition. *Phys. Rev. Lett.*, 102:226402, Jun 2009.

[47] Luca F Tocchio, Federico Arrigoni, Sandro Sorella, and Federico Becca. Assessing the orbital selective mott transition with variational wave functions. *Journal of Physics: Condensed Matter*, 28(10):105602, 2016.

[48] V.I. Anisimov, I.A. Nekrasov, D.E. Kondakov, T.M. Rice, and M. Sigrist. Orbital-selective Mott-insulator transition in $\mathrm{Ca}_{2-x}\mathrm{Sr}_x\mathrm{RuO}_4$. *The European Physical Journal B - Condensed Matter and Complex Systems*, 25(2):191–201, Jan 2002.

[49] S. Nakatsuji and Y. Maeno. Quasi-two-dimensional mott transition system $\mathrm{ca}_{2-x}\mathrm{sr}_x\mathrm{ruo}_4$. *Phys. Rev. Lett.*, 84:2666–2669, Mar 2000.

[50] Luca de' Medici, Jernej Mravlje, and Antoine Georges. Janus-Faced Influence of Hund's Rule Coupling in Strongly Correlated Materials. *Phys. Rev. Lett.*, 107(25):256401, 2011.

[51] Antoine Georges, Luca de' Medici, and Jernej Mravlje. Strong correlations from hund's coupling. *Annual Review of Condensed Matter Physics*, 4(1):137–178, 2013.

[52] Luca de' Medici, Gianluca Giovannetti, and Massimo Capone. Selective Mott physics as a key to iron superconductors. *Phys. Rev. Lett.*, 112:177001, Apr 2014.

[53] G. Jackeli and G. Khaliullin. Mott insulators in the strong spin-orbit coupling limit: From heisenberg to a quantum compass and kitaev models. *Phys. Rev. Lett.*, 102:017205, Jan 2009.

[54] Jeffrey G. Rau, Eric Kin-Ho Lee, and Hae-Young Kee. Spin-orbit physics giving rise to novel phases in correlated systems: Iridates and related materials. *Annual Review of Condensed Matter Physics*, 7(1):195–221, 2016.

[55] Z. P. Yin, K. Haule, and G. Kotliar. Kinetic frustration and the nature of the magnetic and paramagnetic states in iron pnictides and iron chalcogenides. *Nature Materials*, 10:932 EP –, 09 2011.

[56] E. Bascones, B. Valenzuela, and M. J. Calderón. Orbital differentiation and the role of orbital ordering in the magnetic state of fe superconductors. *Phys. Rev. B*, 86:174508, Nov 2012.

[57] Nicola Lanatà, Yongxin Yao, Xiaoyu Deng, Vladimir Dobrosavljević, and Gabriel Kotliar. Slave boson theory of orbital differentiation with crystal field effects: Application to uo_2. *Phys. Rev. Lett.*, 118:126401, Mar 2017.

[58] Satoshi Miyashita, Yasufumi Yamashita, Kenji Yonemitsu, Akihisa Koga, and Norio Kawakami. Mott insulating state in a quarter-filled two-orbital hubbard chain with different bandwidths. *Journal of Physics: Conference Series*, 150(4):042128, 2009.

[59] K. I. Kugel and D. I. Khomskii. Crystal-structure and magnetic properties of substances with orbital degeneracy. *Zh. Eksp. Teor. Fiz*, 64:1429–1439, Apr 1973.

[60] Kliment I Kugel' and D I Khomskiĭ. The jahn-teller effect and magnetism: transition metal compounds. *Soviet Physics Uspekhi*, 25(4):231, 1982.

[61] L.-M. Duan, E. Demler, and M. D. Lukin. Controlling spin exchange interactions of ultracold atoms in optical lattices. *Phys. Rev. Lett.*, 91:090402, Aug 2003.

[62] D I Khomskii. Role of orbitals in the physics of correlated electron systems. *Physica Scripta*, 72(5):CC8, 2005.

[63] R Z Levitin and A S Markosyan. Itinerant metamagnetism. *Soviet Physics Uspekhi*, 31(8):730, 1988.

[64] Michael E. Fisher and David R. Nelson. Spin flop, supersolids, and bicritical and tetracritical points. *Phys. Rev. Lett.*, 32:1350–1353, Jun 1974.

[65] John B. Goodenough. Theory of the role of covalence in the perovskite-type manganites $[\mathrm{La}, m(\mathrm{II})]\mathrm{Mno}_3$. *Phys. Rev.*, 100:564–573, Oct 1955.

[66] Junjiro Kanamori. Superexchange interaction and symmetry properties of electron orbitals. *Journal of Physics and Chemistry of Solids*, 10(2):87 – 98, 1959.

[67] F. J. Morin. Oxides which show a metal-to-insulator transition at the neel temperature. *Phys. Rev. Lett.*, 3:34–36, Jul 1959.

[68] A. X. Gray, M. C. Hoffmann, J. Jeong, N. P. Aetukuri, D. Zhu, H. Y. Hwang, N. C. Brandt, H. Wen, A. J. Sternbach, S. Bonetti, A. H. Reid, R. Kukreja, C. Graves, T. Wang, P. Granitzka, Z. Chen, D. J. Higley, T. Chase, E. Jal, E. Abreu, M. K. Liu, T.-C. Weng, D. Sokaras, D. Nordlund, M. Chollet, R. Alonso-Mori, H. Lemke, J. M. Glownia, M. Trigo, Y. Zhu, H. Ohldag, J. W. Freeland, M. G. Samant, J. Berakdar, R. D. Averitt, K. A. Nelson, S. S. P. Parkin, and H. A. Dürr. Ultrafast terahertz field control of electronic and structural interactions in vanadium dioxide. *Phys. Rev. B*, 98:045104, Jul 2018.

[69] S. Biermann, A. Poteryaev, A. I. Lichtenstein, and A. Georges. Dynamical singlets and correlation-assisted peierls transition in vo_2. *Phys. Rev. Lett.*, 94:026404, Jan 2005.

[70] W. H. Brito, M. C. O. Aguiar, K. Haule, and G. Kotliar. Metal-insulator transition in vo_2: A $\mathrm{DFT}+\mathrm{DMFT}$ perspective. *Phys. Rev. Lett.*, 117:056402, Jul 2016.

[71] O. Nájera, M. Civelli, V. Dobrosavljević, and M. J. Rozenberg. Resolving the vo_2 controversy: Mott mechanism dominates the insulator-to-metal transition. *Phys. Rev. B*, 95:035113, Jan 2017.

[72] Dušan Plašienka, Roman Martoňák, and Marcus C. Newton. Ab initio molecular dynamics study of the structural and electronic transition in vo_2. *Phys. Rev. B*, 96:054111, Aug 2017.

[73] O. Nájera, M. Civelli, V. Dobrosavljević, and M. J. Rozenberg. Multiple crossovers and coherent states in a mott-peierls insulator. *Phys. Rev. B*, 97:045108, Jan 2018.

[74] J. H. Park, J. M. Coy, T. S. Kasirga, C. Huang, Z. Fei, S. Hunter, and D. H. Cobden. Measurement of a solid-state triple point at the metal-insulator transition in vo_2. *Nature*, 500:431, Aug 2013.

[75] Y. Chen, S. Zhang, F. Ke, C. Ko, S. Lee, K. Liu, B. Chen, J. W. Ager, R. Jeanloz, V. Eyert, and J. Wu. Pressure-temperature phase diagram of vanadium dioxide. *Nano Letters*, 17(4):2512–2516, 2017.

[76] Weiss Alarich. John b. goodenough: Magnetism and the chemical bond. interscience publishers. new york, london 1963. 393 seiten, 89 abbildungen. preis: Dm 95 s. *Berichte der Bunsengesellschaft für physikalische Chemie*, 68(10):996–996, 1964.

[77] G. Villeneuve and P. Hagenmuller. *Metal-Insulator Transitions in Pure and Doped VO_2*, pages 39–52. Springer US, Boston, MA, 1985.

[78] C. N. Berglund and H. J. Guggenheim. Electronic properties of vo_2 near the semiconductor-metal transition. *Phys. Rev.*, 185:1022–1033, Sep 1969.

[79] Y-R Jo, M-W Kim, and B-J Kim. Direct correlation of structural and electrical properties of electron-doped individual vo_2 nanowires on devised tem grids. *Nanotechnology*, 27(43):435704, 2016.

[80] Peter Baum, Ding-Shyue Yang, and Ahmed H. Zewail. 4d visualization of transitional structures in phase transformations by electron diffraction. *Science*, 318(5851):788–792, 2007.

[81] John B. Goodenough. The two components of the crystallographic transition in vo2. *Journal of Solid State Chemistry*, 3(4):490 – 500, 1971.

[82] A. Zylbersztejn and N. F. Mott. Metal-insulator transition in vanadium dioxide. *Phys. Rev. B*, 11:4383–4395, Jun 1975.

[83] Sangwook Lee, Kedar Hippalgaonkar, Fan Yang, Jiawang Hong, Changhyun Ko, Joonki Suh, Kai Liu, Kevin Wang, Jeffrey J. Urban, Xiang Zhang, Chris Dames, Sean A. Hartnoll, Olivier Delaire, and Junqiao Wu. Anomalously low electronic thermal conductivity in metallic vanadium dioxide. *Science*, 355(6323):371–374, 2017.

[84] M. M. Qazilbash, M. Brehm, Byung-Gyu Chae, P.-C. Ho, G. O. Andreev, Bong-Jun Kim, Sun Jin Yun, A. V. Balatsky, M. B. Maple, F. Keilmann, Hyun-Tak Kim, and D. N. Basov. Mott transition in vo_2 revealed by infrared spectroscopy and nano-imaging. *Science*, 318(5857):1750–1753, 2007.

[85] C. N. Berglund and A. Jayaraman. Hydrostatic-pressure dependence of the electronic properties of vo_2 near the semiconductor-metal transition temperature. *Phys. Rev.*, 185:1034–1039, Sep 1969.

[86] M. M. Qazilbash, A. A. Schafgans, K. S. Burch, S. J. Yun, B. G. Chae, B. J. Kim, H. T. Kim, and D. N. Basov. Electrodynamics of the vanadium oxides Vo_2 and v_2o_3. *Phys. Rev. B*, 77:115121, Mar 2008.

[87] Hal Tasaki. From nagaoka's ferromagnetism to flat-band ferromagnetism and beyondan introduction to ferromagnetism in the hubbard model. *Progress of Theoretical Physics*, 99(4):489–548, 1998.

[88] H. Tasaki. The Hubbard Model: Introduction and Selected Rigorous Results. *eprint arXiv:cond-mat/9512169*, dec 1995.

[89] Martin C. Gutzwiller. Effect of correlation on the ferromagnetism of transition metals. *Phys. Rev. Lett.*, 10:159–162, Mar 1963.

[90] Junjiro Kanamori. Electron correlation and ferromagnetism of transition metals. *Progress of Theoretical Physics*, 30(3):275–289, 1963.

[91] J. Hubbard. Electron correlations in narrow energy bands. *Proceedings of the Royal Society of London A: Mathematical, Physical and Engineering Sciences*, 276(1365):238–257, 1963.

[92] Elliott H. Lieb and F. Y. Wu. Absence of mott transition in an exact solution of the short-range, one-band model in one dimension. *Phys. Rev. Lett.*, 20:1445–1448, Jun 1968.

[93] M Mezard, G Parisi, and M Virasoro. *Spin Glass Theory and Beyond.* WORLD SCIENTIFIC, 1986.

[94] J.W. Negele and H. Orland. *Quantum many-particle systems.* Frontiers in physics. Addison-Wesley Pub. Co., 1988.

[95] Laleh Farhang Matin. Exactly solvable reaction diffusion models on a bethe lattice through the empty-interval method. *Journal of Theoretical and Applied Physics*, 9(2):93–98, Jun 2015.

[96] Walter Metzner and Dieter Vollhardt. Correlated lattice fermions in $d = \infty$ dimensions. *Phys. Rev. Lett.*, 62:324–327, Jan 1989.

[97] Walter Metzner. Variational theory for correlated lattice fermions in high dimensions. *Zeitschrift für Physik B Condensed Matter*, 77(2):253–266, Jun 1989.

[98] A.L. Fetter and J.D. Walecka. *Quantum Theory of Many-particle Systems.* Dover Books on Physics. Dover Publications, 2003.

[99] Michel Caffarel and Werner Krauth. Exact diagonalization approach to correlated fermions in infinite dimensions: Mott transition and superconductivity. *Physical review letters*, 72(10):1545–1548, 1994.

[100] Cornelius Lanczos. An iteration method for the solution of the eigenvalue problem of linear differential and integral operators. *J. Res. Natl. Bur. Stand. B*, 45:255–282, 1950.

[101] M Capone, L de' Medici, and A Georges. Solving the dynamical mean-field theory at very low temperatures using the Lanczos exact diagonalization. *Phys. Rev. B*, 76(24):245116, 2007.

[102] Markus Aichhorn, Maria Daghofer, Hans Evertz, and Wolfgang von der Linden. Low-temperature Lanczos method for strongly correlated systems. *Physical Review B*, 67(16):161103, 2003.

[103] Eduardo R Gagliano, Elbio Dagotto, Adriana Moreo, and Francisco C Alcaraz. Correlation functions of the antiferromagnetic Heisenberg model using a modified Lanczos method. *Phys. Rev. B*, 34(3):1677–1682, 1986.

[104] Matthias Vojta. Orbital-selective Mott transitions: Heavy fermions and beyond. *Journal of Low Temperature Physics*, 161(1):203–232, Oct 2010.

[105] Junjiro Kanamori. Electron correlation and ferromagnetism of transition metals. *Progress of Theoretical Physics*, 30(3):275–289, 1963.

[106] Philippe Corboz, Andreas M. Läuchli, Karlo Penc, Matthias Troyer, and Frédéric Mila. Simultaneous dimerization and su(4) symmetry breaking of 4-color fermions on the square lattice. *Phys. Rev. Lett.*, 107:215301, Nov 2011.

[107] Matteo Sandri and Michele Fabrizio. Nonequilibrium gap collapse near a first-order mott transition. *Phys. Rev. B*, 91:115102, Mar 2015.

[108] J. E. Hirsch. Two-dimensional hubbard model: Numerical simulation study. *Phys. Rev. B*, 31:4403–4419, Apr 1985.

[109] Tung-Lam Dao, Michel Ferrero, Pablo S. Cornaglia, and Massimo Capone. Mott transition of fermionic mixtures with mass imbalance in optical lattices. *Phys. Rev. A*, 85:013606, Jan 2012.

[110] I. M. Lifshitz. Anomalies of electron characteristics of a metal in the high pressure region. *Sov. Phys. JETP*, 11:1130, Nov 1960.

[111] K Binder. Theory of first-order phase transitions. *Reports on Progress in Physics*, 50(7):783, 1987.

[112] Robert B. Griffiths. Thermodynamics near the two-fluid critical mixing point in he^3 - he^4. *Phys. Rev. Lett.*, 24:715–717, Mar 1970.

[113] L. M. Falicov and J. C. Kimball. Simple model for semiconductor-metal transitions: Smb$_6$ and transition-metal oxides. *Phys. Rev. Lett.*, 22:997–999, May 1969.

[114] Alexander I. Poteryaev, Jan M. Tomczak, Silke Biermann, Antoine Georges, Alexander I. Lichtenstein, Alexey N. Rubtsov, Tanusri Saha-Dasgupta, and Ole K. Andersen. Enhanced crystal-field splitting and orbital-selective coherence induced by strong correlations in v$_2$o$_3$. *Phys. Rev. B*, 76:085127, Aug 2007.

[115] L. Paolasini, R. Caciuffo, A. Sollier, P. Ghigna, and M. Altarelli. Coupling between spin and orbital degrees of freedom in kcuf$_3$. *Phys. Rev. Lett.*, 88:106403, Feb 2002.

[116] E. Pavarini, E. Koch, and A. I. Lichtenstein. Mechanism for orbital ordering in kcuf$_3$. *Phys. Rev. Lett.*, 101:266405, Dec 2008.

[117] Zheng Yang, Changhyun Ko, and Shriram Ramanathan. Oxide electronics utilizing ultrafast metal-insulator transitions. *Annual Review of Materials Research*, 41(1):337–367, 2011.

[118] H. S. Choe, J. Suh, C. Ko, K. Dong, S. Lee, J. Park, Y. Lee, K. Wang, and J. Wu. Enhancing modulation of thermal conduction in vanadium dioxide thin film by nanostructured nanogaps. *Scientific Reports*, 7:7131, Aug 2017.

[119] C. H. Ahn, A. Bhattacharya, M. Di Ventra, J. N. Eckstein, C. Daniel Frisbie, M. E. Gershenson, A. M. Goldman, I. H. Inoue, J. Mannhart, Andrew J. Millis, Alberto F. Morpurgo, Douglas Natelson, and Jean-Marc Triscone. Electrostatic modification of novel materials. *Rev. Mod. Phys.*, 78:1185–1212, Nov 2006.

[120] A. S. Barker, H. W. Verleur, and H. J. Guggenheim. Infrared optical properties of vanadium dioxide above and below the transition temperature. *Phys. Rev. Lett.*, 17:1286–1289, Dec 1966.

[121] Philipp Scheiderer, Matthias Schmitt, Judith Gabel, Michael Zapf, Martin Stübinger, Philipp Schütz, Lenart Dudy, Christoph Schlueter, Tien-Lin Lee, Michael Sing, and Ralph Claessen. Tailoring materials for mottronics: Excess oxygen doping of a prototypical mott insulator. *Advanced Materials*, 30(25):1706708, 2018.

[122] Pablo Stoliar, Laurent Cario, Etiene Janod, Benoit Corraze, Catherine Guillot-Deudon, Sabrina Salmon-Bourmand, Vincent Guiot, Julien Tranchant, and Marcelo Rozenberg. Universal electric-field-driven resistive transition in narrow-gap mott insulators. *Advanced Materials*, 25(23):3222–3226, 2013.

[123] Isao H. Inoue and Marcelo J. Rozenberg. Taming the mott transition for a novel mott transistor. *Advanced Functional Materials*, 18(16):2289–2292, 2008.

[124] N. B. Aetukuri, A. X. Gray, M. Drouard, M. Cossale, L. Gao, A. H. Reid, R. Kukreja, H. Ohldag, C. A. Jenkins, E. Arenholz, K. P. Roche, H. A. Dürr, M. G. Samant, and S. S. P. Parkin. Control of the metal-insulator transition in vanadium dioxide by modifying orbital occupancy. *Nature Physics*, 9:661, Sep 2013.

[125] Changhyun Ko and Shriram Ramanathan. Observation of electric field-assisted phase transition in thin film vanadium oxide in a metal-oxide-semiconductor device geometry. *Applied Physics Letters*, 93(25):252101, 2008.

[126] P. P. Boriskov, A. A. Velichko, A. L. Pergament, G. B. Stefanovich, and D. G. Stefanovich. The effect of electric field on metal-insulator phase transition in vanadium dioxide. *Technical Physics Letters*, 28(5):406–408, May 2002.

[127] M. Nakano, K. Shibuya, D. Okuyama, T. Hatano, S. Ono, M. Kawasaki, Y. Iwasa, and Y. Tokura. Collective bulk carrier delocalization driven by electrostatic surface charge accumulation. *Nature*, 487:459, Jul 2012.

[128] D. Okuyama, M. Nakano, S. Takeshita, H. Ohsumi, S. Tardif, K. Shibuya, T. Hatano, H. Yumoto, T. Koyama, H. Ohashi, M. Takata, M. Kawasaki, T. Arima, Y. Tokura, and Y. Iwasa. Gate-tunable gigantic lattice deformation in vo2. *Applied Physics Letters*, 104(2):023507, 2014.

[129] V. Eyert. The metal-insulator transitions of vo_2: A band theoretical approach. *Annalen der Physik*, 11(9):650–704, Jul 2002.

[130] N. F. Mott and L. Friedman. Metal-insulator transitions in vo_2, $\mathrm{ti}_2\mathrm{o}_3$ and $\mathrm{ti}_{2-x}\mathrm{v}_x\mathrm{o}_3$. *The Philosophical Magazine: A Journal of Theoretical Experimental and Applied Physics*, 30:389–402, Aug 1974.

[131] T. J. Huffman, C. Hendriks, E. J. Walter, Joonseok Yoon, Honglyoul Ju, R. Smith, G. L. Carr, H. Krakauer, and M. M. Qazilbash. Insulating phases of vanadium dioxide are mott-hubbard insulators. *Phys. Rev. B*, 95:075125, Feb 2017.

[132] W F Brinkman and T M Rice. Application of Gutzwiller's Variational Method to the Metal-Insulator Transition. *Phys. Rev. B*, 2(10):4302–4304, 1970.

[133] Hyun-Tak Kim, Byung-Gyu Chae, Doo-Hyeb Youn, Sung-Lyul Maeng, Gyungock Kim, Kwang-Yong Kang, and Yong-Sik Lim. Mechanism and observation of mott transition in vo 2 -based two- and three-terminal devices. *New Journal of Physics*, 6(1):52, 2004.

[134] Hiromu Sasaki and Akinori Watanabe. A new growing method for vo2 single crystals. *Journal of the Physical Society of Japan*, 19(9):1748–1748, 1964.

[135] Larry A. Ladd and William Paul. Optical and transport properties of high quality crystals of v2o4 near the metallic transition temperature. *Solid State Communications*, 7(4):425 – 428, 1969.

[136] C. R. Everhart and J. B. MacChesney. Anisotropy in the electrical resistivity of vanadium dioxide single crystals. *Journal of Applied Physics*, 39(6):2872–2874, 1968.

[137] P.F. Bongers. Anisotropy of the electrical conductivity of vo2 single crystals. *Solid State Communications*, 3(9):275 – 277, 1965.

[138] Wei-Tao Liu, J. Cao, W. Fan, Zhao Hao, Michael C. Martin, Y. R. Shen, J. Wu, and F. Wang. Intrinsic optical properties of vanadium dioxide near the insulator - metal transition. *Nano Letters*, 11(2):466–470, 2011. PMID: 21166443.

[139] J. D. Budai, J. Hong, M. E. Manley, E. D. Specht, C. W. Li, J. Z. Tischler, D. L. Abernathy, A. H. Said, B. M. Leu, L. A. Boatner, R. J. McQueeney, and O. Delaire. Metallization of vanadium dioxide driven by large phonon entropy. *Nature*, 515:535, Nov 2014.

[140] Y. Zhou and S. Ramanathan. Mott memory and neuromorphic devices. *Proceedings of the IEEE*, 103(8):1289–1310, Aug 2015.

[141] Daniel Wegkamp, Marc Herzog, Lede Xian, Matteo Gatti, Pierluigi Cudazzo, Christina L. McGahan, Robert E. Marvel, Richard F. Haglund, Angel Rubio, Martin Wolf, and Julia Stähler. Instantaneous band gap collapse in photoexcited monoclinic vo_2 due to photocarrier doping. *Phys. Rev. Lett.*, 113:216401, Nov 2014.

[142] A. Cavalleri, Th. Dekorsy, H. H. W. Chong, J. C. Kieffer, and R. W. Schoenlein. Evidence for a structurally-driven insulator-to-metal transition in vo_2: A view from the ultrafast timescale. *Phys. Rev. B*, 70:161102, Oct 2004.

[143] Bong-Jun Kim, Yong Wook Lee, Sungyeoul Choi, Jung-Wook Lim, Sun Jin Yun, Hyun-Tak Kim, Tae-Ju Shin, and Hwa-Sick Yun. Micrometer x-ray diffraction study of vo_2 films: Separation between metal-insulator transition and structural phase transition. *Phys. Rev. B*, 77:235401, Jun 2008.

[144] Joyeeta Nag, Richard F. Haglund, E. Andrew Payzant, and Karren L. More. Non-congruence of thermally driven structural and electronic transitions in vo2. *Journal of Applied Physics*, 112(10):103532, 2012.

[145] Tao Yao, Xiaodong Zhang, Zhihu Sun, Shoujie Liu, Yuanyuan Huang, Yi Xie, Changzheng Wu, Xun Yuan, Wenqing Zhang, Ziyu Wu, Guoqiang Pan, Fengchun Hu, Lihui Wu, Qinghua Liu, and Shiqiang Wei. Understanding the nature of the kinetic process in a vo_2 metal-insulator transition. *Phys. Rev. Lett.*, 105:226405, Nov 2010.

[146] J. Laverock, S. Kittiwatanakul, A. A. Zakharov, Y. R. Niu, B. Chen, S. A. Wolf, J. W. Lu, and K. E. Smith. Direct observation of decoupled structural and electronic transitions and an ambient pressure monocliniclike metallic phase of vo_2. *Phys. Rev. Lett.*, 113:216402, Nov 2014.

[147] A P Levanyuk and Daniil G Sannikov. Improper ferroelectrics. *Soviet Physics Uspekhi*, 17(2):199, 1974.

[148] Nardeep Kumar, Armando Rúa, Félix E. Fernández, and Sergiy Lysenko. Ultrafast diffraction conoscopy of the structural phase transition in vo_2: Evidence of two lattice distortions. *Phys. Rev. B*, 95:235157, Jun 2017.

[149] T. M. Rice, H. Launois, and J. P. Pouget. Comment on "vo_2: Peierls or mott-hubbard? a view from band theory". *Phys. Rev. Lett.*, 73:3042–3042, Nov 1994.

[150] Michèle Gupta, A. J. Freeman, and D. E. Ellis. Electronic structure and lattice instability of metallic vo_2. *Phys. Rev. B*, 16:3338–3351, Oct 1977.

[151] D. Paquet and P. Leroux-Hugon. Electron correlations and electron-lattice interactions in the metal-insulator, ferroelastic transition in vo_2: A thermodynamical study. *Phys. Rev. B*, 22:5284–5301, Dec 1980.

[152] M. A. Korotin, N. A. Skorikov, and V. I. Anisimov. Variation of orbital symmetry of the localized $3d^1$ electron of the v^{4+} ion upon the metal-insulator transition in vo_2. *The Physics of Metals and Metallography*, 94(17):17–23, 2002.

[153] A. V. Kozhevnikov, V. I. Anisimov, and M. A. Korotin. Calculation of the electronic structure of the vanadium dioxide vo2 in the monoclinic low-temperature phase m1 using the generalized transition state method. *The Physics of Metals and Metallography*, 104(3):215–220, Sep 2007.

[154] Cédric Weber, David D. O'Regan, Nicholas D. M. Hine, Mike C. Payne, Gabriel Kotliar, and Peter B. Littlewood. Vanadium dioxide: A peierls-mott insulator stable against disorder. *Phys. Rev. Lett.*, 108:256402, Jun 2012.

[155] A. S. Belozerov, A. I. Poteryaev, and V. I. Anisimov. Evidence for strong coulomb correlations in the metallic phase of vanadium dioxide. *JETP Letters*, 93(2):70–74, Mar 2011.

[156] Jan M. Tomczak, Ferdi Aryasetiawan, and Silke Biermann. Effective bandstructure in the insulating phase versus strong dynamical correlations in metallic vo_2. *Phys. Rev. B*, 78:115103, Sep 2008.

[157] D. C. Mattis and W. D. Langer. Role of phonons and band structure in metal-insulator phase transition. *Phys. Rev. Lett.*, 25:376–380, Aug 1970.

[158] C J Hearn. Phonon softening and the metal-insulator transition in vo 2. *Journal of Physics C: Solid State Physics*, 5(12):1317, 1972.

[159] G. J. Hyland. Lattice polarization and coulomb energies in vo_2. *The Philosophical Magazine: A Journal of Theoretical Experimental and Applied Physics*, 20(166):837–841, 1969.

[160] Bence Lazarovits, Kyoo Kim, Kristjan Haule, and Gabriel Kotliar. Effects of strain on the electronic structure of vo_2. *Phys. Rev. B*, 81:115117, Mar 2010.

[161] K. Okazaki, H. Wadati, A. Fujimori, M. Onoda, Y. Muraoka, and Z. Hiroi. Photoemission study of the metal-insulator transition in $\mathrm{vo}_2/\mathrm{tio}_2(001)$: evidence for strong electron-electron and electron-phonon interaction. *Phys. Rev. B*, 69:165104, Apr 2004.

[162] Michel van Veenendaal. Ultrafast photoinduced insulator-to-metal transitions in vanadium dioxide. *Phys. Rev. B*, 87:235118, Jun 2013.

[163] Zhensheng Tao, Tzong-Ru T. Han, Subhendra D. Mahanti, Phillip M. Duxbury, Fei Yuan, Chong-Yu Ruan, Kevin Wang, and Junqiao Wu. Decoupling of structural and electronic phase transitions in vo_2. *Phys. Rev. Lett.*, 109:166406, Oct 2012.

[164] Hyun-Tak Kim, Yong Wook Lee, Bong-Jun Kim, Byung-Gyu Chae, Sun Jin Yun, Kwang-Yong Kang, Kang-Jeon Han, Ki-Ju Yee, and Yong-Sik Lim. Monoclinic and correlated metal phase in vo_2 as evidence of the mott transition: Coherent phonon analysis. *Phys. Rev. Lett.*, 97:266401, Dec 2006.

[165] M.. Mitrano, A. Cantaluppi, D. Nicoletti, S. Kaiser, A. Perucchi, S. Lupi, P. Di Pietro, D. Pontiroli, M. Riccó, S. R. Clark, D. Jaksch, and A. Cavalleri. Possible light-induced superconductivity in $\mathrm{k}_3\mathrm{c}_6 0$ at high temperature. *Nature*, 530:461, Feb 2016.

[166] Minjae Kim, Yusuke Nomura, Michel Ferrero, Priyanka Seth, Olivier Parcollet, and Antoine Georges. Enhancing superconductivity in $A_3\mathrm{c}_{60}$ fullerides. *Phys. Rev. B*, 94:155152, Oct 2016.

[167] Giacomo Mazza and Antoine Georges. Nonequilibrium superconductivity in driven alkali-doped fullerides. *Phys. Rev. B*, 96:064515, Aug 2017.

[168] A. Nava, C. Giannetti, A. Georges, E. Tosatti, and M. Fabrizio. Cooling quasiparticles in $\mathrm{a}_3\mathrm{c}_6 0$ fullerides by excitonic mid-infrared absorption. *Nature Physics*, 14:154, Oct 2017.

[169] Hideo Aoki, Naoto Tsuji, Martin Eckstein, Marcus Kollar, Takashi Oka, and Philipp Werner. Nonequilibrium dynamical mean-field theory and its applications. *Rev. Mod. Phys.*, 86:779–837, Jun 2014.

[170] H. Keiter and J. C. Kimball. Perturbation technique for the anderson hamiltonian. *Phys. Rev. Lett.*, 25:672–675, Sep 1970.

[171] N. Grewe. Spectral properties of the anderson model. *Zeitschrift für Physik B Condensed Matter*, 53(4):271–282, Dec 1983.

[172] N. E. Bickers. Review of techniques in the large-n expansion for dilute magnetic alloys. *Rev. Mod. Phys.*, 59:845–939, Oct 1987.

[173] D. J. Scalapino. Curie law for anderson's model of a dilute alloy. *Phys. Rev. Lett.*, 16:937–939, May 1966.

[174] Th. Pruschke and N. Grewe. The anderson model with finite coulomb repulsion. *Zeitschrift für Physik B Condensed Matter*, 74(4):439–449, Dec 1989.

[175] M. Keller, W. Metzner, and U. Schollwöck. Dynamical Mean-Field Theory for Pairing and Spin Gap in the Attractive Hubbard Model. *Physical Review Letters*, 86(20):4612–4615, 2001.

[176] Chuya Inoue and Fumihiko Takano. Effect of impurities on superconductivity in anderson model. *Progress of Theoretical Physics*, 48(4):1080–1089, 1972.

[177] G. C. Wick. The evaluation of the collision matrix. *Phys. Rev.*, 80:268–272, Oct 1950.

[178] Andreas Rüegg, Emanuel Gull, Gregory A. Fiete, and Andrew J. Millis. Sum rule violation in self-consistent hybridization expansions. *Phys. Rev. B*, 87:075124, Feb 2013.

[179] Martin Eckstein and Philipp Werner. Nonequilibrium dynamical mean-field calculations based on the noncrossing approximation and its generalizations. *Phys. Rev. B*, 82:115115, Sep 2010.

[180] Philipp Werner, Hugo U. R. Strand, Shintaro Hoshino, Yuta Murakami, and Martin Eckstein. Enhanced pairing susceptibility in a photodoped two-orbital hubbard model. *Phys. Rev. B*, 97:165119, Apr 2018.

[181] Francesco Peronaci, Marco Schiró, and Olivier Parcollet. Resonant thermalization of periodically driven strongly correlated electrons. *Phys. Rev. Lett.*, 120:197601, May 2018.

[182] A. Amaricci, A. Valli, G. Sangiovanni, B. Trauzettel, and M. Capone. Coexistence of metallic edge states and antiferromagnetic ordering in correlated topological insulators. *Phys. Rev. B*, 98:045133, Jul 2018.

[183] Frédéric Mila and Kai Phillip Schmidt. *Strong-Coupling Expansion and Effective Hamiltonians*, pages 537–559. Springer Berlin Heidelberg, Berlin, Heidelberg, 2011.

[184] J. Schwinger. On angular momentum. 1 1952.

[185] D. Ruan and W. Ruan. Boson realization of nonlinear so(3) algebra. *Physics Letters A*, 263(1):78 – 82, 1999.

[186] Q. H. Liu, D. M. Xun, and L. Shan. Raising and lowering operators for orbital angular momentum quantum numbers. *International Journal of Theoretical Physics*, 49(9):2164–2171, Sep 2010.